

UNIVERSITÄT
BAYREUTH

ULTRAFAST COHERENT DYNAMICS OF ELECTRONIC
EXCITATIONS IN SINGLE CONJUGATED POLYMERS AND
SUPRAMOLECULAR AGGREGATES

Von der Universität Bayreuth
zur Erlangung des Grades eines
Doktors der Naturwissenschaften (Dr. rer. nat.)
genehmigte Abhandlung

von
Kevin Wilma

aus Hof/Saale

1. Gutachter: Prof. Dr. Richard Hildner
2. Gutachter: Prof. Dr. Markus Lippitz

Tag der Einreichung: 09.04.2019

Tag des Kolloquiums: 19.06.2019

Summary

The spectroscopic characterisation of fundamental photophysical processes is highly important for the final physical picture of organic nanostructures and the further transfer of this knowledge to technical-relevant applications. The first few femtoseconds after a photo-excitation has taken place, determine the complete evolution to a large extend of the generated quantum mechanical properties and therefore the microscopic characteristics. This work provides a joint experimentally and theoretically approach, which is capable of extracting the ultrafast dynamics and quantum mechanical properties of single and supramolecular nano structures. By using an ultrafast spectroscopy setup and quantum dynamics identification (QDI) procedure the samples were measured and the important parameters identified.

The first chapter of this work was about the photoluminescence (PL) detected measurement of ultrafast dynamics of single methyl-substituted ladder type poly(*para*-phenylenes) (MeLPPP). MeLPPP is a suitable system for the analysis of two-photon (2P) processes, as the very rigid backbone is responsible for the strict quantum mechanical symmetry selection rules and its extraordinary 2P cross section. By using amplitude-shaping techniques, the ultrafast decay of the generated coherence between the electronic ground singlet state S_0 and the second excited singlet state S_2 was measured. The obtained data was subsequently analysed with the QDI-procedure and the underlying processes identified. All data was reliably reproduced by introducing a 3-level model, where a pure 2P transition takes place between S_0 and S_2 and the emission originates from the first excited singlet state S_1 . The obtained histograms of the optimised dephasing and relaxation rates as well as E_2 , the energy of S_2 reflect the inhomogeneity of the complex environments of each molecule. However, simply measuring the coherence decay is not enough to fully characterise MeLPPP with respect to the S_0 - S_2 2P Rabi-coupling, and hence more complex experiments need to be carried out.

These additional measurements were done by phase-only shaping techniques, where the PL intensity of single MeLPPP molecules was detected in dependency of the variation of the linear chirp. Most of the traces analysed, exhibit a symmetric PL intensity under variation of the linear chirp. This symmetric response was nicely reproduced by the QDI-procedure with the previous 3-level model. Surprisingly a considerable fraction of the data exhibits asymmetric PL dependencies on the linear

chirp. The QDI procedure was not able to find a minimum model which reproduces the asymmetric data within the 3-level model with physically reasonable parameters. Therefore the model was extended to a 4-level model, including a highly excited state (with a PL quantum yield nearly 0), denoted with S_3 . S_3 exhibits an energy mismatch of around one one-photon energy of the laser spectrum with respect to S_2 . Hence, for resonant conditions this level opens up the path for an additional 1P transition $S_2 \rightarrow S_3$, after excitation was generated in S_2 by a 2P absorption. Including this additional transition into as loss-channel for the generated population, the QDI-procedure found a minimum model reproducing the asymmetric data with high quality. The model describes a 4-level system with a (2+1)-photon transition, which is highly sensitive to the interplay between the electronic parameters of S_2 and S_3 and the instantaneous excitation energy. Both of these chapters proof that the described joint approach is capable of a reliable and fast extraction and characterisation of quantum mechanical and ultrafast parameters for single quantum systems. Furthermore this represents the first time proof of genuinely active coherent control of multi-photon processes via phase-shaping of single organic molecules in complex environment.

The second chapter is about similar ultrafast measurements on an ensemble of carbonyl-bridged triarylamine derivative with s-chiral side chains (S-CBT). S-CBT exhibits different aggregation behaviours, dependent on the used solvent. While S-CBT emerges fully dissolved in tetrahydrofuran (THF), n-dodecane (DOD) induces H-type like aggregation of the single building blocks to supra molecular nanofibres. The measurement of the coherence decay S-CBT in THF revealed a exclusively 2P allowed electronic state S_2 , which was not known before. Hence, the induced transition in these experiments does not take place between the electronic ground state S_0 and the first excited state S_1 , but between S_0 and S_2 . The results on the linear chirp variation and the two-color-pulse sequence both exhibited asymmetric PL intensities, as a function of the linear chirp parameter and the delay between the double pulse sequence, respectively, in analogy to MeLPPP. Two possible processes were considered, which could give rise to these asymmetric shapes: (i) the simultaneous stimulated emission (SE) of two-photons and (ii) the intersystem crossing (ISC) rate between the accessed state S_2 and an iso-energetic excited triplet state T_2 , which is dependent on the spectral phase of the laser pulse. Although the first option can not be excluded, further measurements on the existence of the triplet manifold, its energetic landscape and calculations of the shape of the generated wave packet in S_2 strongly corroborate the second option.

Changing the solvent from THF to DOD opens up the path for supramolecular nanofibres with clear H-type interaction characteristics between the S-CBT building blocks. In analogy to S-CBT in THF similar experiment for DOD were carried out. In

contrast to the H-type characteristic decrease of the PL quantum yields of S-CBT in DOD and the suppression of the 0-0 transition from the lowest excited singlet exciton band, the results of the ultrafast measurements for S-CBT in DOD resemble the data obtained for S-CBT in THF. In other words, the aggregation only seems to have minor influence on the accessed second excited singlet state S_2 , if at all. This agrees with theoretical predictions, which state that in case of a non-resonant two-photon transition, the limiting lifetime of the virtual state impedes efficient interaction of the dipole moments. Also for S-CBT in DOD the asymmetric linear chirp and two-color pulse sequence measurements could be explained by either stimulated emission of two photons or the wave packet shape dependent intersystem crossing rate between the excited singlet and triplet states. Latter option is further corroborated by the results on S-CBT in THF, but also by the fact that the electronic structure of the triplet manifold does not change considerably for the structural change from the isolated to the single nanofibre.

In conclusion, it has been shown, that an experimentally and theoretically joint approach is capable of measuring the ultrafast dynamics and energetic landscape of single organic molecules in a complex environment at room temperature. In doing so non-resonant 2P absorption processes were exploited to measure the ultrafast coherence decay envelope and achieve quantum mechanical coherent control over a (2+1)-photon transition. In the second part ultrafast measurement on a compound were presented, which exhibits an aggregation behaviour, strongly dependent on the used solvent. For the isolated monomer and its H-aggregated form it was shown, that next to the electronic states found in the linear absorption, this system exhibits an exclusively 2P allowed singlet state, which does not change its electronic structure upon aggregation. Furthermore, it is highly likely that phase-only modulation approaches are capable of coherently controlling this singlet-triplet transition by the generation of different shapes of wave packets in the excited state.

Deutsche Zusammenfassung

Die spektroskopische Charakterisierung fundamentaler photophysikalischer Prozesse prägt maßgeblich das finale Verständnis organischer Nanostrukturen und erleichtert den Transfer dieser Grundlagen auf technische Anwendungen. Die Entwicklung der Photophysik in den ersten Femtosekunden nachdem eine Photoanregung stattgefunden hat bestimmen meist den weiteren Verlauf der quantenmechanischen Eigenschaften des Systems und damit auch die mikroskopischen Eigenschaften. Diese Arbeit befasst sich mit der Messung solcher Ultrakurzzeitprozesse auf Zeitskalen mehrerer 10 bis hin zu Hunderten Femtosekunden. In Kombination mit einer Quantendynamik-Identifikations-Prozedur (QDI) können die erhaltenen Daten schnell und zuverlässig reproduziert und die zu Grunde liegenden Prozesse charakterisiert werden.

Der erste Teil dieser Arbeit befasst sich mit der Photolumineszenz (PL) detektierten Messung von Ultrakurzzeitdynamiken einzelner konjugierter Polymere in einer ungeordneten komplexen Umgebung bei Raumtemperatur. Die untersuchte Probe war Methylsubstituiertes Leiter Poly(*para*-Phenylen), kurz MeLPPP, und weist aufgrund seines sehr starren Polymer-Rückgrats strikte quantenmechanische Symmetrieauswahlregeln auf. Mittels Amplitudenmodulationsmessungen wurden zuerst die Kohärenzzerfälle vom ausschließlich Zwei-Photonen (2P) erlaubten zweiten angeregten Singulett S_2 gemessen. Die Ergebnisse wurden anschließend mit der QDI-Prozedur erfasst und die zu Grunde liegenden Prozesse identifiziert. Alle Kohärenzzerfälle konnten mit einem 3-Niveau Modell und dem 2P-Übergang vom elektronischen Grundzustand S_0 in den S_2 verlässlich und mit hoher Qualität reproduziert werden. Die Verteilungen der optimierten Dephasierungs- und Relaxationsraten als auch der Energie E_2 von S_2 spiegeln die Inhomogenität der komplexen Umgebungen wider. Nichtsdestotrotz fehlte für die komplette Charakterisierung von MeLPPP die 2P Rabi-Kopplung zwischen S_0 und S_2 , die, speziell für MeLPPP, nur mittels komplexerer Experimente analysiert werden kann.

Diese Messungen befassen sich mit reinen Phasenmodulationstechniken und die Detektion der PL Intensitäten einzelner MeLPPP in Abhängigkeit des linearen Chirps. Die Ergebnisse zeigen, dass für den Großteil der analysierten Moleküle eine symmetrische Abhängigkeit der PL Zählraten vom Chirpparameter β besteht. Diese Symmetrie konnte mit dem vorhergehenden 3-Niveau Modell sehr gut reproduziert werden. Überraschen-

derweise zeigt ein signifikanter Teil des Datensatzes asymmetrische PL-Abhängigkeiten bezüglich des linearen Chirps. Versuche, diese Asymmetrie mit dem vorhergehenden 3-Niveau System zu reproduzieren waren erfolglos. Das Modell wurde anschließend um ein zusätzliches energetisches Niveau, gekennzeichnet mit S_3 , erweitert, welches zugleich eine Energiedifferenz von 13000 cm^{-1} zu S_2 aufweist und eine verschwindend geringe PL Quantenausbeute besitzt. Die Energiedifferenz entspricht dabei genau der Energie eines Photons des Laserspektrums, weshalb die Möglichkeit eröffnet wird, nach einer 2P-Absorption in den S_2 eine zusätzliche Ein-Photonen (1P) Absorption von S_2 nach S_3 zu induzieren. Mit diesem zusätzlichen Übergang und dem Wissen, dass die PL-Quantenausbeute von S_3 gleich 0 ist, konnte die Asymmetrie reproduziert und der ablaufende Prozess als ein (2+1)-Photonenübergang identifiziert werden. Die optimierten Modellparameter stimmen mit denen überein, die aus den Kohärenzzerfällen erhalten wurden, wobei nun die energetische Landschaft und die Dephasierungsraten um die jeweiligen Parameter von S_3 erweitert wurden. Der komplette (2+1)-Photonen Übergang hängt stark vom Zusammenspiel der energetischen und dynamischen Parameter von S_2 und S_3 mit der instantanen Laserfrequenz ab und kann deshalb über die lineare Phase kontrolliert werden. Durch beide Abschnitte in diesem Kapitel wurde schlussendlich gezeigt, dass die hier vorgestellte Kombination aus Experiment und Theorie ein leistungsfähiges Werkzeug ist, um schnell und verlässlich quantenmechanische Parameter zu extrahieren und charakterisieren. Des Weiteren stellt der zweite Teil den ersten erfolgreichen Versuch dar, einen (2+1)-Photonen Prozess in organischen Molekülen in komplexer Umgebung kohärent zu kontrollieren.

Der zweite große Teil dieser Arbeit befasste sich mit Ensemble-Messungen an Carbonyl-verbrückten Triarylamine (CBT) mit S-chiralen Seitenketten (S-CBT), ein molekulares System, das durch die Wahl des Lösungsmittels zu supramolekularen Strukturen heranwachsen kann. In Analogie zu MeLPPP wurden sowohl der Kohärenzzerfall und die lineare Chirp abhängige PL-Zählrate als auch das Verhalten unter einer Zwei-Farben-Puls Sequenz Anregung gemessen. Als Lösungsmittel wurden Tetrahydrofuran (THF) und n-Dodekan (DOD) verwendet, wobei S-CBT in THF komplett gelöst ist und in DOD zu Nanofasern aggregiert. Die ersten Messungen an S-CBT in THF ergaben, dass der induzierte Übergang nicht etwa zwischen dem elektronischen Grundzustand S_0 und dem ersten angeregten Singulett S_1 stattfindet, sondern vielmehr zwischen S_0 und einem ausschließlich 2P-erlaubten Zustand S_2 (zweiter angeregter Singulett). Des Weiteren wurden Prozesse identifiziert, die eine Asymmetrie sowohl der linearen Chirp als auch der Zwei-Farben-Puls Messungen verursachen. Dabei kommen zwei Prozesse in Frage, welche eine Abhängigkeit von der spektralen Phase des Laser aufweisen können: (i) die simultane stimulierte Emission (SE) zweier Photonen und (ii) das

Intersystem-Crossing zwischen S_2 und iso-energetischen Triplet T_2 . Wobei die erste Variante nicht per se ausgeschlossen wurde, bestärken weitere Messungen über die Existenz der Triplet-Zustände, deren spektralen Positionen und Rechnungen zu den quantenmechanischen Wellenfunktionen die letztere Variante sehr.

Ändert man nun das Lösungsmittel von THF zu DOD, entstehen innerhalb der Lösung supramolekulare Strukturen, die einen klaren H-Typ ihrer Wechselwirkung zwischen den einzelnen S-CBT Molekülen aufzeigen. In Analogie zu THF wurden die gleichen Messungen angefertigt und die erhaltenen Daten ausgewertet. Obwohl aufgrund der Aggregation die strahlende Rate deutlich sinkt, weisen sowohl die Kohärenzzerfälle als auch die Resultate der linearen Chirp und Zwei-Farben-Puls Messungen die gleichen Charakteristika auf wie die Ergebnisse für S-CBT in THF. Dies weist wiederum darauf hin, dass auch hier der induzierte Vorgang zwischen dem S_0 und dem S_2 stattfindet, und darüber hinaus S_2 keinerlei elektronische Veränderung hinsichtlich der Aggregation zeigt. Dies stimmt der Theorie überein, die beschreibt, dass sich für nicht-resonante 2P-Übergänge keine ausreichende Wechselwirkung ergibt, die wiederum die elektronischen Eigenschaften dieser Zustände beeinflusst. Ferner zeigen die Phasenmodulationsmessungen die gleichen Asymmetrien, die auch hier mit den oben genannten Prozessen erklärt werden können, da auch die Triplet-Struktur sich nicht signifikant zu ändern scheint, nachdem die supramolekularen Strukturen gebildet wurden. Schließlich wurden für dieses sehr komplexe molekulare System Messungen angefertigt, die großen Aufschluss über die Kurzzeitdynamiken als auch dessen Energielandschaft geben.

Zusammenfassend konnte in dieser Arbeit eine Kombination aus experimenteller Ultrakurzzeitspektroskopie und theoretischer Quantendynamik-Identifikations Prozedur entwickelt werden. Dieser Ansatz erlaubt es schnell und zuverlässig quantenmechanische Parameter aus komplexen System zu extrahieren und verlässlich zu beschreiben. Durch die Einzelmolekülmessungen an MeLPPP wurde erstmalig der ultraschnelle Kohärenzzerfall in einem ausschließlich Zwei-Photon erlaubten Zustand vermessen und die kohärente Kontrolle einzelner organischer Nanoobjekte via eines (2+1)-Photonen-Prozesses gezeigt. Im zweiten Teil wurde ein komplexes System analysiert, was ein Lösungsmittel-abhängiges Aggregationsverhalten aufweist. Sowohl für das isolierte Monomer, als auch für die aggregierten Nanofasern wurde ein strikt Ein-Photon verbotener, jedoch Zwei-Photonen erlaubter elektronischer Singulett Zustand gefunden, dessen elektronische Struktur durch die Aggregation nicht beeinflusst wird. Des Weiteren scheint die kohärente Kontrolle der *Intersystem-Crossing* Rate möglich, die den Übergang zwischen dem Zwei-Photonen erlaubten Zustand und einem höher energetischem Triplet-Niveaus beschreibt.

The shepherd's boy says, "There's this mountain of pure diamond. It takes an hour to climb it, and an hour to go around it. Every hundred years, a little bird comes. It sharpens its beak on the diamond mountain. And when the entire mountain is chiseled away, the first second of eternity will have passed."

You must think that's a hell of a long time. Personally, I think that's a hell of a bird.

- The Doctor

Contents

Summary	i
Deutsche Zusammenfassung	v
1 Motivation	1
2 Introduction	5
2.1 Photophysics of Organic Molecules and Conjugated Polymers	5
2.2 Quantum Mechanical Description of the Linear and Non-Linear Susceptibility	13
2.3 Group Theory of Organic Molecules	18
2.4 Aggregation and Two-Photon Accessible States	25
2.5 Optical Bloch Equations	28
2.6 Quantum Dynamics Identification	32
3 Experimental	37
3.1 Sample	37
3.2 Sample Preparation	42
3.3 Technical Informations	42
3.4 Modulation Patterns	48
4 Ultrafast Measurements and Coherent Control of Single Molecules	51
4.1 Introduction	52
4.2 Two-Photon Induced Coherence Decays	53
4.3 Visualising “Hidden” States by Single Pulse Coherent Control	63
4.4 Conclusion on Coherence Decays and β -dependent Measurements	74
5 Ultrafast Processes upon Aggregation in Supramolecular Structures	77
5.1 Introduction	77
5.2 Experimental	78
5.3 Ultrafast Measurements on the Isolated Molecule in Solution	80

5.4	Ultrafast Measurements on Single Nanofibres in Solution	93
5.5	Conclusions on the Isolated Molecule and Nanofibres	101
Appendix		105
A.1	Group Theory Calculations on the S-CBT Core	105
A.2	Technical Details	106
A.2.1	Spincoater Settings	106
A.2.2	Quantum Dynamics Identification	106
A.3	Coherence Decay of an Ensemble MeLPPP Sample in Toluene	107
A.4	Shape of the Linear Chirp Dependent Photoluminescence Traces	109
A.5	Symmetric Simulations to Asymmetric Data	111
A.6	Asymmetry of Linear Chirp Dependent S-CBT Measurements	113
A.7	Fluorescence Spectroscopy of Highly Excited States in S-CBT	114
A.8	Transient Absorption Spectroscopy	115
A.9	Wavefunctions upon Linearly Chirped Excitation	116
Bibliography		119
Publication List		129
Danksagung		131

List of Figures

2.1	Organic Molecules and Conjugated Polymers.	7
2.2	Optical Processes in Chromophores.	9
2.3	Homogeneous and Inhomogeneous Line Widths of Single Chromophores and Ensembles.	12
2.4	One- and Two-Photon Absorption.	16
2.5	Symmetry Operations on a Monomer Unit of Methyl Substituted Ladder-Type Poly(<i>para</i> -phenylene) (MeLPPP).	20
2.6	Symmetry Operations on an Individual Carbonyl-Bridged Triarylamine Derivative.	23
2.7	Allowed 1P and 2P Transitions.	24
2.8	Schematic Energy Diagram and Absorption for Ideal J- and H-Type Aggregates.	26
2.9	Bloch Sphere and Vector.	30
2.10	Schematic Coherence Decay Envelope.	31
2.11	Scheme for Identifying the Single Molecule Quantum Dynamics from a Phase Shaping Experiment.	34
3.1	Spectral Characteristics of MeLPPP.	38
3.2	Spectral Characteristics of S-CBT.	40
3.3	Experimental Setup.	43
3.4	Pulse Characterisation.	46
3.5	Modified Excitation/Detection Unit.	46
3.6	Pulse Characterisation for the Modified Setup.	47
4.1	Time and Spectral Dependent Characteristics of the Excitation.	54
4.2	Intensity Trace of Two Single Molecules Under Constant Excitation.	55
4.3	Coherence Decays of Single Molecules.	57
4.4	Phase Scan of Double Pulse Sequence for an Ensemble Sample.	58
4.5	Statistics on Energetic Landscape and Ultrafast Dynamics of Single Molecules.	59

4.6	Bloch Vector Tip Dynamics of Two Individual MeLPPP Molecules.	62
4.7	Spectral and Time-Dependent Characteristics of the Excitation.	64
4.8	Coherent Control of Two-Photon Induced Absorption in an Ensemble and in Single Molecules.	66
4.9	3-Level Model Simulations of β-Dependent Populations of a Single Molecule.	68
4.10	4-Level Model Simulations on the Population of Three Single Molecules.	71
4.11	Time-Dependent Population Dynamics for Different Values of $\pm\beta$.	72
4.12	Amplitude and Phase-Shaping Experiments on One Individual Molecule.	75
5.1	Spectral Characteristics of S-CBT in THF and of the Excitation Source.	79
5.2	Ultrafast Measurements on S-CBT in THF.	81
5.3	Two Colour Double Pulse Sequence Measurements on S-CBT in THF.	83
5.4	Two-Photon Absorption of S-CBT in THF.	86
5.5	Nanosecond Transient Absorption Spectra of S-CBT in THF.	90
5.6	Processes Leading to an Asymmetric Behaviour.	92
5.7	Spectral Characteristics of S-CBT in DOD and Laser.	95
5.8	Ultrafast Measurements on S-CBT in DOD.	96
5.9	Two Color Double Pulse Excitation Measurements on S-CBT in DOD.	97
5.10	Energy Diagram and Sketch of Ultrafast Processes for the Isolated Molecule and Nanofibre.	102

List of Tables

4.1	Optimal Model Parameters for Three Individual Molecules. . .	56
4.2	Three- and Four-Level Simulation Parameters.	67
5.1	Franck-Condon Progression of S_1 and S_2	87

Chapter 1

Motivation

Processes taking place during the time directly after the event of a photoabsorption of a quantum system, such as atoms or molecules, mainly determine the further quantum mechanical dynamics and finally nano- and microscopic photoactive characteristics. Such processes include the excited states wave packet formation and evolution, and the resulting population and energy transfer processes, respectively. The sound understanding of the latter one is highly fundamental to analyse light harvesting mimicry systems and organic electronics. However, the first step is always the analysis of these processes on a truly molecular level, which, in the case of a single molecule sample, removes the ensemble averaging and allows for detection of the individual properties inherent to each nano-object.

The first evidence of single-molecule detection was demonstrated by a variety of research groups in the late 1980s. While Moerner and Kador detected the absorption of single dopant molecules of pentacene in a *p*-terphenyl host crystal at low temperatures [1], Orrit and Bernard took advantage of the Stokes-shift and detected the fluorescence of the same sample-host system [2]. Nowadays, single-molecule techniques are mainly based on the detection of the fluorescence/photoluminescence as it requires a much more complex setup and technique to detect the absorption spectrum of single nano objects. In the experiment itself, addressing single molecules can be done via spectral and spatial selectivity. While at low temperatures, the electronic transitions are extremely narrow and therefore also the linked spectral bandwidth, at room temperature these transitions are broadened. Hence, in the former case single molecules can be addressed by a spectral selectivity and resonant excitation. In contrast, at room temperatures this approach does not work out and measuring single molecules is only achieved by producing extremely low concentrations of molecules in the host system. This ends up in spatially well separated positions of the single molecules through the host and each emitter can be addressed by positioning it in the excitation volume. With single-molecule techniques, as stated above, ensemble averaging can be overcome. This refers to the spatial inhomogeneity of the host and therefore the variety of local surroundings and interactions of the sample

with its host. As a result, in single-molecule experiments, different sample-host systems but also time-dependent dynamics can be accessed (from ns to s). This time-dependent detection of the photoluminescence intensity of single emitters can exhibit sudden jumps to higher or lower signal levels as well as quasi-continuous variations of the intensity. Former one is classified as “blinking” and can yield a lot of information about the analysed system. While some groups found that the blinking statistics and dynamics can reveal the energy transfer rates between different electronic states of a multi-chromophoric system [3] or along a polymer chain to a single localised polymer defect [4], Schörner *et. al.* have shown, that single proteins can exhibit a conformational memory only by the investigation of the time-dependent intensity fluctuations [5]. Next to the solely detection of the intensity level, modern photo-detecting devices open the path for the time-dependent detection of the photoluminescence lifetime and spectrum. By polarisation resolved detection of the spectrum, Issac *et. al.* revealed the emitting species of a multi-chromophoric system and showed that emission occurs not only from the lowest energy site but more from all neutral subunits [6]. Another experiment was carried out by Wilma and Issac [7], where spectral shifts, immediately occurring before a blinking event, were identified with the approach of a single electron from the host and were finally able to track the electron dynamics by using the single molecule as a probe. The quasi-continuous variations of the time-dependent intensity on the other hand is commonly referred to spectral diffusion, which is a highly dynamical process at room temperatures and due to spatial rearrangements of the chromophore itself or its surrounding host material [8, 9]. Analysis of the spectral diffusion behaviour can yield information about the nature of excitation state [10, 11] or also the orientation of the transition dipole moment [12].

Although conventional single-molecule techniques have proven their power and versatility, they are limited to the photoluminescence lifetime of the molecule, which is typically around several ns to ps in extreme cases [13–17]. However fundamental processes, such as charge and energy transfer, electronic dephasing and intramolecular vibrational relaxation occur on times scales much faster than ns. As a result, the development of extended novel single-molecule techniques is a key prerequisite for improving and completing the understanding of dynamics in organic matter.

As a first step towards the time scales of fs to ps, pump-probe spectroscopy is capable of measuring intra- and intermolecular energy transfer rates, as well as system recovery times, which are not necessarily connected to radiative channels. By time and spectral dependent detection of the transmittance of the pumped and not pumped system, stimulated and spontaneous emission as well as excited state absorptions and ground state bleaches can be measured [17]. Although this method is usually limited to bulky

samples, a similar photoluminescence detected approach was successfully extended to the single-molecule level by van Dijk *et. al.* in the group of van Hulst [18, 19]. By measuring the photoluminescence signal in dependency of an ultrafast delay between two pulse replica they demonstrated the capability of their setup of investigating the ultrafast relaxation pathways by incoherent pump-dump processes on the fs time scale. Next to a control over the delay between the two pulses, the adjustable phase between the pulses opens up the path to probe phase memory of the single molecule. The finally detected photoluminescence is then a function of the delay and phase difference between both pulses. Hildner *et. al.* have demonstrated for the first time the measurement of the optical free induction decay of single molecules under ambient conditions with this phase-locked double pulse excitation scheme and furthermore analysed the electronic dephasing dynamics [20]. Phase-only approaches on the other hand can change the outcome of photoinduced processes, too, but genuine active coherent control was only proven for the strong interaction regime [21–24]. This lack of phase-sensitivity in the strict one-photon limit was already predicted by theoretical groups and accordingly, one-photon coherent control is only possible in open quantum systems if the environmentally induced dissipation is strong [25, 26]. This hypothesis was tested by the group of Kukura by applying phase-shaping approaches to the retinal photoisomerization, but did not show any proof of one-photon phase control [27]. In other words, up to date there is no evidence for active coherent control in the strict one-photon limit.

This work connects to these results by measuring the ultrafast dynamics and energetic landscape of single methyl-substituted ladder type poly(*para*-phenylenes) (MeLPPP) in complex environments. The experimental approach will be extended to aggregating carbonyl-bridged triarylamin derivatives with *s*-chiral side chains (S-CBT) [28] and their electronic energy pathways will be analysed. The key aspect, however, is that instead of a single-photon absorption, the optical transition is induced by two-photons. Subsequent analysis of these novel data with a theoretical identification procedure allows the extraction of parameters describing the ultrafast dephasing and relaxation times as well as the energetic landscape. New insights into coherently controlled multi-photon processes and an in-depth discussion of the excitation energy pathways will be provided.

This thesis is organised as follows: in Chapter 2 basic principles of photophysical properties of single molecules and aggregates, group theory aspects as well as ultrafast dynamics are discussed. Chapter 3 provides all helpful experimental information about the sample preparation, methods and pulse-shaping approaches. While the first part of Chapter 4 demonstrates the possibility to use the experimental setup and the theoretical identification procedure to measure and reliably describe ultrafast dynamics induced by two-photon absorptions in single MeLPPP molecules, the second part is about

the coherent control of (2+1)-photon processes in the same sample and the further identification of dark states. The second main measurements in Chapter 5 reveal a two-photon accessible state in the S-CBT system and provide two possible processes which are coherently controlled. Furthermore, this chapter demonstrates that the two-photon allowed state is unaffected by H-type aggregation of the S-CBT system. The summary can be found in the end of this thesis.

Chapter 2

Introduction

The core of this work is the measurements of ultrafast processes and coherent control of conjugated polymers (CP) and supramolecular aggregates. Within this, single methyl-substituted ladder type poly(*para*-phenylene) (MeLPPP) are embedded in a solid matrix and exposed to phase and amplitude shaped excitation pulse sequences. In analogy to the single CP measurements, ensemble solutions of a carbonyl-bridged triarylamine derivative with *s*-chiral side chains (S-CBT) are analysed, additionally in dependency of different aggregation states. In both cases the concept of chromophores, composed of multiple individual building blocks, will be used to describe the interaction between the photo active subunits and the excitation field for both cases, the MeLPPP and S-CBT.

2.1 Photophysics of Organic Molecules and Conjugated Polymers

The knowledge of basic photophysical properties of organic molecules builds the groundwork of a clear understanding of this work. In this section a brief introduction of organic molecules and conjugated polymers (CP) as well as their photophysics is presented. Transitions between pure electronic and additional vibronic states are discussed, followed by an overview of dynamic loss mechanisms (dephasing and relaxation), which are responsible for the line widths of these transitions. These dynamics will be discussed with regard to modern experimental ultrafast results on CP and low molecular weight molecules.

Electronic and spectral properties of organic molecules and polymers

The most fundamental functional building blocks of modern organic electronics are CP and dye molecules. Requirements on the material, such as charge transfer efficiency, absorption cross section and photostability just to mention a few, are

specific to their application. The functionality of organic solar cells, for example, requires a broad absorption in the spectral range and efficient energy and charge transfer mechanisms [16]. High tuneability of these spectral characteristics due to their molecular structure is a beneficial key feature. Assembling these building blocks to more complex structures, covalently or non-covalently bound, can create even more advantageous properties [29–36]. Supramolecular aggregates can exhibit a high tunable absorption in the visible range and additional efficient energy transfer mechanisms. More information on the photophysics of these architectures can be found in section 2.4.

Covalently bound structures like conjugated polymers, consisting of tens to hundreds bound building blocks, are of big interest in the field of organic electronics. Due to their alternating single and double bonds along the polymer backbone and their structural conformation, they exhibit features like energy transfer, non-linear optical behaviour and strong (tunable) absorption in the visible range [30, 33, 37]. These properties are a consequence of orbital hybridisation. The alternating σ -bonding carbon atoms form the plane of the backbone (σ -plane), in which the so called “conjugated path” can be found. The remaining hybridised, p_z -orbitals stick out of this plane and overlap with the neighbouring ones, which generates a π -bond. These bonds create a delocalised π -electron system, which finally is responsible for the electronic properties of the conjugated polymer [16, 33, 37]. In Figure 2.1 the chemical structures of a single organic molecule (Carbonyl-bridged triarylamine derivative [28], a) and a conjugated polymer (methyl-substituted ladder type poly(*para*-phenylene) [38], b) are shown. Next to their central building blocks (in this case: the triarylamine core (a) and the poly(*para*-phenylene) (b)) functional molecules and polymers have attached side groups (R_i) in order to, e.g., improve their solubility.

Photophysics of single molecules and conjugated polymers can be described with the many-body Hamiltonian [39, 40]. In doing it was shown, that the photophysics of polymers do not behave like perfectly aligned chains with a fully extended π -electron system [41, 42]. The electron-electron and electron-phonon coupling lead to a localisation of the electronic wave function on several repeating units on the backbone. Moreover, defects like kinks, torsions or chemical defects enhance this wave function localisation. These subdivided parts of the polymer can consist of several repeating units and are called *chromophores* [43–47]. The *conjugation length* is the size or the number of repeating units inside a chromophore. As defects randomly break the perfectly aligned structure of a polymer chain (depending on synthesis, host material, chemical composition) the conjugation lengths are statistically distributed for a sample of polymer and the π -electron system gets subdivided. For the rigid polymer MeLPPP shown in

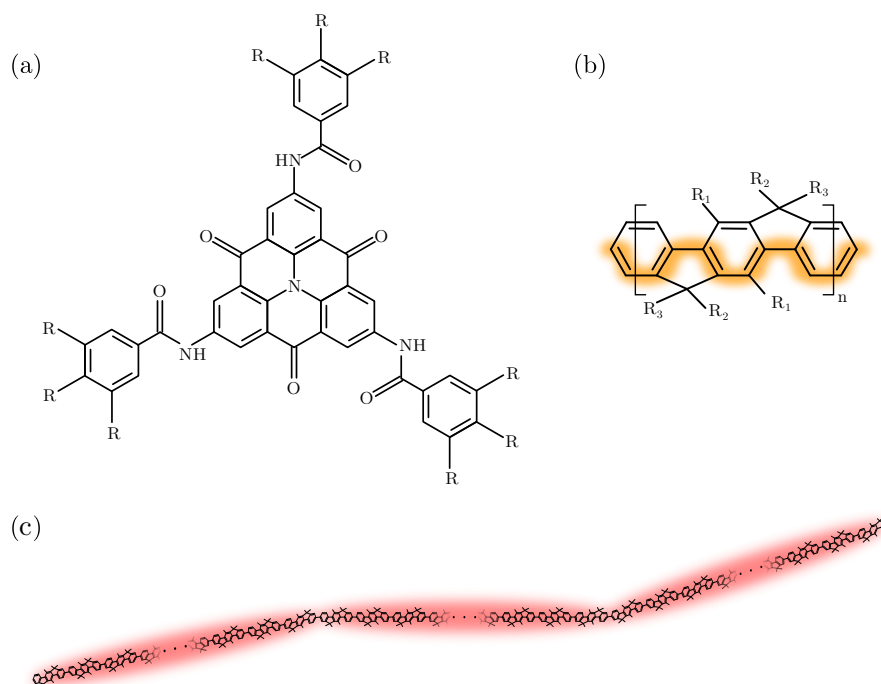


Fig. 2.1: Organic Molecules and Conjugated Polymers. (a) Carbonyl-bridged triarylamin derivative with *s*-chiral side chains (S-CBT)[28]. (b) Methyl-substituted ladder type poly(*para*-phenylene) with conjugated path along the polymer backbone (orange shaded). (c) Schematic structure of a MeLPPP polymer chain consisting of three chromophores (red shaded ellipse). (a, b) For clarity reasons the side groups are not shown.

Fig.2.1 (b) a typical polymer chain is separated into about 10 - 15 chromophores (2.1 (c)), with one chromophore consisting of 5 to 10 repetition units [46, 48–51]. From this point on, all considerations made, are based on the term chromophore, whether in a sense of a single molecule or a delocalisation on a CP chain or supramolecular aggregate, respectively.

$$H = H_{n,n}(\mathbf{R}_i) + H_{e,e}(\mathbf{r}_i) + H_{e,n}(\mathbf{r}_i, \mathbf{R}_i) \quad (2.1)$$

The many-body Hamiltonian consists mainly of three parts: (i) the kinetic and potential energy of the nuclei $H_{n,n}(\mathbf{R}_i)$, (ii) the kinetic and mutual potential energy of the electrons $H_{e,e}(\mathbf{r}_i)$ and (iii) the coulomb interaction between electrons and the nuclei of the molecule $H_{e,n}(\mathbf{r}_i, \mathbf{R}_i)$, with \mathbf{R}_i and \mathbf{r}_i representing a full set of nuclear and electronic coordinates. The Schrödinger equation can be solved for the very simple case of single hydrogen atom in vacuum. However, already the solution for the allegedly still simple H_2^+ molecule is not exact any more [39]. Therefore simplifications on the Hamiltonian have to be made.

The *Adiabatic-* and *Born-Oppenheimer-Approximation* (BO approximation) separate the dynamics of the nuclei from the electrons [39, 40]. This assumption is based on the fact, that the mass of the nuclei is much bigger than electron mass ($\frac{m_n}{m_e} \approx 10^4$) and therefore the nuclear dynamics are slow in comparison to the electrons. In the final analysis the result of the BO approximation is a total state wave function $|\psi(\mathbf{r}_i, \mathbf{R}_i)\rangle$ which consists of a direct product of an electronic ($|\psi_e\rangle$) and a nuclear (vibrational, $|\psi_\nu\rangle$) wave function. Notably the pure electronic part is only parametrically dependent on the positions of the nuclei

$$|\psi\rangle = |\psi_\nu(\mathbf{R}_i)\rangle |\psi_e(\mathbf{r}_i, \mathbf{R}_i)\rangle \quad . \quad (2.2)$$

The photophysical properties (e.g. the transition dipole matrix element, which is a measure for the probability of transitions) can be derived from this stage for simple chromophores by perturbation theory (see section 2.2). Upon interaction with an electro-magnetic (EM) field population is generated in an excited state. The electronic states are approximated with a harmonic potential, with the vibrational energies equally separated by an effective vibration of energy $\hbar\omega_{\text{eff}}$. The energy gap between the lowest excited state and the ground state is of optical frequencies (E_0), thus the transitions between those states are called *optical transitions*. In the following an overview is given to understand steady state spectral properties as well as dephasing and relaxation processes. Therefore an exact calculation of the quantum mechanical properties such as the transition dipole matrix element does not need to be calculated quantitatively at this stage. However, it should be noted, that the approximations made above are useful for simple structures, but the problem remains still too complicated for greater architectures. Further simplifications, especially for conjugated polymers have to be made. Hückel treated mathematically, as a starting point, the π -electron system along the backbone like a particle in the box, whereas the Pariser-Parr-Pople and Su-Schrieffer-Heeger model took the electron-electron and electron-phonon coupling into account, respectively [16].

(Non-)Radiative Transitions. The electronic and spectral properties of chromophores can be simplified and pictured with a *Jablonski* diagram (see Fig.2.2 (a)). This diagram reflects an energy level scheme for one single chromophore and the corresponding transitions. The energy levels consist of pure electronic (S_i, T_i) and associated vibrational states (ν_i). Transitions between those states are denoted with vertical arrows, with an upward arrow reflecting the absorption and pointing downwards displays an energy loss, whether by non-radiative or radiative processes. Quantum mechanical selection rules forbid (one photon) transitions between states with different spin multiplicity ($S = 0$ for a singlet state S_i and $S = 1$ for triplet T_i) and/or between

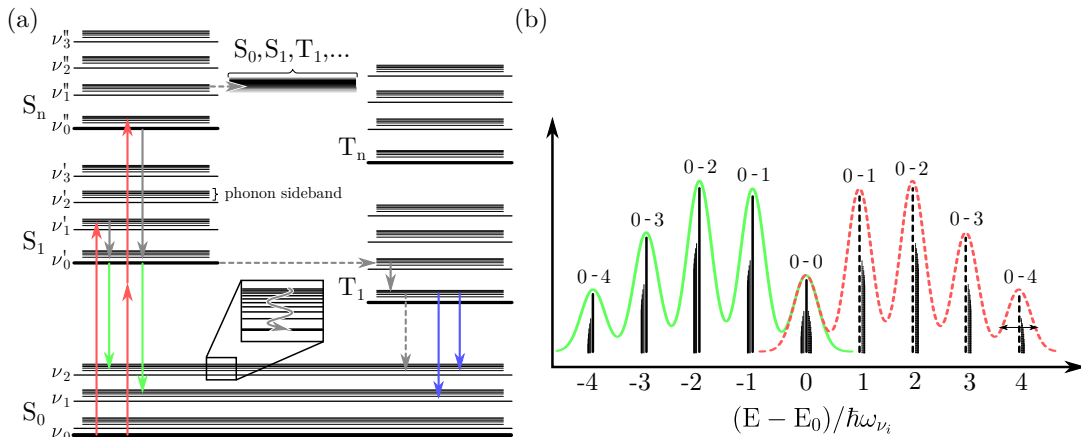


Fig. 2.2: Optical Processes in Chromophores. (a) Simplified Jablonski diagram with: absorption (red), emission (green) and non-radiative processes (grey arrows, solid and dashed). The non-radiative processes are subdivided into intersystem crossing (ISC, dashed lines) and internal conversions (IC, solid grey arrows). The inset shows enlarged the phonon side band with an IC process. Singlet states are denoted with S_i , Triplets with T_i and vibrational modes with ν_i . The vibrational modes are separated by an effective mode energy $\hbar\omega_{\text{vib}}$. (b) Schematic line (black) and related broadened spectrum (em. green, abs. red) of the vibronic transitions (ν_i , $i = 0, 1, 2, \dots$ between the electronic ground state S_0 and the first excited state S_1 of energy E_0 (with the energy of S_0 set to zero). Solid (dashed) vertical black lines present the sharp transitions between the particular energy levels for an emission (absorption) process. The peaks are denoted with the 0 ($i = 0, 1, 2, 3, 4$) for the vibrational mode of the initial (final) state of the specific transition

states of same parity (even “g” and uneven “u”) [39]. However, spin-orbit coupling breaks the former rule by generating small admixtures of triplet and singlet states, with singlet states exhibiting a small triplet character and vice-versa. Therefore transitions between those states become possible, if however with small probability (intersystem crossing, ISC). The second rule is also not ultimate, which will be discussed in more detail in section 2.3. Due to their weak spin-orbit coupling the ground state S_0 and lowest excited state S_1 are singlet states. Next to S_0 and S_1 multiple additional states can exist. Triplet states are denoted with $T_{1,2,\dots}$ and higher excited electronic singlet states with S_n ($n \geq 2$), which are often unclear to assign. Next to electronic and vibronic levels, small densely packed energy levels are evident in the emission (absorption) at the low-energy (high-energy) wing, which correspond to the phonon-side band (PSB, see also Fig.2.3)[52]. These energy levels are due to the electronic coupling to phonons of the surrounding matrix in which the chromophore is embedded. The PSB will be evident in single molecule experiments at cryogenic temperatures and typically has a width of about tens of wavenumbers [48, 51, 53, 54]. Electronic transitions between singlet states can be accessed by absorption or fluorescence spectroscopy, in which, depending on the symmetry of the electronic wave functions, one-photon [39, 40, 55]

or two-photon absorption processes [56, 57] have to be induced. Typical energies for one-photon transitions between S_0 and S_1 are between 12500 cm^{-1} to 25000 cm^{-1} for low molecular weight organic molecules and CPs [16, 29, 40, 51, 58, 59]. Two-photon induced transitions are usually located at the high energy site of this scale and are typically 1000 cm^{-1} to 5000 cm^{-1} above the first excited singlet state [38, 51, 56] due to alternating symmetries of the wave functions. States with a strong triplet character can be identified via pump-probe spectroscopy or nano second lifetime measurements [17].

Upon absorption, population is usually generated in a vibrational level in the first excited singlet state S_1 . Within the first 200 fs after excitation [38, 60, 61] the vibrational energy is rapidly dissipated (non-radiatively) into the surrounding host (solvent or matrix molecules) and the generated population can decay back to S_0 under emission of radiation (fluorescence, ps to ns [29, 38, 62, 63]). If population is generated in a high lying electronic state S_n via one- or multi-photon absorption the first step is highly likely a fast internal conversion (IC, non-radiative, sub 50 fs) into S_1 [64] followed by radiative processes into the ground state. Iso-energetic transitions are presented in Fig. 2.2 with horizontal gray arrow from S_n ($n \geq 2$) to the manifold of high energetic states of the singlets S_{n-1} and triplets T_{n-1} from where further internal conversion takes place. Other non-radiative processes are ISC, from singlet states to triplets and vice-versa. Due to the low transition probability between singlets and triplets, generated triplet population stays significantly longer in the excited state T_1 than e.g. in S_1 , which is reflected by a longer lifetime of triplet states (μs to ms for phosphorescence [17, 63] compared to fluorescence ps to ns).

Dephasing, Relaxations and Line shapes. The superimposed curves (green solid, red dashed) in Fig. 2.2 (b) reflect real absorption and emission spectra. The evident vibronic progression is due to the vibronic level manifold in each electronic state, and is quantum mechanically described by electron-phonon coupling. A measure for this coupling is the *Huang-Rhys-parameter* λ^2 , which descriptively defines the overlap in vibronic wave functions of involved vibrations of the ground and the excited state [65]. The continuous peaks indicate a broadening of the theoretical infinitely narrow transitions. Static and dynamic processes in gaseous, liquid and solid phases lead to a distribution of the transition energy of a single chromophore.

The lifetime Δt of a purely electronic excited state is limited. Therefore the energy of this radiative transition has a distinct uncertainty in energy ΔE . This width is called the *natural linewidth* and is described by the *Uncertainty Principle* [57]

$$\Delta E \propto \frac{\hbar}{\Delta t}. \quad (2.3)$$

The decay of this radiative transition is exponential and therefore the line shape is Lorentzian [57]. But still, this picture is not enough to describe the line shapes of optical transitions of chromophores. Multiple processes lead to further homogeneous (HLB) and inhomogeneous line broadening (IHLB), which is described below. Thereby HLB differs from IHLB in its affection on the system: if, in an ensemble of emitters, all chromophores are affected by a broadening mechanism in the same way, the broadening is assigned to HLB. For IHLB each chromophore is affected unequally and therefore the emitter becomes distinguishable. In the case of single chromophore this picture applies to e.g. spectral diffusion, which generates distinguishable emitters “in time” due to varying interactions with the local surrounding and shifts of the transition energies.

The homogeneous line broadening (HLB) or line width Γ_{hom} is described by

$$\Gamma_{\text{hom}} = \frac{1}{\pi T_2} = \frac{1}{2\pi T_1} + \frac{1}{\pi T_2^*(T)}, \quad (2.4)$$

where T_1 is the population decay time stated above and $T_2^*(T)$ accounts for temperature dependent pure dephasing processes [54, 55, 66]. This dephasing is due to interaction of the chromophore with its local environment (e.g. scattering of phonons) and leads to random shifts of the energy levels faster than the excited state lifetime. In gaseous phase this corresponds to the pressure broadening. At single molecule concentration this line width can be measured with sufficient time and spectral resolution. Furthermore at cryogenic temperatures the dephasing process is frozen out and the linewidth of the pure electronic transition (without any vibrational energy), the so called *zero phonon line* (ZPL), becomes the natural linewidth $\Gamma_{\text{hom}}^{\text{single}}$ limited by the excited state lifetime [67] (see Fig.2.3 (a)).

IHLB on the other side is caused by an averaging effect over a distribution of transition energies. For a single chromophore embedded in a solid amorphous matrix, fast reorganisation processes (but slower than T_1) of its local surrounding influence its dielectric environment (dynamic disorder)[9, 67]. Subsequently the interaction between the chromophore and its environment is a highly dynamical process, leading to randomly fluctuating energy levels. For insufficient experimental conditions this may cause an averaging of multiple transition energies and an inhomogeneously broadened absorption or emission. This is called “spectral diffusion” and can occur at sufficient temperatures on time scales from microseconds to multiple seconds (see Fig.2.3 (b))[7, 9, 67]. For an ensemble of chromophores, in liquid or solid phase, additional averaging due to each chromophore’s specific environment adds up to the inhomogeneous broadening (static disorder, see Fig.2.3 (c))[66]. Corresponding to an ensemble, polymer chains can exhibit different conjugation lengths resulting in different energetic levels [48, 68].

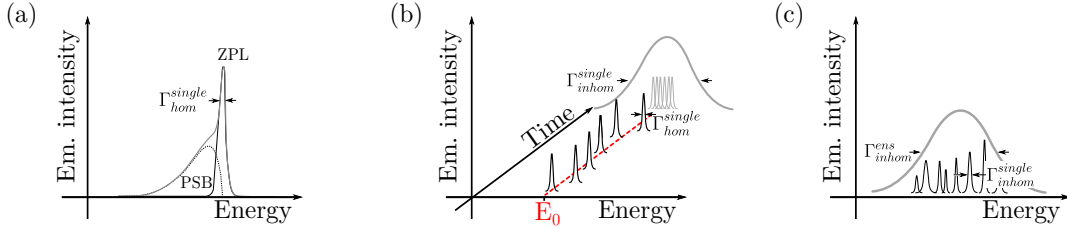


Fig. 2.3: Homogeneous and Inhomogeneous Line Widths of Single Chromophores and Ensembles. (a) Sketch of a single chromophore emission spectrum (solid, grey) of the homogeneous zero phonon line (ZPL, solid, black) and its corresponding phonon-side band (PSB, dashed). (b) Time dependent spectral diffusion around mean value E_0 of a homogeneous line (solid, black) and its resulting inhomogeneously broadened emission (solid, grey). (c) Inhomogeneously broadened emission of an ensemble sample (solid, grey) due to local variations of the environment of multiple chromophores with inhomogeneous line widths Γ_{inhom}^{single} (solid, black).

Depending on the interaction strength between the chromophore and its environment the inhomogeneous line widths can be either of Lorentzian or Gaussian shape.

Above mentioned processes can be measured under sufficient conditions. For polymers such as MeLPPP the ZPL and Γ_{inhom}^{single} get evident at cryogenic temperatures [53]. Here the PSB is mostly due to vibrations of the attached side groups of the polymers and the surrounding matrix. Averaging over multiple single MeLPPP at different positions in the sample agrees with ensemble measurements on MeLPPP (corresponding to Fig.2.3 (c)). Next to the ZPL further peaks are evident in low temperature spectra of conjugated polymers. These features are normally ascribed to electron-phonon coupling of vibrational modes of the chromophore itself. Energies of these modes range from 250 cm^{-1} for collective vibrations up to 1400 cm^{-1} for carbon bond stretching [48]. Time resolved measurements yield information about spectral diffusion and therefore about the energetic landscape. The jumps can occur on time scales faster than the excited state lifetime itself (pure dephasing processes T_2^*) up to several days or weeks. These jumps can be followed with a single molecule experiment, e.g. by continuously exciting single molecules and simultaneous detection of its spectral resolved fluorescence. This was already shown for smaller molecules like perylene bisimide [7] or bigger architectures like the light harvesting complex LH2 of *Rhodospseudomonas acidophila* [69].

Measurements on Dephasing. Ultrafast measurements such as coherent control schemes [20, 21, 70] or atto- to femtosecond pump-probe techniques [17, 71, 72] are able to get insights into ultrafast processes like dephasing, relaxation or excited state absorptions of CP and low-weight organic molecule. Holcman *et al.* [73] studied the purely electronic exciton in a single polydiacetylene (PDA) chain embedded in a crystalline matrix of its own monomer. Using a pair of phaselocked pulses (FWHM ≈ 1 ps) they find the temperature dependent (between 5 K and 50 K) effective dephasing

time T_2 (see Eq. 2.4) of the analysed emission distributed between 1 ps to 8 ps. The T_2 obtained by the temporal measurements are compared with the inverse line width of the emission, proving that dephasing has a much bigger influence on the line width, than the lifetime of the exciton. At room temperature this influence is even more significant. Brinks and Hildner *et al.* [21] used single terrylene diimide (TDI) molecules embedded in a polymethylmethacrylate (PMMA) film and also a phase-locked pair of identical pulses to generate and influence the coherence in this system at room temperature. The coherence decays within the first 300 fs after the first pulse transferred excitation probability to the first excited state, indicating strong dephasing due to high electron-phonon coupling to the matrix at ambient conditions. Using the Bloch-formalism (see section 2.5) they were able to track and manipulate the dynamics of their prepared coherent superposition state for any desired interpulse delay smaller than T_2^* .

Single chromophores exhibit multiple radiative and non-radiative transitions between electronic and vibrational (inter and intra molecular modes) states. Several spectral features are evident in emission and absorption spectra at high and low temperatures and range from the PSB, which accompanies the ZPL, to higher vibrational modes of the chromophore itself. These theoretical infinitely narrow lines are broadened due to (in)homogeneous processes in gaseous, fluid or solid states. In summary it should be emphasized, that dephasing processes have the biggest impact on a room temperature emission and absorption spectrum of a single chromophore. Inhomogeneous processes like spectral diffusion e.g. for a single emitter embedded in a solid amorphous matrix still have an effect on the line shape but are negligible in comparison to dephasing. Measurements on dephasing include fluorescence spectroscopy up to ultrafast schemes such as optical free induction decay measurements. Exemplary measurement techniques and result will be discussed at the end of section 2.5.

2.2 Quantum Mechanical Description of the Linear and Non-Linear Susceptibility

The interaction between matter and an EM field is characterised by the susceptibility of a material. By exposure of matter into the EM field the electrons inside the material are forced to move, which finally generates a polarisation P [55, 74]

$$\mathbf{P} = \epsilon_0 \left(\chi^{(1)} \mathbf{E} + \chi^{(2)} \mathbf{E} \cdot \mathbf{E} + \chi^{(3)} \mathbf{E} \cdot \mathbf{E} \cdot \mathbf{E} + \dots \right) \quad , \quad (2.5)$$

with ϵ_0 the dielectric constant, $\chi^{(i)}$ the susceptibility tensor of i th order and E the EM field. Depending on the power of the EM field the description in 2.5 can be simplified to

$$P = \epsilon_0 \chi^{(1)} E \quad , \quad (2.6)$$

which is sufficient enough to describe linear processes, such as simple one-photon (1P) absorption, with the generated polarisation P oscillating at the same frequency as the interacting external field ω . However, the focus of this work is on two-photon (2P) absorption processes, which is clearly a non linear problem. At this stage, the material mediated interaction of EM fields can not be treated independently for each component any more. In other words, a non linear process of n th order, will generate n mixed up components of the polarisation. A figurative example is *second harmonic generation* (SHG), a $\chi^{(2)}$, where two EM field components (ω_1, ω_2) generate a matter polarisation oscillating at $\omega_1 + \omega_2$. Therefore the description in Eq.2.5 finally reads for SHG

$$P_n = \epsilon_0 \left(\sum_j \chi_{nj}^{(1)} E_j(\omega_1) + \sum_{j,k} \chi_{njk}^{(2)} E_j(\omega_1) E_k(\omega_2) + \dots \right) \quad . \quad (2.7)$$

The summation in 2.7 runs over each vector component of the EM field E_l of frequency ω_m . However, this work is about the 2P absorption process and the non-linear susceptibility contributing to this is $\chi^{(3)}$.

$$P_n = \epsilon_0 \left(\sum_j \chi_{nj}^{(1)} E_j(\omega_1) + \sum_{j,k} \chi_{njk}^{(2)} E_j(\omega_1) E_k(\omega_2) + \sum_{j,k,l} \chi_{njkl}^{(3)} E_j(\omega_1) E_k(\omega_2) E_l(\omega_3) + \dots \right) \quad . \quad (2.8)$$

Most of the CP exhibit centro symmetric symmetry (see section 2.3) and therefore the lowest non linear χ , these polymers can exhibit, is indeed $\chi^{(3)}$. The polarisability of centro symmetric structures (here MeLPPP) must flip the sign if the sign of the external EM field is reversed. For an even order χ this is only true for $\chi = 0$. This in turn means that all susceptibilities of order $2n$ ($n = 1, 2, 3, \dots$) vanish. Both linear and non-linear susceptibilities can be derived from the time-dependent Schrödinger equation in first and second order perturbation theory, which is briefly shown in the two following parts.

Linear Susceptibility

The problem of light matter interaction has to be derived in the picture of time-

dependent perturbation theory [55, 75]. The perturbed (in general time-dependent) Schrödinger equation reads

$$i\hbar \frac{\partial}{\partial t} |\Psi\rangle = (H_0 + H^S) |\Psi\rangle, \quad (2.9)$$

with H_0 is the unperturbed Hamiltonian of the system, H^S the perturbation and Ψ reflects the (in general time and spatial dependent) total wave function.

$$|\Psi\rangle = \sum_{\zeta=j,f}^{\infty} c_{\zeta}(t) |\psi_{\zeta}^0\rangle \quad (2.10)$$

Ψ is a linear combination of the unperturbed solutions ψ_{ζ}^0 multiplied by their time dependent coefficients $c_{\zeta}(t)$. Solving 2.9 for the absorption process in a two level system (see Fig. 2.4 (a)) with all population concentrated in the initial state $|\psi_j\rangle$ at $t = 0$, yields a differential equation for the $c_{\zeta}(t)$. If the difference between the initial conditions for $t = 0$ ($c_j(0) = 1$ and $c_f(0) = 0$, see Fig. 2.4 (a)) and for $t > 0$ is insignificantly small (which is small population transfer from the initial to the final state), the square value $|c_{\zeta}(t)|^2$, which is a measure for the population probability of the respective state, can be calculated using

$$c_f(t) = -\frac{1}{2} H_{fj}^S(0) \left\{ \frac{e^{i(\omega_{fj}+\omega)t}}{\omega_{fj} + \omega + i\gamma_f} + \frac{e^{i(\omega_{fj}-\omega)t}}{\omega_{fj} - \omega - i\gamma_f} \right\} \quad (2.11)$$

with $H_{\sigma\zeta}^S = \langle \psi_{\sigma}^0 | H^S | \psi_{\zeta}^0 \rangle$, $\omega_{fj} = \frac{1}{\hbar} (E_f - E_j)$ and the relaxation rate γ_f from the final state $|\psi_f^0\rangle$. For the interaction of a total electric dipole moment $\hat{\mathbf{p}} = e \sum_m \hat{\mathbf{r}}_m$ (e elementary charge) with an EM field $\mathbf{E} = \mathbf{E}_0 \cos(\omega t)$ the perturbation becomes $H^S = -\hat{\mathbf{p}} \cdot \mathbf{E}_0 \cos(\omega t)$. Finally, calculation of the quantum mechanical polarisation

$$P_{\text{qm}} = \frac{N}{V} d(t) = -\frac{N}{V} \left\{ c_j^* c_f \langle \psi_j^0 | \hat{\mathbf{p}} | \psi_f^0 \rangle e^{-i\omega_{fj}t} + c_f^* c_j \langle \psi_f^0 | \hat{\mathbf{p}} | \psi_j^0 \rangle e^{i\omega_{fj}t} \right\} \quad , \quad (2.12)$$

which is product of the number density $\frac{N}{V}$ and the induced electric dipole moment $d(t)$ of state $|\Psi\rangle$, and subsequent component comparison to the macroscopic polarisation

$$P(t) = \frac{1}{2} E_0 \left\{ \chi(\omega) e^{-i\omega t} + \chi(-\omega) e^{i\omega t} \right\} \quad , \quad (2.13)$$

yields the linear susceptibility

$$\chi^{(1)} = \frac{e^2}{3\epsilon_0 \hbar} |\mathbf{n} \cdot \hat{\boldsymbol{\mu}}_{fj}|^2 \left(\frac{1}{\omega_{fj} - \omega - i\gamma_f} + \frac{1}{\omega_{fj} + \omega + i\gamma_f} \right) \quad , \quad (2.14)$$

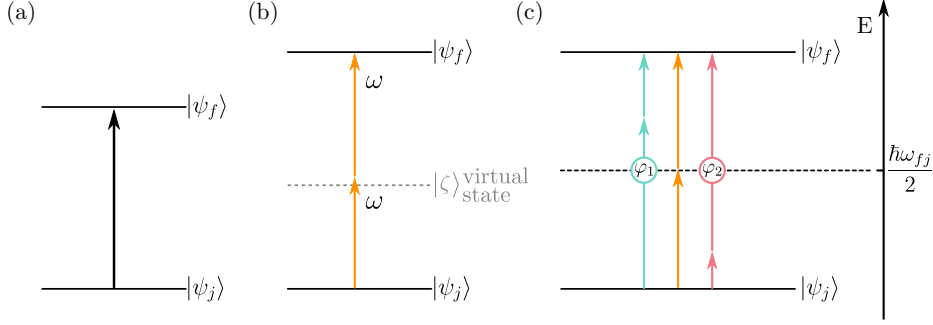


Fig. 2.4: One- and Two-Photon Absorption. (a) One-photon absorption process between two singlet states S_0 (ψ_i) and S_1 (ψ_f). (b) Two-photon (2P) absorption process between the singlet ground state S_0 , a short lived virtual state (grey dashed) and a higher excited singlet state S_n with $n > 2$. (c) 2P absorption between the singlet ground state S_0 and excited state S_1 for three exemplary excitation energy combinations. The orange one resembles the same as in (b) with $\omega_1 = \omega_2 = \omega$, with light blue and light red are composed of differing energies and distinct phases φ_1 and φ_2 . The dashed line marks the half of the transition energy.

where the *rotating wave approximation* (RWA) was used. \mathbf{n} denotes the polarisation of the EM field ($\mathbf{n} \parallel \mathbf{E}_0$), γ_f the spontaneous decay rate of the excited state $|\psi_f^0\rangle$ and $\hat{\boldsymbol{\mu}}_{fj}$ is the transition dipole matrix element which was introduced before and reads in general

$$\hat{\boldsymbol{\mu}}_{fj} = \langle \psi_f^0 | \hat{\mathbf{p}} | \psi_j^0 \rangle \quad . \quad (2.15)$$

From the susceptibility we can derive dielectric properties such as the refractive index $\eta(\omega)$ and the extinction coefficient $\kappa(\omega)$ with [55]

$$[\eta(\omega) + i\kappa(\omega)]^2 = 1 + \chi(\omega). \quad (2.16)$$

A measure for the number of absorbed photons or the interaction of the molecule/CP with the external field is the absorption cross section [16]

$$\sigma^{(lin)}(\omega) = \frac{\kappa(\omega) \ln(10)}{N_A}, \quad (2.17)$$

with N_A the *Avogadro* constant. For *para*-phenylene-type polymers it was found, that these absorption cross sections are around $10^{-15} - 10^{-14} \text{ cm}^2$ [50]. Low molecular-weight organic dye molecules exhibit smaller values around $10^{-17} - 10^{-16} \text{ cm}^2$ [67, 76].

Non-Linear Susceptibility

The first time 2P absorption has been reported was 1931 by Maria Göppert-Mayer in her theoretical analysis by second order perturbation theory [56]. In particular, 2P absorption is a $\chi^{(3)}$ process (which means the generated polarization is a result

of three different frequencies $\omega_1, \omega_2, \omega_3$ in the most general case). The calculation of $\chi^{(3)}$ is analogous to the steps made before with all the population concentrated in the initial state at $t = 0$. Therefore the second order perturbation solution yields the wave function coefficient [75]

$$c_f^{(2)}(t) = \frac{1}{\hbar} \frac{e^{i\omega_{fj}t} - 1}{\omega_{fj}} \sum_{\zeta} \frac{H_{f\zeta}^S(0) H_{\zeta j}^S(0)}{E_{\zeta} - E_j} , \quad (2.18)$$

with applied RWA and therefore

$$|c_f^{(2)}(t)|^2 = \frac{4 \sin^2(\omega_{fj} \frac{t}{2})}{\hbar^2 \omega_{fj}^2} \left| \sum_{\zeta} \frac{H_{f\zeta}^S(0) H_{\zeta j}^S(0)}{E_{\zeta} - E_j} \right|^2 . \quad (2.19)$$

The indices run through all intermediate states $|\zeta\rangle$, which take part in the 2P absorption from the initial to the final state. Comparison to Eq.2.11 shows that only the last part on the right side is different between the first and second order coefficients.

However, from this point the calculations become complex, as the contributing EM field components of different ω_i can not be treated independently any more. Already the combination of all involved frequencies for a $\chi^{(2)}$ process (for example *second harmonic generation*) produces a very lengthy expression [55] for the polarisation. Clearly, the expression for $\chi^{(3)}$ is even more extensive and must not be fully presented in this work. A further simplification is the assumption of an 2P absorption process between two states with a monochromatic excitation (one colour 2P absorption of ω). The imaginary part of the susceptibility simplifies to [55, 74] (a full expression can be found e.g. in [74, 77])

$$\text{Im}(\chi^{(3)}) = \frac{\pi e^4}{3\epsilon_0 \hbar} \left| \sum_{\zeta} \frac{(\mathbf{n} \cdot \boldsymbol{\mu}_{f\zeta})(\mathbf{n} \cdot \boldsymbol{\mu}_{\zeta j})}{\omega - \omega_{\zeta}} \right|^2 . \quad (2.20)$$

The summation on the right hand side of Eq. 2.20 is again through all intermediate electronic levels of the material. In the special case of non resonant 2P absorption this describes the absorption of a single photon of energy ω into the short-lived (10^{-15}) virtual state. If the intensity of the incident EM field is high enough ($10^6 \frac{\text{W}}{\text{cm}^2}$ to $10^9 \frac{\text{W}}{\text{cm}^2}$), the probability of an absorption of a second photon, during the lifetime of the virtual state, is finite leading to the population of the final state. In Fig. 2.4 (b) a sketch of the non resonant 2P absorption is pictured. The first transition takes place into the virtual state $|\zeta\rangle$ from where the second transition into the final (excited) state occurs. Note that the process shown, is a special case with the participating EM fields are of same energy ω and $2\omega = E_f - E_j$. The resonant 2P absorption on the other side, describes the situation of a primary transition into a real electronic level of the

interacting matter from where the second transition can be induced. The longer lifetime of the real intermediate state enhances the probability of the second transition strongly [78, 79].

The above discussed cases of 2P absorption only account for a monochromatic excitation. Usually the excitation source in measurements of ultrafast processes is pulsed and therefore the spectrum is a continuous distribution of energies. Thus multiple combinations of frequencies will contribute to the 2P transition simultaneously. This is qualitatively pictured in Fig.2.4 (c) for three different cases of 2P transitions. The orange case reflects the same as in (b) with $\omega_1 = \omega_2$ and the remaining for $\omega_1 \neq \omega_2$. Besides the orange case the possibility is given now, to induce the transition via the left and the right excitation pathway. The induced polarisation therefore exhibits the phase information of all involved EM fields. For the sake of simplicity only two excitation pathways, light blue and red with phases $\varphi_{1,2}$ are considered. Depending on the particular phase φ_1 and φ_2 of the interacting EM field components the induced polarisations will interfere de- or constructively as function of the relative phase. This is called *excitation pathway interference* and will finally result in a modulated 2P transition probability. This will be important for Section 4.3 in Chapter 4, where excitation pathway interferences play a key role, to understand the ultrafast dynamics of the analysed system.

In analogy to $\chi^{(1)}$, the absorption cross section $\sigma^{(nl)}$ is for the non-linear problem proportional to $\text{Im}(\chi^{(3)})$, too. Values range from 10000 – 10 GM (1 Goepfert-Mayer/GM = $10^{-50} \frac{\text{cm}^4 \text{s}}{\text{photon molecule}}$) for CP and organic dyes [50, 80, 81]. The technical possibilities synthesizing CP allows for tuning stiffness and conjugation lengths. Subsequently the symmetry is a highly adjustable parameter and CP can exhibit large 2P absorption cross sections [78, 82]. Applications of 2P absorption range from spectroscopic techniques, to study high lying electronic states [38, 51, 53, 83] to micro fabrication [84, 85]. Microscopic techniques take also advantage of this property. Both, the power dependent 2P absorption probability as well as σ^{nl} is highly material dependent, a better spatial resolution can be achieved by this selective excitation [86, 87].

2.3 Group Theory of Organic Molecules

As discussed in section 2.1 and 2.2 the structural symmetry plays an important role in the symmetry of a state's wave function and therefore in the 1P and 2P absorption process. In the following group theory of organic molecules, which is an advantageous tool for understanding molecular transitions, will be discussed. This is followed

by application of the knowledge to the real molecular compounds, MeLPPP and S-CBT.

Symmetry Selection Rules

Selection rules are a very helpful tool in order to find out if a transition takes place or not. In general the exact value of the transition matrix dipole element (see Eq.2.14, 2.20) has to be known to characterize an optical transition. For many body systems, such as CPs or even only low molecular-weight organic molecules, this calculation is extremely complex. For an optical transition the wave functions of the initial state (ground state) and the final state (electronic, vibronic) need to be computed to solve the integral in μ_{fj} . However only the knowledge if a transition is allowed or not is usually enough to serve the purpose.

In general there are two different selection rules for optical processes: (i) spin and (ii) symmetry selection rules [39]. Former does not need to be defined exactly, but describes in general the spin conservation of the transition dipole matrix element. This ends up in a quantum mechanical prohibition for transitions between states with different spin multiplicities (e.g. between singlet and triplet states). However, as stated before, multiple *spin-orbit coupling* processes can generate states with mixed spin multiplicities [16, 40]. Therefore a non vanishing probability for a transition with a change in spin exists [17, 88].

Symmetry selection rules. Additional selection rules apply to spin-allowed transitions. Depending on the symmetry of the involved state's wave function, whether its sign is changed or retained under distinct symmetry operations, the transition matrix dipole element vanishes or not. Group theory is an easy and straightforward way to describe the symmetry behaviour of electronic states. Primarily the chromophore, or molecule is assigned to a distinct *point group*. This point group specifies the symmetry operations, which can be done without making the structure before and after the operation distinguishable. Basically there are five symmetry operations, which can be applied to the structure [89, 90].

- Identity element of symmetry I : This operation applies to all structures and leaves the conformation unchanged. I is equivalent to C_1 , an one-fold rotation (through 2π) of the molecule.
- Centre of symmetry i : Also known as *inversion*, this operation inverts all positions of the molecules atoms sign $((x, y, z) \rightarrow (-x, -y, -z))$. But still the final structure is indistinguishable from the initial one (see Fig.2.5 (b)).
- Axes of symmetry C_m : The clock-wise rotation by $\frac{2\pi}{m}$ which leaves the molecule unchanged is denoted with a C_m rotation axis (see Fig.2.5 (c))

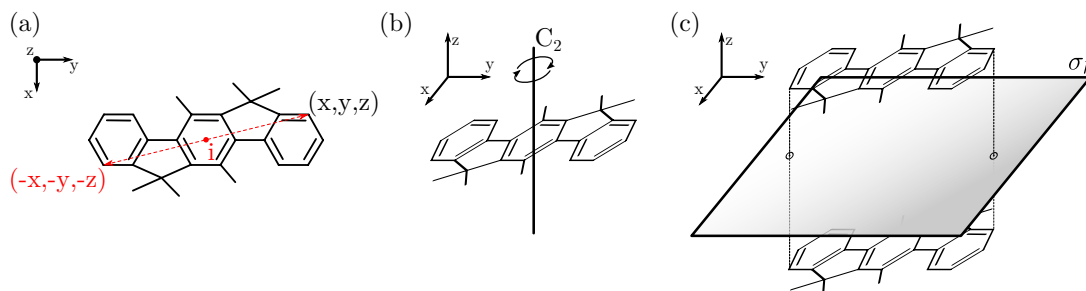


Fig. 2.5: Symmetry Operations on a Monomer Unit of Methyl Substituted Ladder-Type Poly(*para*-phenylene) (MeLPPP). (a) Inversion operation on MeLPPP through its inversion center (red full circle). Side groups are neglected for the sake of clarity. (b) Two times rotation by π on MeLPPP performed by the two-fold rotation axis C_2 . (c) MeLPPP is reflected at its mirror plane σ_h .

- Plane of symmetry σ : All two-dimensional molecules have a plane of symmetry, which does not change the structure. A mirror plane perpendicular to the axis of symmetry C_m with highest order m is labelled with h (see Fig.2.5 (a)). If C_m coincides with the plane of symmetry it is denoted as σ_v .
- Rotation-reflection axis of symmetry S_m : If a rotation through $\frac{2\pi}{m}$ followed by a reflection at a mirror plane perpendicular to that rotation axes results in an indistinguishable final structure, the molecule exhibits a S_m rotation-reflection axis.

In the following the identification of point groups and therefore irreducible representations and symmetry elements are shown on the example of MeLPPP, which is important for the experimental part of this work. After the detailed explanation for MeLPPP, the findings obtained will be applied to the S-CBT molecule. Without any further knowledge of photophysical calculations of both compounds, the gained information will be helpful for discussions later on.

Group Theory Analysis on MeLPPP. As a first example the monomer unit of the MeLPPP CP is chosen and shown in Fig.2.5. MeLPPP possesses a centre of inversion (Fig.2.5 (b)) in the middle of the central phenyl ring, a two-fold symmetry axis (set to coincide with the z -axis, Fig.2.5 (c)) through i and parallel to the xy -plane a mirror plane σ_h (perpendicular to the z -axis, Fig.2.5 (a)). According to [89] this molecule belongs to the non-degenerate point group C_{2h} . C_{2h} is an *Abelian* group, indicating the commutation of all symmetry operations (elements). The order of the group sticks to the total number of elements and is for C_{2h} 4. If two multiplied elements produce another one of the group, they are called *generating* elements (σ_h results from the combination $C_2 \times i$). Furthermore *symmetry species* (which apply to the wave functions later on) can be derived. These species are assigned according to their behaviour under symmetry operations of the generating elements. If one species is

symmetric (antisymmetric) to the primary axis (here C_2) rotation it is labelled with A (B). Depending on symmetric or anti-symmetric behaviour under the inversion i , A or B receives the subscript g (*gerade*) or u (*ungerade*), respectively (this property is called parity). Therefore C_{2h} contains 4 symmetry species, also called *irreducible representations*, with A_g, A_u, B_g, B_u .

Symmetry Relations for Wave Functions. Next to structural symmetry, the (pure electronic) wave functions of the individual states can be classified by group theory, too. The results can straightly be transferred to the chromophore units of the CP, as these are only translation invariant multiples of the monomer unit. The wave function with highest symmetry is always the equilibrium state, in this case the electronic ground state. As the symmetry species A_g is totally symmetric under all symmetry elements, this species is identified with the electronic ground state S_0 . For oligomers and CPs the symmetry of electronic states alternates with higher energies [40, 45, 91], identifying the lowest excited singlet states S_1 with a B_u species, in this case. The new state notation follows $n^M X_S$, with n enumerating the electronic state of one symmetry species according its energy, M is the spin multiplicity, X_S the symmetry species defined before. The pure electronic ground state S_0 , for example, finally reads $1^1 A_g$.

An electronic transition (therefore also 1P absorption) only takes place if the transition dipole matrix element in Eq.2.15, with $\hat{\mathbf{p}} = (\hat{p}_x, \hat{p}_y, \hat{p}_z)$, does not vanish. As the integral in Eq.2.15 runs over the whole space, the total product needs to be totally symmetric or in other words an even function of the electron coordinates. Finally this symmetry conditions depends strongly on the symmetries of the initial and final states wave function and the dipole operator. Following [92], at least one of the elements in Eq.2.15 must be totally symmetric. The symmetry components of the dipole operator is dependent on the point group itself. For C_{2h} $\hat{\mathbf{p}}$ reads [92]

$$\Gamma(\hat{\mathbf{p}}) = \begin{pmatrix} B_u \\ B_u \\ A_g \end{pmatrix}, \quad (2.21)$$

with $\Gamma(O)$ describing the irreducible representation of its argument O . As the transition dipole moments of CP are elongated along the polymer backbone, we can neglect the z -component in Eq.2.21, whereas both, the x - and y -component are interchangeable and therefore will be both included in the further considerations:

$$\begin{aligned} \Gamma(\psi_f) \times \Gamma(\hat{p}_{x,y}) \times \Gamma(\psi_j) &\stackrel{!}{=} A_g \\ \Gamma(\psi_f) \times B_u \times A_g &= A_g \quad \text{with} \quad \Gamma(\hat{p}_{x,y}) = B_u \quad . \end{aligned} \quad (2.22)$$

The product of an even and uneven species generates an uneven species. Accordingly $\Gamma(\psi_f)$ of the final states must be B_u for the 1P transition from the ground state 1^1A_g .

For a 2P transition the considerations are in analogy to the previous ones. The dipole operator $\hat{\mathbf{p}}_{2P}$ is now a 3×3 tensor and the stated problem has to be solved for each component of the tensor [92].

$$\Gamma(\hat{\mathbf{p}}_{2P}) = \begin{pmatrix} A_g & A_g & B_g \\ A_g & A_g & B_g \\ B_g & B_g & A_g \end{pmatrix} \quad (2.23)$$

Again, we can neglect all components in the z -direction and only xx, yy, xy, yx are of importance. In contrast to 2.22 the calculations reads now

$$\Gamma(\psi_f) \times A_g \times A_g = A_g \quad . \quad (2.24)$$

Finally the final state ψ_f must be of even symmetry to fulfil the condition for the transition dipole matrix element, i.e. A_g .

In other words, the 1P transition from the electronic ground state, is only allowed if the target state is of total uneven symmetry. In contrast, the 2P transition from 1^1A_g will only take place when the final state is of the same symmetry species as the ground state, i.e. A_g . Linear and non-linear absorption spectroscopy measurements have proven that the first excited singlet state is indeed of uneven symmetry B_u . In contrast, the next excited singlet state (i.e. the second excited state) is of even symmetry A_g and accessible by 2P absorption [38, 93].

The previous considerations have been made on the assumption that all processes are purely electronic. Hildner et al. [51, 93] have shown that, whether a 1P or 2P process is induced (from the vibronic ground state in 1^1A_g), the vibrational level has to be a totally symmetric species (a_g). On the example of 1P absorption this means

$$\begin{aligned} \Gamma(\psi_f) \times \Gamma(\nu_f) \times \Gamma(\hat{\mathbf{p}}_{x,y}) \times \Gamma(\psi_j) &\stackrel{!}{=} A_g \\ B_u \times \Gamma(\nu_f) \times B_u \times A_g &= A_g \\ \rightarrow \Gamma(\nu_f) &= a_g \end{aligned} \quad (2.25)$$

with $\nu_{f,j}$ denoting the vibrational state of the final or initial level and lower case a_g is the irreducible representation for a vibronic level.

Group Theory Analysis on S-CBT. Next to the conjugated polymer MeLPPP another compound, called S-CBT, was analysed. For the understanding of the ultrafast measurements, the symmetry considerations made above have to be applied to S-CBT,

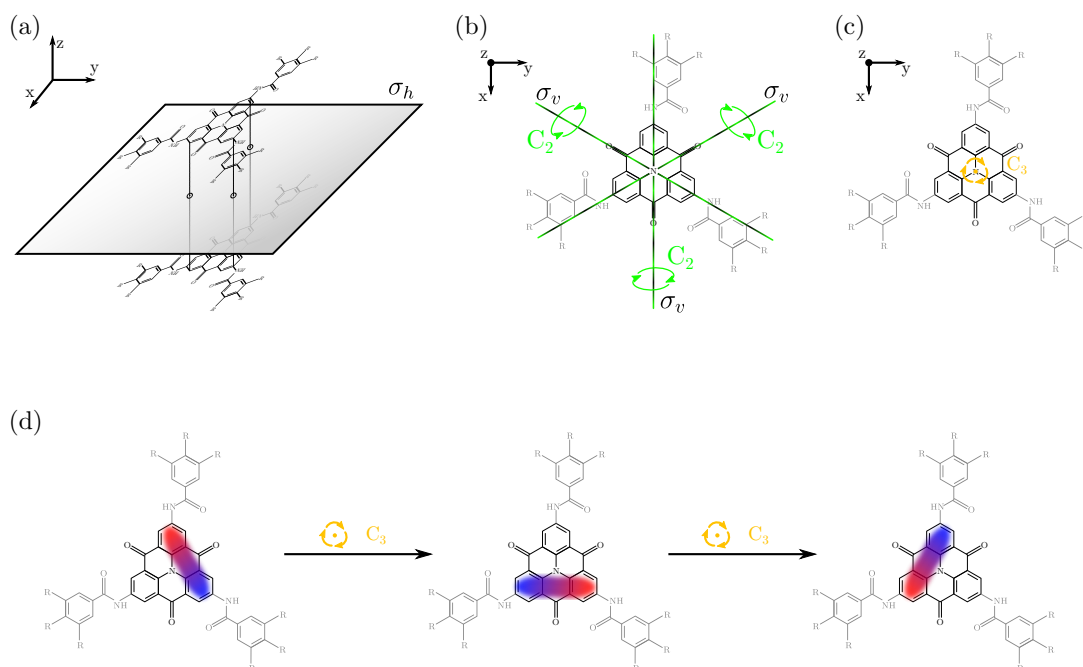


Fig. 2.6: Symmetry Operations on an Individual Carbonyl-Bridged Triarylamine Derivative. (a) Carbonyl-bridged triarylamine derivative with *s*-chiral side chains (S-CBT, side groups are neglected for the sake of clarity) is reflected at its mirror plane σ_h . (b) Three different two-fold rotation axes parallel to the x - y -plane (green) and three different mirror planes containing the principle axis (black). Both, planes and axes coincide, therefore the lines are coloured black and green simultaneously. (c) Three times rotation by $\frac{2}{3}\pi$ on S-CBT performed by the three-fold rotation axis C_3 (orange full circle) parallel to the z -axis.

too (see Fig.2.6). Following the instructions shown before, group theory analysis of this compound will be briefly done in the next section. Fig. 2.6 shows the symmetry elements which can be operated on the S-CBT system, without changing its appearance. It is important to note, that these operations are applied to the core of S-CBT, as the side groups (shown in grey in Fig. 2.6 (b),(c)) contribute only a minor part to the optically active orbitals and are therefore negligible. Haedler *et al.* performed measurements on a comparable compound but without any aromatic side groups, showing the same spectral characteristics as S-CBT [94]. This is further supported by the fact, that the side groups (the aromatic benzene rings) are attached to the core only by three single bonds, whose electronic coupling is not strong enough.

The core exhibits multiple proper rotation axes: one C_3 and three times C_2' (2.6 (c) and (b)). The highest order of the existing rotation axes is 3. The C_2' are perpendicular to that three-fold axis (prime superscript) and additionally a mirror plane, also perpendicular to C_3 , denoted with σ_h exists (Fig.2.6 (a)). Three more mirror planes are spanned by a combination of the z - and x, y -axes (σ_v), containing the principle axis (Fig.2.6 (b))

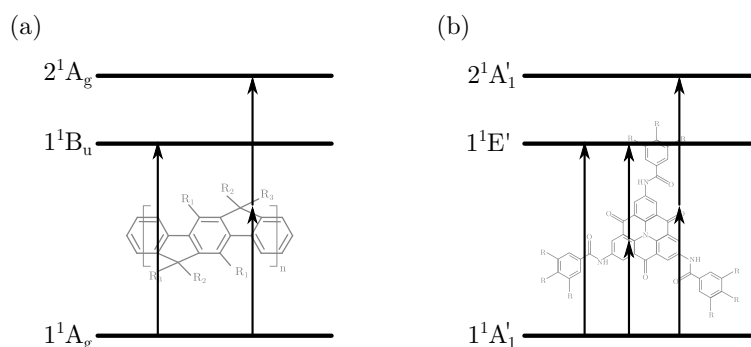


Fig. 2.7: Allowed 1P and 2P Transitions. (a) Simplified energy level diagrams of the ground state 1^1A_g , the first 1^1B_u and second excited singlet state 2^1A_g of MeLPPP (grey structure in the background) and the symmetry allowed 1P and 2P transitions pictured with the arrows. (b) Symmetry allowed 1P and 2P transitions in S-CBT (grey underlaid structure) and respective simplified energy levels of ground state $1^1A'_1$, higher excited singlet states $1^1E'$ and $2^1A'_1$. Note the subscript 1 describes the symmetry to the C_2 axis, with the prime standing for symmetric behaviour in dependency of the mirror plane σ_h .

black lines). Execution of C_3 and σ_h afterwards generates an improper rotation axis S_3 (not shown in the picture). With these symmetry elements S-CBT belongs to the degenerate D_{3h} point group of order 12.

The degeneracy can be understood in terms of linear combinations: if an irreducible representation can be produced by a linear combination of others of the same group (by carrying out symmetry operations) this representation is called degenerate and denoted with E . This can be applied to the figure of the density of electrons distributions. If two electronic states have the same energy as other ones and can be transferred to each other by, e.g., a proper C_3 rotation the states are degenerate. This example is shown in Figure 2.7 (d) for an exciton located on one part of the S-CBT core. This degeneracy effects complicate the symmetry considerations. However, this problem still can be solved with proper calculations, which can be found in the appendix A.1. The result shows that a 2P absorption from the totally symmetric ground state $1^1A'_1$ is allowed to states with the same symmetry A'_1 and also to degenerate states with non-total symmetry E' . In contrast a 1P transition from the ground state is only possible to electronic states with E' (see Fig.2.7). Hence the same state of symmetry E' can be populated by a 1P or 2P transition from the ground state in S-CBT (see later on in Chapter 5).

Figure 2.7 sums up the results, which have been obtained only by symmetry considerations. In the linear CP MeLPPP (2.7 (a)) the first excited singlet state is only accessible via an 1P absorption, which will be visible in conventional spectroscopy experiments [51, 53]. The second excited single state exhibits an even symmetry, which is 1P forbidden but 2P allowed from the ground state [38, 51, 93]. On the contrary

S-CBT exhibits a more complex behaviour due to the two dimensional structure (Fig.2.7 (b)). Population from the ground state can be directly transferred to excited singlet states by both, 1P and 2P absorption. However, there are still states which are only 2P allowed and 1P forbidden. Note that these rules are strictly valid for completely fulfilled symmetry properties. If any symmetry is broken, due to any stress induced by solid surroundings or flexible side groups, the selection rule is soften. Therefore, in real systems it is possible to induce, if however with small probability, transitions between states with theoretically vanishing transition dipole moment.

2.4 Aggregation and Two-Photon Accessible States

In this section an introduction into the interaction between transition dipole moments and the subsequent change of photophysical properties is briefly discussed. For a part of the experimental work this knowledge is advantageous and surely helps to discuss the measured effects in supramolecular structures.

Different theoretical models exist in order to describe the interaction in molecular aggregates. The *Kasha* model [95] is very successful in calculating the photophysical properties of a variety of molecular aggregates. In this picture, the interaction is limited to purely Coulombic coupling. Starting from the point-dipole approximation for the coupling of two individual transition dipole moments, two types of aggregates are derived [65]

$$J_C = \frac{\boldsymbol{\mu}_1 \cdot \boldsymbol{\mu}_2 - 3(\boldsymbol{\mu}_1 \cdot \hat{\mathbf{e}}_R)(\boldsymbol{\mu}_2 \cdot \hat{\mathbf{e}}_R)}{4\pi\epsilon R^3} \quad , \quad (2.26)$$

where the transition dipole moments $\boldsymbol{\mu}_{1,2}$, the dielectric constant of the surrounding ϵ and the center of mass connecting displacement vector $\mathbf{R} = \mathbf{e}_r R$ was used. Whether J_C in Equation 2.26 is < 0 or > 0 a *J-type* or *H-type* aggregate is formed. This distinction is based on the relative angle between the two dipoles, which is reflected by the scalar product of the dipole moments and the displacement vector. The different $\boldsymbol{\mu}_i$ are arranged in J-aggregates “head-to-tail” like, whereas for the H-type structures the transition dipole moments are positioned “side-to-side”. Even though this model is able to describe the photophysics of a big part of molecular aggregates it still has two major shortcomings. On one hand, the whole interaction is based on the Coulombic interaction, which is only through space. However, for many molecular aggregates the distances between the subunits is small enough and efficient overlap of the wave function can occur. On the other hand, a more detailed analysis of the vibronic- or electron-phonon coupling must be included to describe more quantitatively spectral features in H- and J-type aggregates [65].

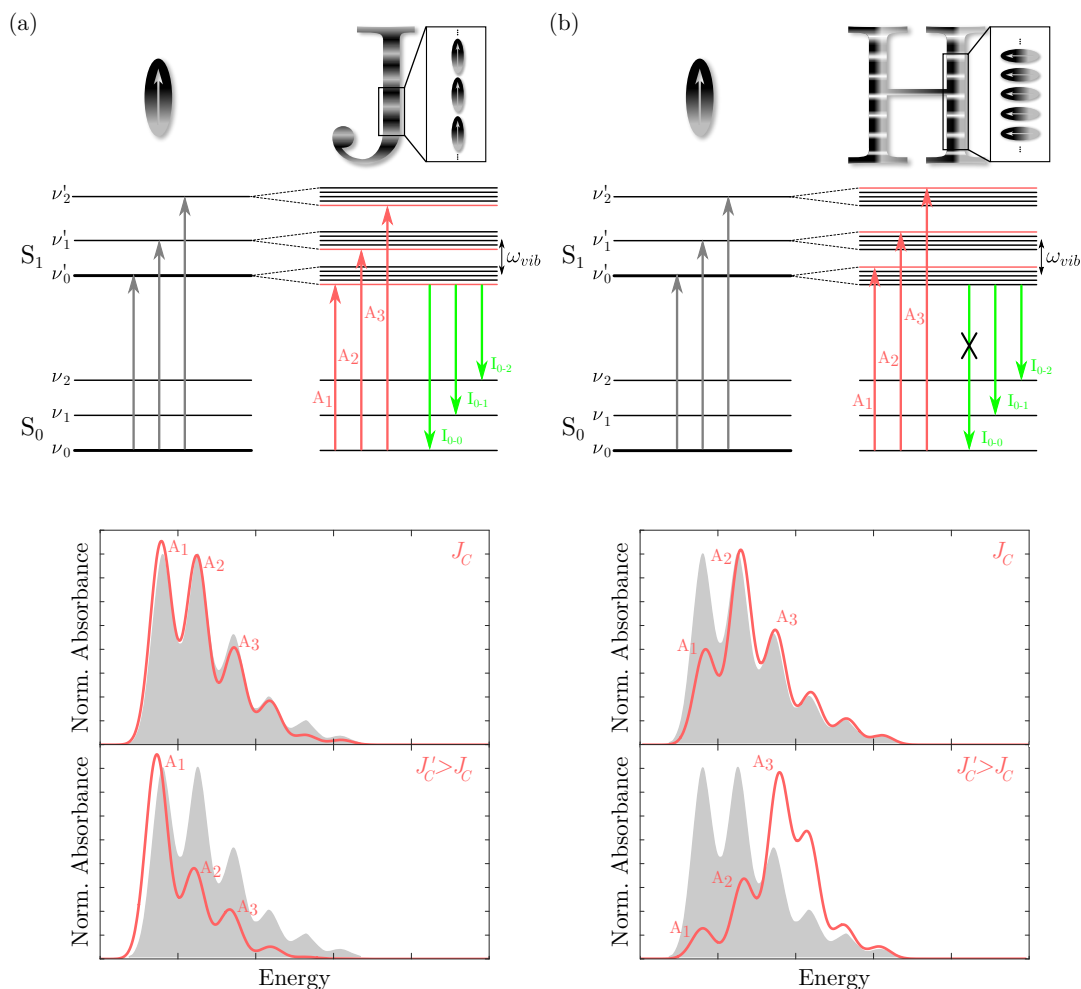


Fig. 2.8: Schematic Energy Diagram and Absorption for Ideal J- and H-Type Aggregates. (a): J-type aggregates; (b): H-type aggregates. Upper third : Scheme of a single chromophore and a “head-to-tail” (“side-to-side”) arranged J-type (H-type) structures. Mid third: Schematic energy level diagrams; each electronic ($S_n, n > 0$) and vibronic level ($\nu_n, n \geq 0$) of a single chromophore (black single lines with grey arrows) forms exciton bands (multiple packed lines) upon aggregation. The transition from the ground state S_0, ν_0 (red arrows) is only allowed into the lowest (highest) exciton level (red horizontal lines) for ideal J(H)-aggregates. The radiative transitions (green arrows) take place from the lowest level in the lowest exciton band to each level in the electronic ground state. Except the zero phonon transition for H-type structures, which is forbidden by symmetry reasons (crossed arrow, only for PL). Lower third: schematic absorption ($A_{1,2,3}$) of the monomolecular unit (grey filled area) and the aggregate for two couplings J_C and $J'_C > J_C$.

The simple picture above was extended by Spano and co-workers and published in several publications [65, 96, 97]. Many aromatic molecules exhibit strong vibronic progressions in their spectral characteristics. These features are mostly due to electron-phonon coupling of the intra-molecular carbon bond stretching modes of the aromatic groups (typically around 1200 cm^{-1} to 1600 cm^{-1} [29, 48, 68, 94]). These vibrational energies need to be included into the theory in order to describe the photophysics in agreement with experiments. Starting from the Frenkel-Holstein Hamiltonian a set of quantitative expressions of wave functions and energies is obtained, which are dependent of at least four parameters: the vibrational energy of the vinyl-stretching mode ω_{vib} , the free exciton bandwidth $W = 4J_C$, the number of chromophores N and the Huang-Rhys-parameter λ^2 [65]. Energetic disorder can be included and affects the photophysical properties of the aggregates as well. Comparison of W with the relaxation energy $\lambda^2\omega_{vib}$ opens up the distinction between strong and weak “excitonic coupling regimes” ($\lambda^2\omega_{vib} > W$ strong coupling; $\lambda^2\omega_{vib} < W$ weak coupling).

The most important results are summed up in Fig.2.8 for the J- and H-type aggregates in (a) and (b) respectively. In the upper third of the picture the ideal arrangement for J-type (head-to-tail) and H-type aggregates (side-to-side) is sketched (zoomed inset). The left energy level diagram of the second third reflects in each case the energy landscape of a single chromophore, with the right part representing the energy level diagram for the aggregated situation. In contrast to Kashas model [95], each of the vibronic levels ($\nu_{0,1,2,3,\dots}$) splits up into multiple states (from now on denoted as exciton manifold). If J_C increases, these exciton manifolds move together until only one single dense packed band is left. For ideal J-aggregates the oscillator strength (which is a measure for the probability of absorption) is completely concentrated in the lowest levels (red shifted to single molecule absorption) of each manifold (red coloured levels in Figure 2.8). At temperatures of $T = 0\text{ K}$ the emission follows Kashas rule and takes place from the lowest excited state of the lowest manifold into the vibrational levels of the ground state. In contrast, the absorption for H-aggregates is only allowed to the upper edge (blue shifted) of each exciton manifold. Still the emission occurs only from the lowest excited singlet state. However, the zero-phonon transition is not allowed by symmetry reasons. For both type of aggregates this selective absorption is due to the destructive interference of the phases of the interacting transition dipole moments. For H-type (J-type) structures this absorptive level is blue (red) shifted. In the last third of Fig.2.8 (a) and (b) schematic absorption spectra are shown of the single chromophore (grey filled area) and the aggregates (red solid line) in dependency of weaker (stronger) coupling in the upper (lower) absorption spectrum. For head-to-tail arranged molecules, the absorption of the zero-phonon peak increases whereas the oscillator strength of

the vibronic progression decreases (leading to a bigger ratio $\frac{A_1}{A_2}$ compared to the single chromophore's absorbance). In the case of H-aggregates this ratio decreases for stronger interactions. With these indications the aggregation behaviour of a sample can be traced only by steady-state measurements. Moreover, this complex model yields information about the coupling strengths, the energetic disorder and electron-phonon coupling effects. The exact execution of this model, its applications and further modifications towards charge transfer can be found in a very detailed review by Hestand et al. [65].

Two-Photon Absorption Upon Aggregation. The aggregation characteristics stated above all apply at first to 1P allowed states. Nevertheless, the core of this work is about non-resonant 2P absorption. The question is, how do these 2P allowed states behave upon aggregation of the molecules. There haven't been any publications about that topic up to now. Several research projects, as shown in the introduction, have been made on resonant¹ 2P processes on mostly molecular J-aggregates with permanent dipoles. Spano and Mukamel calculated in 1989 [77] the third order susceptibility $\chi^{(3)}$ for a resonant 2P absorption through exciton and biexciton states. All terms for biexciton states, however, are not of importance for this work. The most essential finding is, that, including off-resonance conditions in $\chi^{(3)}$, all possible terms which result in a 2P enhancement cancel out completely. In a more figurative picture: for non- or off-resonant 2P absorption the first interaction is due to virtual states with lifetimes of about 2 to 3 fs; this time is way too short for the molecules to interact properly and the molecules behave like monomer units. Moreover, the coupling of S-CBT in H-aggregates is around 800 cm^{-1} [76], which translates into 42fs and is multiple times slower than the lifetime of the intermediate virtual state. Therefore excitons in 2P allowed states are not formed on these short time scales. Thus the expected behaviour is to find no changes for only 2P allowed states at all upon aggregation.

2.5 Optical Bloch Equations

The *Bloch equations* have their origin in the field of nuclear magnetic resonance (NMR). Felix Bloch first derived these equations 1946 to describe the dynamics of the net magnetisation (*paramagnetic polarisation* in accordance with Bloch) as function of the dephasing and relaxation times after interaction with an external radio frequency field [98]. With these set of equations, each component of the magnetisation vector \mathbf{M} can be derived in time.

¹Resonance, in this case, applies to intermediate real excitonic states, which are populated in a 2P process by the absorption of the first photon followed by the second absorption to the final state.

This problem can be transferred to the field of light matter interactions and are then called *optical Bloch equations* (OBE). The OBE are a convenient method to describe effects like dephasing, relaxation and strong coupling processes with a simple set of three equations. The following steps are based on the calculations made in [55, 57] and can be looked up in detail in these publications. Starting from a single molecule with two molecular levels ($|1\rangle, |2\rangle$, with $E_2 > E_1$) exposed to monochromatic external field of energy ω_L the wave function coefficients are derived (see also section 2.2). The interesting quantity of these semi quantum mechanical problems are the $c_i c_j^* = c_{ij}$, which are the product of the wave function coefficient c_i with its own complex conjugate. For the case of a two level atom this ends up in $|c_{11}|, |c_{22}|, |c_{12}|$ and $|c_{21}|$, whereas the first two are called *populations* and the remaining *coherences*. The *density matrix elements* are identified as follows:

$$\rho_{11} = |c_{11}|^2, \quad \rho_{22} = |c_{22}|^2, \quad \rho_{12} = c_1 c_2^* \quad \text{and} \quad \rho_{21} = c_2 c_1^* = \rho_{12}^* \quad . \quad (2.27)$$

In this case the condition $\rho_{11} + \rho_{22} = 1$ for the two level system is always preserved. The interaction is again defined as $H^S = V = -\mathbf{p} \cdot \mathbf{E}_0 \cos(\omega_L t)$. In the system of the molecule the EM field vector is rotating with ω_L . The problem is therefore solved in a rotating frame system (rotation of the Hamiltonian by ω_L, \hat{H}). Under the assumption of relaxation and dephasing, the time evolution of the density matrix can be derived with the *Liouville-von-Neumann* equation [99]

$$\dot{\hat{\rho}} = \frac{i}{\hbar} [\hat{\rho}, \hat{H}] - \hat{\gamma} \circ \hat{\rho} \quad . \quad (2.28)$$

$\dot{\hat{\rho}}$ is the time derivative of density matrix operator, the first addend is the commutator of $\hat{\rho}$ with the rotated Hamiltonian and \circ denotes the element wise product between a rate matrix $\hat{\gamma}$ and $\hat{\rho}$. The OBE finally read

$$\dot{\rho}_{11} = i \frac{\Omega_R}{2} (\rho_{21} - \rho_{12}) + \gamma_{11} \rho_{11} \quad (2.29)$$

$$\dot{\rho}_{22} = i \frac{\Omega_R}{2} (\rho_{12} - \rho_{21}) - \gamma_{22} \rho_{22} \quad (2.30)$$

$$\dot{\rho}_{12} = i \frac{\Omega_R}{2} (\rho_{11} - \rho_{22}) - \rho_{12} \left(\frac{\gamma_{12}}{2} + i\delta \right) \quad (2.31)$$

$$\dot{\rho}_{21} = i \frac{\Omega_R}{2} (\rho_{22} - \rho_{11}) - \rho_{21} \left(\frac{\gamma_{21}}{2} - i\delta \right) \quad . \quad (2.32)$$

Two new quantities were introduced: the *Rabi frequency* $\hbar\Omega_R = -\hat{\boldsymbol{\mu}}_{12} \cdot \mathbf{E}_0$ and the detuning $\delta = \omega_L - \omega_0$ between the absorption of the molecule and the laser frequency.

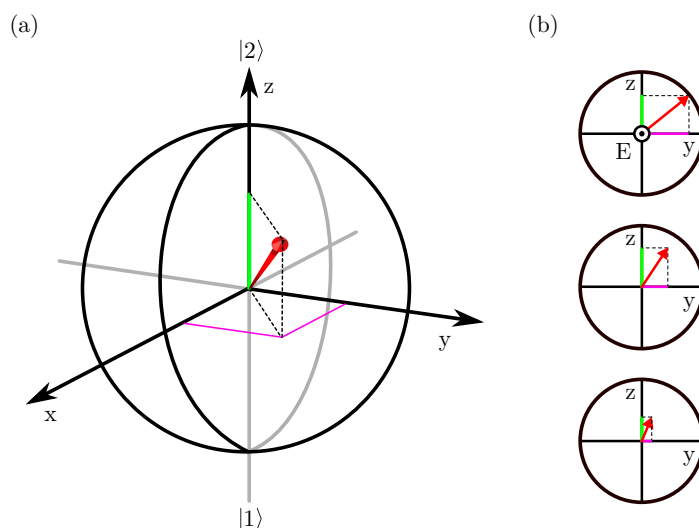


Fig. 2.9: Bloch Sphere and Vector. (a) Three dimensional Bloch sphere with Bloch vector (red). The z component (green) reflects the population difference between state 2 and 1 and the x- and y-components (magenta) yield the coherences. If the Bloch vector points straight downward (upward), all population probability is in the ground state $|1\rangle$ (excited state $|2\rangle$). (b) Projection of the Bloch vector on the y-z-plane in the case of resonance and electric field amplitude parallel to the x axis (see main text). The upper panel shows the rotated Bloch vector, indicating a population probability in state 1 and 2 (z-axis, green) and coherences (y-axis, magenta). The middle panel reflects the process of pure dephasing (loss of coherence, change in the y-value) without any population relaxation (z-value keeps constant), while, in the lowest panel both, dephasing and population relaxation took place.

These equations describe the time dependent behaviour of the populations of states $|1\rangle$ and $|2\rangle$ and the corresponding coherences. The population relaxation of the ground state $|1\rangle$ γ_{11} is 0 as the lifetime is infinitely large. For state $|2\rangle$ the lifetime is finite. However, the time scale of the experiments carried out in this work is much smaller (femtoseconds) than the excited state lifetime (picoseconds to nanoseconds for organic molecules). Therefore the assumption $\gamma_{22} \approx 0$ is justified for many organic systems. However, if any additional relaxation, e.g. a non radiative transition into lower excited states or dark states, takes place this assumption is not valid any more and γ_{22} has to be included. This will be important for the system MeLPPP, where fast relaxation processes between two electronic states decrease the excited state population. The dephasing of the coherences is described by $\gamma_{21} = \gamma_{12} = \frac{1}{T_2} = \frac{1}{2T_1} + \frac{1}{T_2^*} \approx \frac{1}{T_2^*}$ (see Eq.2.4).

In analogy to the magnetisation vector in NMR, a pseudo spin vector can be formed out of the components in the OBE with

$$x = \rho_{21} + \rho_{12}, \quad y = i(\rho_{21} - \rho_{12}) \quad \text{and} \quad z = \rho_{22} - \rho_{11} \quad . \quad (2.33)$$

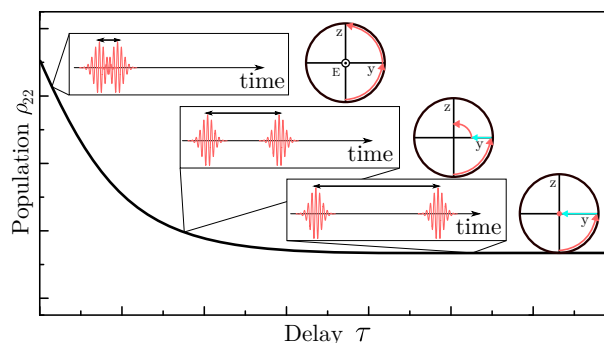


Fig. 2.10: Schematic Coherence Decay Envelope. Double pulse sequence transfers population ρ_{11} from state $|1\rangle$ into state $|2\rangle$, ρ_{22} by an EM field with amplitude parallel to the x axis. A snapshot in time is shown in the insets for three different delays τ between the phase-locked pulses and the respective projection of the Bloch vector tip on the y - z -plane. Light red arrows reflect the rotation of the tip by interaction with the pulses and turquoise arrows show the dephasing, without any population relaxation. The probability of increasing ρ_{22} vanishes with higher τ which is reflected by the decay. The characteristic time the population transfer probability decreases is called coherence time. After the coherence is fully dephased (third inset) the population can not be increased by the second pulse.

This vector is called the Bloch vector. With this figurative way, one is able to describe the interaction of a two level system with an EM field (continuous wave or pulsed). The amount of rotation angle from its equilibrium position (pointing downward, all population is in state $|1\rangle$) depends on the interaction time and strength. Furthermore the convention is to set the polarisation of the electric field amplitude vector along the x or y axis, respectively, while in this work the considerations are based on the former case. If the excitation energy is E_2 (E_1 is set to 0), that is $\delta = 0$, the rotation is always through the x - or z axis. For $|\delta| > 0$ the rotation is through an axis combination of x and z (see Fig.2.9 (b)). Next to a population transfer from state $|1\rangle$ (or the ground state) to state $|2\rangle$ (first excited state), the generation and loss of coherence can be traced by the change of x - and y -components of the Bloch vector. In a picture without any population relaxation, the coherence will be lost, because of pure dephasing (see section 2.1). While the z -component stays constant, the x - and y -values will vanish in time. Strong interaction of the molecule with the electro-magnetic field, by high electric field amplitudes or strong coupling, will result in depopulation effects by stimulated emission. This process complies with a rotation by an angle $> \pi$, which results in less population in state $|2\rangle$ than for a complete rotation by π .

Experimentally this effect can be probed by the stepwise increase of the excitation power incident on a single molecule. Several publications on this effect, called *Rabi oscillations*, have been made. Gerhardt et al. [100] prepared a coherent state in a single dibenzanthrene molecule and traced the photoluminescence (PL) particularly

in dependence of the excitation power. At a distinct value the PL starts to exhibit small oscillations modulated on top. These oscillations can be described by multiple rotations by π of the Bloch vector. Stimulated emission therefore reduces the population which is reflected by an oscillatory behaviour of the PL. Furthermore Hildner et al. [20] exploited several single terrylene diimide molecules to a double pulse excitation scheme. The first pulse transfers excitation probability into the excited state, ρ_{22} , and generates coherence between state $|1\rangle$ and $|2\rangle$. Now, if the second pulse has a defined phase with respect to the first pulse, and the generated system is not fully dephased, a second rotation of the Bloch vector is possible, which increases ρ_{22} . However, if the system is already fully dephased at arrival of the second pulse, the finally generated population can not be increased any more, leading to the signal strength, which can be produced by an incoherent excitation scheme. This effect is called coherence decay and an exemplary trace as well as snapshots of the Bloch sphere projection on the y-z-plane are given in Fig.2.10. Different shapes of the obtained decay traces indicate strong or weak interaction strengths between the transition dipole and the electro-magnetic field, resulting in different rotation angles of the Bloch vector. The pure Rabi-oscillations can be found in the Supplementary Information of [20].

The Bloch vector analysis will be important for the first part of the experiments carried out in this work. The response of single MeLPPP to a similar double pulse excitation sequence are detected and analysed in the Bloch picture. Informations about the specific dephasing times, couplings and the time dependent coherences are obtained.

2.6 Quantum Dynamics Identification

In order to reconstruct the multi-photon induced single molecule signals, a powerful theoretical method is essential. The basic idea is shown in the following section. Detailed information can be found in reference [101].

The Quantum Dynamics Identification (QDI) procedure was developed by Prof. Dr. Chuan-Cun Shu of the University of New South Wales, Australia and School of Physics and Electronics, Hunan Key Laboratory of Super-Microstructure and Ultrafast Process, Central South University, Changsha [101]. The procedure is based on the density matrix formalism and its task is to find a minimal quantum mechanical model, which reproduces the noisy data with high fidelity.

The description of the density matrix $\rho(t)$ (see section 2.5) of a single molecule in the N -dimensional Hilbert space is given by the Lindblad master equation [102], which is a more specialised formulation of Eq. 2.28

$$\frac{d}{dt}\rho(t) = \frac{-i}{\hbar} [\hat{H}_0 - \hat{H}^S(t), \rho(t)] + \sum_{i \neq j=0}^{N-1} \mathcal{L}_{ij}(\rho(t)) + \sum_{i=0}^{N-1} \mathcal{D}_i(\rho(t)) \quad . \quad (2.34)$$

$\hat{H}_0 = \sum_{j=0}^{N-1} E_j |j\rangle \langle j|$ is the stationary unperturbed molecular Hamiltonian and $\hat{H}^S(t)$ describes the interaction between the molecule and the EM laser field. Quantum mechanical loss channels for population and coherence are described by the last two terms in Eq.2.34, respectively, and are included in the rate matrix γ in Eq.2.28. $\mathcal{L}_{ij} = \Gamma_{ij} \left(\rho_{ii} |j\rangle \langle j| - \frac{1}{2} \{ |i\rangle \langle i|, \rho \} \right)$ is called a Lindblad super operator and represents the population relaxation from state $|i\rangle$ to state $|j\rangle$. From this term the relaxation rates Γ_{ij} between the involved states are obtained. Furthermore, dephasing plays a key role for coherence decay and coherent control experiments. The pure dephasing of state S_i is given by $\mathcal{D}_i = \frac{\gamma_i}{2} \left(\rho_{ii} |i\rangle \langle i| - \frac{1}{2} \{ |i\rangle \langle i|, \rho \} \right)$, and the dephasing rate $\gamma_i = \frac{1}{T_i}$ is the inverse of the dephasing time [103]. The time evolution of the density matrix is calculated according to Eq.2.34 under consideration of interaction between the pulsed excitation $E(t)$ and transition dipole moment $\mu_{ij}^{(1P),(2P)}$ for 1P and 2P processes. *Fourier* transformation of the experimental measured spectral amplitude $A(\omega)$ yields the time dependent electro-magnetic field amplitude. Furthermore the applied phase $e^{i\varphi(\omega)}$ and amplitude functions $A_{\text{mod}}(\omega)$, dependent on the experiment carried out, can be included by multiplication

$$E(t) = \frac{1}{\sqrt{2\pi}} \int_{-\infty}^{\infty} A(\omega) A_{\text{mod}}(\omega) e^{-i\omega t} e^{i\varphi(\omega)} d\omega \quad . \quad (2.35)$$

With reasonable initial parameters for (i) the dephasing and relaxation rates, (ii) Rabi-couplings $\Omega^{(1P)} = (\mu_{ij}^{(1P)}) E_0$ and $\Omega^{(2P)} = (\mu_{ij}^{(2P)})^2 E_0^2$ between the transition dipole and the peak strength of the electro-magnetic laser field E_0 (iii) and the energy of the involved states E_i , the Lindblad master equation is solved for each applied modulation Π_M . A residual S for this multi parameter optimisation problem is defined as

$$S = \sum_{m=1}^M \left| \lambda_m(Q, \Pi_m) - \sum_n^N \mathcal{X}_{m,n}(Q, \Pi_m) \Delta Q_n \right|^2 \quad , \quad (2.36)$$

and is updated iteratively by ΔQ from the initial guess. The experimental PL signal $\mathcal{P}(Q, \Pi) = [\mathcal{P}(\Pi_1), \dots, \mathcal{P}_M(\Pi_M)]$ is compared to the theoretically calculated PL data $P(Q, \Pi_m) = [P_1(Q, \Pi_1), \dots, P_M(Q, \Pi_m)]$ via the variance matrix elements $\lambda_m(Q, \Pi_m) = (P)_m(\Pi_m) - [aP_m(Q, \Pi_m) + b]$ and Jacobian matrix elements $\mathcal{X}_{m,n}$. The dependencies

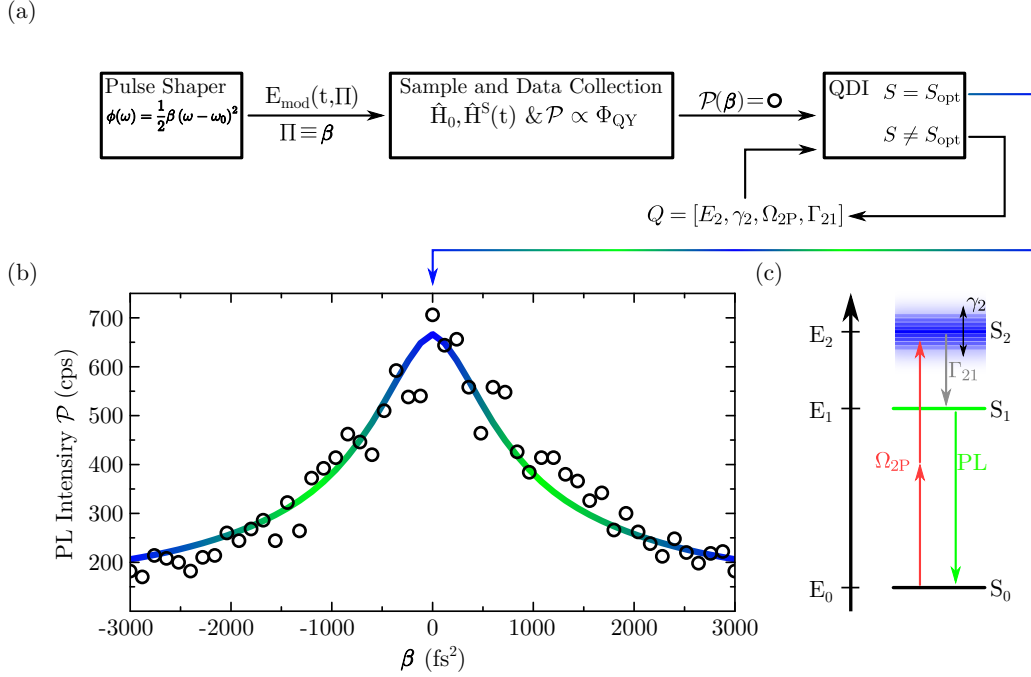


Fig. 2.11: Scheme for Identifying the Single Molecule Quantum Dynamics from a Phase Shaping Experiment. (a) Phase shaping experiment controls the linear chirp of the excitation by parameter β . Interaction ($\hat{H}^S(t)$) of the shaped EM field $E_{mod}(t, \Pi)$ with the molecule (\hat{H}_0) generates the PL which is proportional to the molecules quantum efficiency Φ_{QY} . This set of data is iteratively reproduced with a termination condition $S = S_{opt}$ by the Quantum Dynamics Identification (QDI). For this kind of experiment, the parameters to optimise are: the energy level E_2 of the analysed molecule, the dephasing rate γ_2 and relaxation Γ_{21} of the 2P allowed state S_2 and the 2P Rabi coupling Ω_{2P} . (b) and (c) Optimum QDI results (blue-green solid line) plotted together with the experimental data \mathcal{P} (empty circles) in dependency of the applied chirp factor β and the associated energy level diagram of all involved levels (ground S_0 , first S_1 and second excited state S_2) and processes (for the description of parameters see (a)).

define the parameters to optimize $Q = [Q_1, \dots, Q_N]^T$ and the modulation Π_M . The theoretical PL data points are scaled with a and b , because the detected experimental PL signal is proportional to the absolute quantum yield of the electronic state and therefore its population. Least square fitting methods yield the optimal values for a and b . It is important to note, that due to the lower signal to noise ratio, which is common for single molecule experiments, the minimum found is not necessarily the global but a local minimum (see appendix A.2 for more information).

To understand the quite complicated model above, an exemplary measurement is given in Fig.2.11. The principle: 2P induced single MeLPPP chromophore PL is modulated by a phase-only approach. MeLPPP exhibits strong 2P absorption cross section of the second excited state (see Fig.2.11 (c)). From S_2 the generated population decays to the first excited state S_1 , from where PL emission can be detected. The

function applied to the spectral dependent phase of the electro-magnetic excitation pulse reads

$$\varphi(\omega) = \frac{1}{2}\beta (\omega - \omega_0)^2 \quad , \quad (2.37)$$

where β is the linear chirp parameter and ω_0 is the maximum of the spectral amplitude of the excitation. With β set to different values between $[-3000, 3000]$ fs² the probability of inducing a 2P transition from the ground state S_0 to the 2P allowed state S_2 is changed. This is reflected by a higher or lower PL signal at the detector. The obtained data is fed to the QDI procedure and iteratively reproduced by optimizing $Q = [\Omega_{2P}, \gamma_2, \Gamma_{21}, E_2]$. If the residual, defined in Eq.2.36, hits a local minimum, an optimum of the QDI is found. In this case the data is reproduced with high quality as shown in Fig.2.11 (b). (c) reflects schematic the underlying identified processes of the PL detected pure 2P absorption experiment, which is minimal necessary to find an optimal model. After transferring excitation probability from S_0 to S_2 by 2P absorption, the coherence dephases with γ_2 and the population can relax to S_1 with a rate of Γ_{21} . From S_1 the population decays back to S_0 under radiation of PL. This special case reflects the pure 2P absorption process between two states of a single chromophore. Models which go beyond this “simple” case will be discussed in chapter 4. With the combination of exploitation of single molecules to coherent control schemes and a theoretical identification procedure, the fast and reliable analysis of fundamental (and hidden) processes, which lie at the heart of many modern organic electronics, becomes possible.

Chapter 3

Experimental

This chapter will cover the sample characterisation with regard to their photophysical properties, in the linear and non-linear regime. Furthermore, information on the sample preparation will be provided. The preparation method plays a key role in order to produce single molecule concentration for the MeLPPP CP and the desired aggregation properties of the S-CBT ensemble solution. The last part is about experimental details such as the setup, the pulse shapers and the characteristics of the transform limited and shaped pulse.

3.1 Sample

Methyl Substituted Ladder-Type Poly(*para*-Phenylene)

The CP methyl substituted ladder-type poly(*para*-phenylene), short MeLPPP, which was synthesized by Prof. Dr. Ullrich Scherf (Universität Wuppertal, Germany) [58, 104] has a molecular weight of $M_n = 55300$ Da with a polydispersity of 3. The chemical structure is shown in Fig.3.1 (a), with its attached functional side groups, which provides solubility in organic solvents. The central phenyl ring is connected to its neighbouring rings by two bonds, the carbon-carbon bond and a carbon-methyl-carbon bond, yielding the name “ladder-type” polymer (see Fig.3.1 (a) orange arrows). This two-fold bonding between the phenyl rings lead to a reinforcement of the polymer backbone, resulting in high intra-chain order. This order can be broken by defects, due to impurities and/or kinks in the chain itself. Again, these subunits divided by defects are called chromophores (see section 2.1 and Fig. 2.1), consisting in the case of MeLPPP of around 5 - 10 monomer units [46, 47, 50]. With around 70 - 80 repetition units per MeLPPP chains, one single chain contains about 10 chromophores. Furthermore, the high intra-chain order strengthens the symmetry properties of the polymer backbone, giving rise to high 2P absorption cross sections of these ladder-type structures [38, 105], see section 2.3.

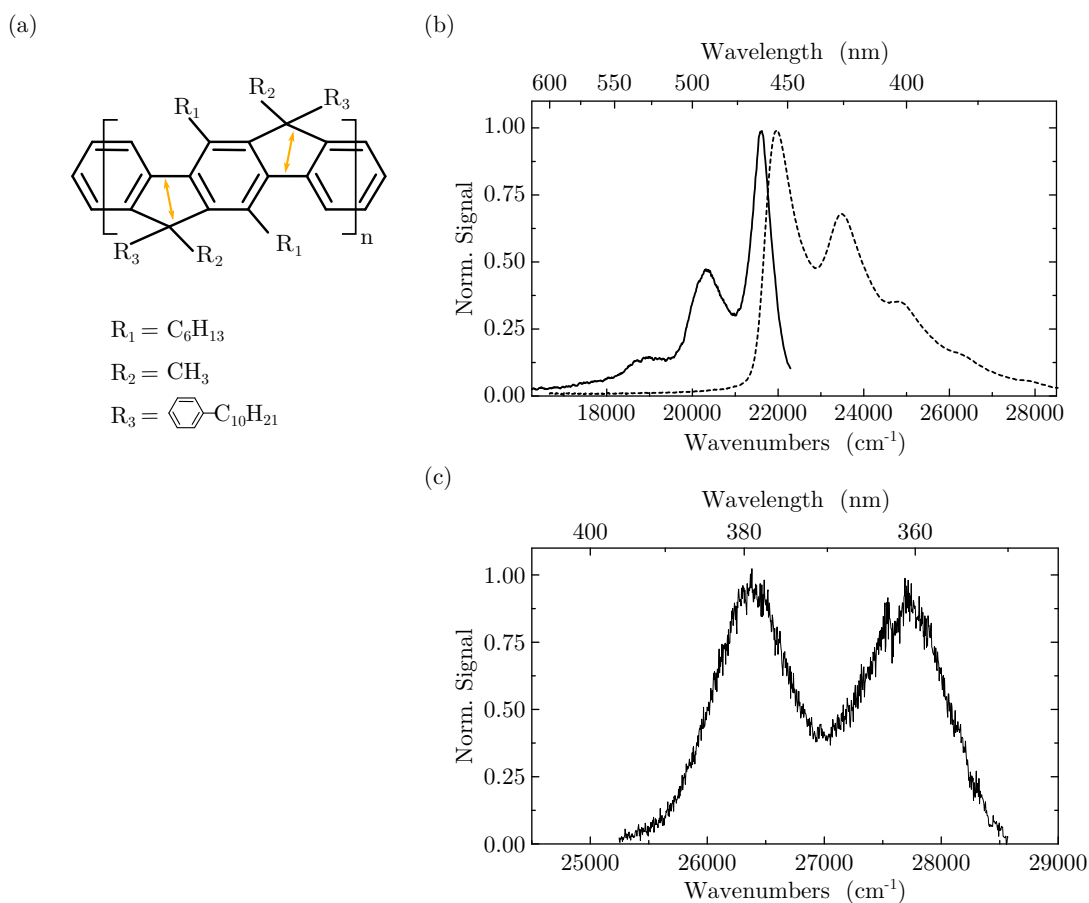


Fig. 3.1: Spectral Characteristics of MeLPPP. (a) Chemical Structure of methyl-substituted ladder-type poly(*para*-phenylene) (MeLPPP). The orange arrows mark the two bonds giving MeLPPP the name ladder-type. (b) Linear absorption (dashed) and emission spectrum (solid) of a thin MeLPPP film measured at room temperature. (c) Two-photon (2P) fluorescence excitation spectrum of a thin MeLPPP film at room temperature, measured with a continuous wave laser [93].

In Fig.3.1 (b) the room temperature (RT) spectral characteristics for a thin MeLPPP-film is shown for 1P absorption (data taken with permission from [93]). The maximum of absorption is around 22000 cm^{-1} , followed by a pronounced vibronic progression spaced by 1400 cm^{-1} to 1500 cm^{-1} . These modes can be ascribed to intra-molecular carbon-carbon stretching modes and their overtones and combined vibrations [106]. The inhomogeneous line width at RT yields 690 cm^{-1} . The PL is red shifted to the absorption energy, but however, the Stokes shift is only small, as the rigid backbone does not allow a strong shift between the ground states and the first excited states potential energy minima. The maximum of PL is centered around 21600 cm^{-1} and the strong electron-phonon coupling to the C-C stretching mode is evident, too. Due to the overlap of absorption and emission the line width of the maximum of PL is a

little bit smaller due to intra *density-of-states* energy transfer [13], but of same order of magnitude (600 cm^{-1}).

Fig.3.1 (c) shows a fluorescence excitation spectrum of the, only 2P allowed, second excited state S_2 of MeLPPP (data taken with permission from reference [93]). Surprisingly, this spectrum was taken using a continuous wave excitation laser [93], reflecting the high 2P absorption efficiency of MeLPPP. Rather low excitation intensities of $2 \frac{\text{MW}}{\text{cm}^2}$ were enough to induce the 2P absorption process. The pure electronic transition of S_2 is located around 26380 cm^{-1} , which is about 4400 cm^{-1} above the first excited (only 1P allowed) state. The second peak at 26670 cm^{-1} in Fig.3.1 is ascribed to an intra-molecular carbon-carbon (intra as well as inter ring) stretching mode of energy $\approx 1290 \text{ cm}^{-1}$ [93]. Furthermore, below 26380 cm^{-1} no 2P induced PL signal was found. This indicates the strongly maintained symmetry relations of the backbone of MeLPPP. This, in turn, means, that the impact of the bulky side chains is insignificant on the backbone structure.

Overall, MeLPPP is a perfect model system to study 2P absorption processes. Its high symmetry relations give rise to efficient 2P transitions and in combination with the RT quantum yield of about 25 % in film (60% in solution), experiments on the single molecule level could be realised [107, 108]. Furthermore, the high photostability of MeLPPP is a favourable property, as the chromophores will be exposed in this work to averaged powers of about $0.2 \cdot 10^6 \frac{\text{W}}{\text{cm}^2}$ (peak power of the pulsed excitation was about $6 \cdot 10^{10} \frac{\text{W}}{\text{cm}^2}$) for several of seconds.

Carbonyl-Bridged Triarylamine Derivative

The other part of the measurements were carried out on a carbonyl-bridged triarylamine (CBT) derivative with s-chiral side chains, short S-CBT. The compound was synthesized by Dr. Andreas Haedler [28] (Makromolekulare Chemie I, Universität Bayreuth). The chemical structure of the monomer is shown in Fig.3.2 (a). The planar, aromatic, heterotriangulene core (grey) is functionalised by three hydrogen-bonding amide groups (green) at the positions 2, 6 and 10. Furthermore, bulky Gallic acid groups (blue) are attached to that amide linkers in order to influence the solubility and achieve steric repulsion (see later). The self-assembly from single molecules to single nano fibres is driven by *van-der-Waals* interaction of the π -electron systems of the aromatic CBT core. Without the functionalised amide groups the adjacent CBT cores would stack upon each other with a significant spatial offset, downgrading the quality of aggregation and energy transfer mechanism [94]. The hydrogen-bonding amide groups, however, eliminate this offset and stabilise the desired columnar structure. S-CBT is a model system to study energy transfer along a single nano fibre upon

laser excitation. The side chains attached to the amide groups show by themselves already strong chirality and define the rotation direction along the complete fibre. A fibre like structure is sketched in Fig.3.2 (c), once without rotation of the monomers for convenience and once from a side view to clarify the helical structure. Small-angle X-ray scattering measurements have shown, that the distance between the monomer S-CBT units in single fibre is about 3.3 Å, which is indeed the π - π stacking distance [28]. Energy transfer over a long distance up to 4 μm has been reported for another CBT derivative [94]. The only difference between the S-CBT, shown here, and the compound in [94] are the side groups attached to the amides.

The self-assembly of S-CBT can be tuned with the choice of solvent. In tetrahydrofuran (THF) the compound is fully solubilised and the absorption and emission spectra obtained are referred as the monomer spectra. The absorption spectrum is shown in Fig.3.2 (b) with a zoomed part of the absorption and additional PL in the inset. The spectra were normalized to the 0-1 peak of the first excited singlet state S_1 (marked with the particular arrow). The 0-0 peak of the absorption is located at 21620 cm^{-1} and has a full width at half maximum (FWHM) of about 1300 cm^{-1} . The spectra can be described by a vibronic energy of 1370 cm^{-1} , the FWHM for the progression of vibronic peaks is around 1500 cm^{-1} . Strong absorption signals are obtained from 29500 cm^{-1} up to 37000 cm^{-1} . This absorption can be ascribed to a (1P allowed) higher excited singlet state S_n ($n \geq 2$ as clear denotation of these high lying states is not unambiguous). However, although there is no prior knowledge about strictly 2P allowed states, the symmetry consideration made in section 2.3 demonstrate the possibility to induce a 2P transition into S_1 . This will be further investigated in chapter 5. In dodecane (DOD) the compounds self-assemble in a H-aggregate behaviour. This H-type assembly is described by a strong suppression of the 0-0 peak in absorption and a small blue shift of the respective energies (see section 2.4). The whole absorption is shown in Fig.3.2 (d), with a zoomed part of the absorption and additional PL in the inset. The spectra were normalised as before. Although the 0-0 transition has clearly decreased, the absorption is red and not blue shifted. This seems to be in contrast with theoretical results, but the interpretation of steady state spectra is still not that trivial. In aggregate structures the individual building blocks interact with different aggregate molecules as well as solvent molecules. For the fully dissolved case, the monomers only interact with the solvent molecules. However, the local environment is different for the aggregate, where adjacent S-CBT units present the nearest environment. This *gas-to-crystal* red shift, due to different polarisabilities of the surroundings, can easily exceed the exciton blue shift [96]. For a more reliable description of the H- or J-type aggregate quality the interpretation should stick to the ratio between the 0-0 and 0-1 transition of S_1 in absorption [96].

Next to the S_1 absorption, the radiative 0-0 transition from S_1 , shown in the inset in Fig.3.2 (d), is suppressed, too, which is additionally forbidden by symmetry reasons. The absorption above 29000 cm^{-1} , which is ascribed to high lying electronic states S_n ($n \geq 2$), is still strong, but the shape has significantly changed. However, it is still unclear from which specific states this absorption originates.

3.2 Sample Preparation

The single molecule 2P absorption measurements were carried out on the MeLPPP system. The solid MeLPPP was dissolved in toluene (99.7% purity, Sigma-Aldrich) at a concentration of 10^{-9} M to produce evenly spaced single molecule samples and only individual compounds are excited. The solution used for preparing the final sample contained $5\frac{\text{mg}}{\text{mL}}$ polystyrene (polydispersity index 1.04, PSS). Thin films of several 100 nm were produced by spincoating on a freshly cleaned quartz cover slip of thickness $170\mu\text{m}$. The spincoater settings can be found in the appendix A.2. The cover slip then was put into a holder construction into the excitation/detection unit (see below). Constant nitrogen flow prevents oxygen to diffuse into the polystyrene film and minimises photobleaching effects.

The S-CBT molecule was dissolved in THF at a concentration of about $40\ \mu\text{M}$, which is 100 parts per million (ppm), to produce a fully solubilised system. On the other side, n-dodecane was chosen, because the S-CBT molecule forms single H-aggregated nano-fibres in this solvent. The final dispersion was obtained by putting the sample into the ultrasonic bath and subsequent heating near below the boiling point of the respective solvent. The freshly made dispersion was then put into a quartz glass cuvette (QS-111, Hellma Analytics) with a light path length of 10 mm, and finally transferred to the modified setup. All measurements were carried out within 24 hours.

3.3 Technical Informations

Setup

In order to perform ultrafast measurements and coherent control experiments on single MeLPPP, a setup was built consisting of an ultrafast laser, pulse shaper and an excitation/detection unit consisting of two objectives and a CCD as well as a time-resolved detector. The concept is pictured in Fig.3.3. The laser system is a titan-ions doped sapphire crystal system (GriffinTM-10-WT, KMLabs), able to produce 30 fs pulses

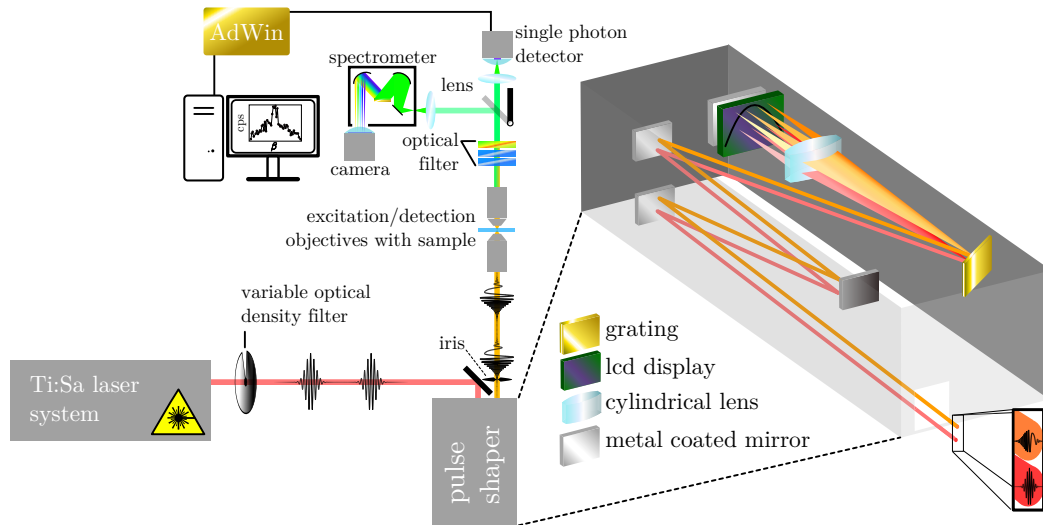


Fig. 3.3: Experimental Setup. The titan-sapphire (Ti:Sa) laser produces pulses with a full width at half maximum of about 30 fs (transform limited, oscillatory line in red path) at a repetition rate of 80 MHz. Two reflective optical density wheels attenuate the power (only one drawn). In the pulse shaper the electro-magnetic field is spectrally dispersed by the gold coated grating and focused by a tube lens onto the anti reflex coated liquid crystal display (LCD), called the spatial light modulator (SLM), operating in the first order of diffraction (solid black line reflects an applied phase function). Another metal mirror reflects the modulated light a second time through the SLM and the modulated excitation is spatially combined again by the grating. The desired output (oscillatory line in orange path) is separated from the 0th order of diffraction by the iris and passes through the excitation air objective (NA=0.5) and is focused in the sample plane. The photoluminescence (PL) is detected by a second air objective (NA=0.85). The excitation light is blocked by two blue glass 39 filter (thickness of 3 mm) and a dielectric short pass with cutting edge at 492 nm (20325 cm^{-1}). The passed PL can be detected by either a single photon counting module, or through reflection at a flipped mirror, by a spectrometer and subsequent charged coupled device camera. The single photon module detected PL is then counted by a real time controller (AdWin ©Jäger GmbH) and passed to a self coded python software on the computer. To make the picture easier to follow, the entrance and exit beam path were drawn next to each other. The three dimensional sketch reflects the real situation with one beam above the other.

at a repetition rate of 80 MHz by mode locking. The tuning range of the laser is between 700 - 920 nm and the output power in the mode locked operation is around 500 mW. To attenuate the power two reflective optical density (OD) wheels were used (Thorlabs). The pulse shaping unit (folded 4f arrangement, MIIPS®-HD, BioPhotonic Solutions) is drawn in the right part of Fig.3.3. A gold coated grating spectrally disperses the EM field of bandwidth $\Delta\nu$ and a subsequent tube lens focuses each energy into the masking plane. The spatial light modulator (SLM), a liquid crystal display (LCD)(2D 8000×600 pixel, LCOS-SLM X11840-07(X), Hamamatsu), is mounted in the masking plane and the desired amplitude and phase modulation patterns are produced by a commercial software (MIIPS 2.0) on an external laptop. Another metal coated mirror reflects the

beam a second time through the SLM and the modulated EM field is again combined at the grating and exits the pulse shaper unit slightly above the entrance height. Due to the anti reflection coatings of the SLM and its voltage specifications the optimal transmission is between 13333 cm^{-1} and 11765 cm^{-1} (750 and 850 nm). The shaping is diffraction-based, which enhances the contrast in amplitude shaping schemes and suppresses unwanted modulator replicas [109]. The desired output is diffracted into the first order and after the shaping unit a spatial filter (iris) is put into the path to block all except the first order. An air objective (Micro Plan, magnification 20, numerical aperture NA=0.5, Microthek) focuses the light into the sample plane. A second air objective (S.Plan, magnification 60, NA = 0.85, Euromex) is used to collect the PL, which is then separated from the excitation light by three optical filters: two blue glass 39 (Schott) of thickness 3 mm and one dielectric short pass with cutting edge at 492 nm to fully suppress the high power excitation. The PL is detected by a single photon counting module (avalanche photo diode, APD, Multi Photon Devices, chip diameter $50\text{ }\mu\text{m}$, dark counts < 25 counts per second, counting output TTL 250 ps) and the signal is sent through a real time micro controller ((AdWin©, Jäger GmbH) to the computer to further analyse the data by a self written python software. The AdWin was programmed to count the pulses which are produced by the APD with a time binning of about 36 ms. The time resolution was chosen to be small enough to detect important features, but still the low light conditions of single molecule spectroscopy require sufficient integration times. A flip mirror opens the possibility to detect spectral features. However, for low signal strengths measured in this work, the spectral path was not chosen at all. Besides the dielectric mirror inside the pulse shaping unit all used mirrors are silver coated (reflectivity > 0.96 at 400-2000 nm, Thorlabs).

Pulse Compression. Even though the setup consists mainly of non dispersive elements, the transmission through the whole path, up to the sample plane will affect the spectral dependent phase of the pulse ϕ_P . In order to get full control over the time dependent energy distribution and therefore also the time dependent EM field amplitude the knowledge of the spectral dependent phase distribution at the focal plane is absolutely essential. ϕ_P can be measured with the *Multiphoton Intrapulse Interference Pulse Scan* (MIIPS) technique, introduced by Lozovoy and Xu et al. [110, 111]. The *Microscope Detection Unit* (MDU) contains a nonlinear crystal for second harmonic generation (SHG) and a fibre coupler to detect the SHG radiation. The MDU is positioned in the focal plane (sample plane, instead of the sample) and the preceding optics are unchanged. The objective focuses the excitation into the crystal and, for fitting adjustments, SHG is detected by a connected spectrometer (USB4000, Ocean Optics) and the MIIPS 2.0 software (100 ms binning time). With sufficient SHG signal

MIIPS is started and operates in the following manner: different phase functions are applied in six iterations by the pulse shaper to the excitation and the spectral, as well as phase function dependent SHG signal is detected. After each iteration step a *compensation mask* is obtained, which eliminates the measured phase distortions and maximises the SHG signal. After the sixth iteration the residue of ϕ_P is close to zero and the final compensation mask (CM) is the sum of all iteratively determined masks. Measuring the pulse width $\Delta\tau$ with the final compensation applied, yields a transform limited (TL, sometimes also bandwidth limited) pulse, which can be described by the time-bandwidth product

$$\Delta\nu\Delta\tau = \frac{2\ln 2}{\pi} \approx 0.441 \quad , \quad (3.1)$$

whereas this value is only valid for a Gaussian intensity distribution of the pulse [112]. This product is also measured by the software and serves for a quality check of the compressed pulse. For the experiments, the CM is added to all phase modulations to guarantee the correct pulse shape in the focal plane. To characterise the compressed pulse, the SHG spectrum can be measured in dependency of an applied cosine function. In Fig. 3.4 (a) such a color coded scan is plotted for a representative spectrum shown in the inset in Fig.3.4(b). The applied phase function reads

$$\varphi_{\text{mod}} = A \cdot \cos(\gamma(\omega - \omega_{\text{mod}}) + \delta) \quad , \quad (3.2)$$

with the spectral energy ω , the center modulation frequency ω_{mod} and the scan parameter δ (varied from -2000 rad to 2000 rad). The amplitude A was set to 2 and the period γ should be of order of the pulse width (from experience 35 fs worked for most cases). The scan shows the spectral intensity of the SHG for the variation of δ . If the pulse width is close to the transform limit, the features in the MIIPS trace with maximal SHG intensity become parallel to each other. For a still distorted phase, these features exhibit a significant deviation from the parallelism. Next to the compensation and measurement of ϕ_P the pulse width can be analysed via collinear intensity autocorrelation. An autocorrelation scan is shown in Fig.3.4(b) with an optimised Gaussian pulse shape of FWHM = 40 fs. However the autocorrelation profile does not reflect the exact pulse profile and the obtained FWHM must be divided by $\sqrt{2}$ to get the real pulse width (assuming the pulse is Gaussian). This finally yields a pulse width of 29 fs for the spectrum shown in the inset in 3.4(b) and a time-bandwidth product of ≈ 0.44 . For all measurements on MeLPPP shown in this work, the spectrum was set to resemble that spectrum shown in Fig.3.4(b) and the phase was compensated according to the procedure described above. Deviations between different measurement days can still occur, but this will result only in negligible changes in the spectrum

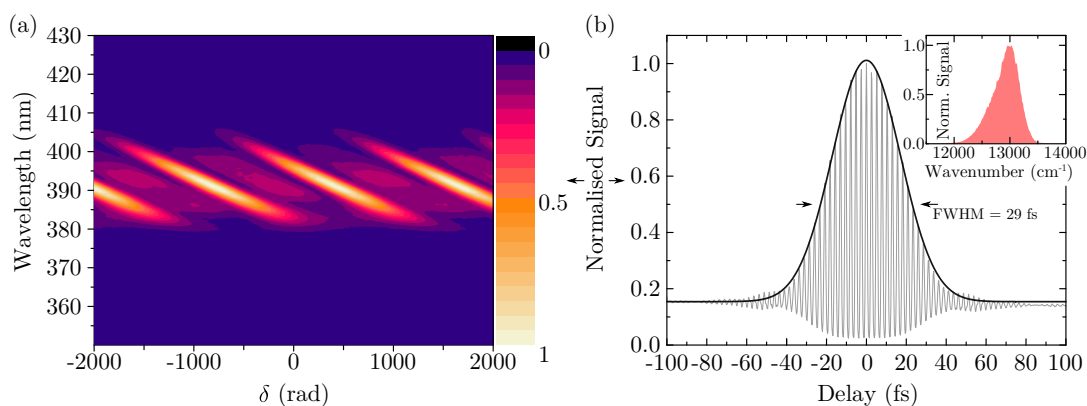


Fig. 3.4: Pulse Characterisation. (a) Phase scan with modulation phase $\varphi_{\text{mod}} = A \cdot \cos(\gamma(\omega - \omega_0) + \delta)$ of the compressed pulse in the focal plane. A was set to 2 and γ was 35 fs. δ was scanned from -2000 rad to 2000 rad. ω and ω_0 are the excitation energy and the modulation centre set to maximum of excitation, respectively. (b) Normalised SHG detected collinear intensity autocorrelation of the excitation to characterise the time dependent pulse shape (grey). Optimised Gaussian pulse (black) to obtain the pulse width of 29 fs. Note that, a collinear intensity autocorrelation of a Gaussian pulse is broadened with respect to the real shape of the pulse by $\sqrt{2}$. Therefore, the full width at half maximum (FWHM) given in the pictures, reflect the real FWHM. The inset shows an exemplary spectrum of the titan-sapphire laser with maximum energy at 12970 cm^{-1} and spectral width of 500 cm^{-1} .

and pulse shape. Further information on the spectral characteristics and pulse shaper settings will be provided in the respective measurements section in Chapter 4.

Setup Modifications for S-CBT Measurements

The S-CBT molecule presents a very complex system regarding its aggregation behaviours. The ultrafast dynamics should be therefore first of all analysed in the simpler form of a dissolved system. In doing so the excitation/detection unit had to be

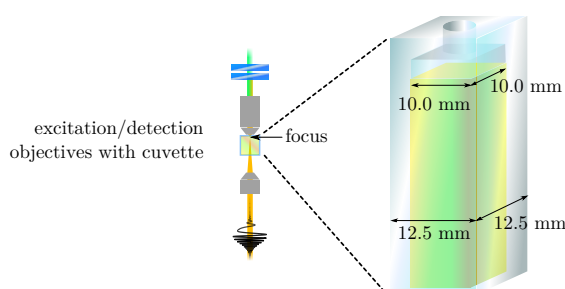


Fig. 3.5: Modified Excitation/Detection Unit. Left part: The excitation objective with $\text{NA}=0.17$ focuses the beam at the very end of the inner volume of the quartz glass cuvette. The photoluminescence is collected by an air objective ($\text{NA}=0.5$) and passed through two BG 39 glass filters. Right part: three dimensional sketch of the quartz glass cuvette with filled volume (yellow,green,orange)

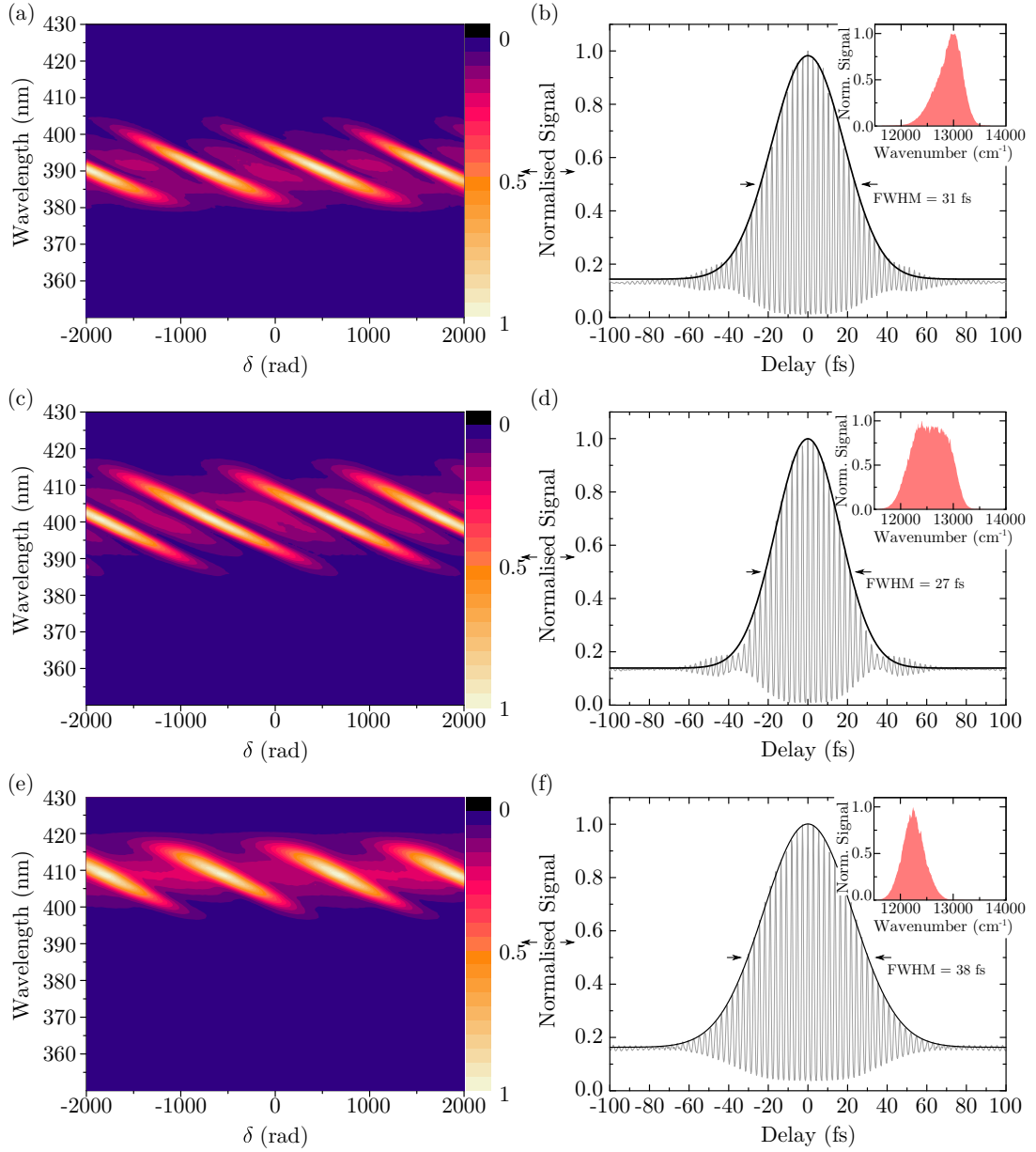


Fig. 3.6: Pulse Characterisation for the Modified Setup. (a,c,e) Second harmonic generation (SHG) detected phase scans with modulation phase $\varphi_{\text{mod}} = A \cdot \cos(\gamma(\omega - \omega_0) + \delta)$ of the compressed pulse in the focal plane for excitation shown in the respective insets in (b,d,f). A was set to 2 and γ was 35 fs. δ was scanned from -2000 rad to 2000 rad. ω and ω_0 are the excitation energy and the modulation centre set to maximum of excitation. (b,d,f) Normalised SHG detected collinear intensity autocorrelation of each excitation to characterise the time dependent pulse shape (grey). Optimised Gaussian pulse (black) to obtain the pulse width of 31, 27, and 38 fs. Note that, a collinear intensity autocorrelation of a Gaussian pulse is broadened with respect to the real shape of the pulse by $\sqrt{2}$. Therefore, the full width at half maximum (FWHM) given in the pictures, reflect the real FWHM. The insets reflect the exemplary spectra of the titan-sapphire laser with maximum energies at 12970, 12500 and 12224 cm⁻¹ and spectral widths of 500, 920 and 480 cm⁻¹, respectively.

modified with respect to the space between both objectives, which was adjusted for a quartz glass cuvette (dimensions: 46 mm × 12.5 mm × 12.5 mm) to fit in. Furthermore, the working distance of the NA = 0.85 air objective is too small to collect the PL through the 2.5 mm thick cuvette walls. Therefore the objective line up was changed, too. For the excitation an air objective of NA = 0.17 (magnification 5, PZO) with a working distance large enough to focus inside the solution, at the end of the 10 mm long light path inside the cuvette, was used (see Fig.3.5). The PL was then collected by an objective with NA=0.5 and separated from the excitation by two BG 39 glass filters. The modified part is shown in Fig.3.5 with a three dimensional sketch of the cuvette with solution in the right part. In order to compensate the phase distortion, it was necessary to determine the CM for (i) the modified setup itself, (ii) an empty cuvette of the same material and (iii) the light path dependent solvents dispersion. The final CM is then a sum of all three and was again added in each measurement to guarantee a TL pulse in the focal plane. The excitation spectrum was set to three different positions with their maxima at 12970, 12500 and 12224 cm⁻¹, to induce 2P processes, near the first 0-1 transition in S₁ up to far off resonant with this transition (see red lines in Fig.3.2 (b) and (d)). The SHG detected phase scans as well as collinear intensity autocorrelation traces, which characterise the TL pulses are shown in Fig.3.6 for each excitation spectrum investigated. The envelope of the intensity autocorrelation was again fitted with a Gaussian function, which yields FWHM of the respective spectra of 31 fs, 27 fs and 38 fs.

3.4 Modulation Patterns

In order to analyse ultrafast dynamics of single MeLPPP and S-CBT in different supramolecular arrangements, the samples were exploited to phase and amplitude shaping schemes. Phase only approaches varied the second order phase distortion, in other words the linear chirp, whereas amplitude and simultaneous phase shaping was used, to generate a phase locked double pulse sequence with flexible delay τ . The linear chirp modulation function reads

$$\varphi_{\text{mod}} = \frac{1}{2}\beta(\omega - \omega_{\text{mod}})^2 \quad , \quad (3.3)$$

whereas ω is the frequency spread along the horizontal axis of the SLM, ω_{mod} the center modulation frequency, set for all measurement to the maximum of the excitation spectrum and β is the chirp parameter scanned always from -3000 fs² to 3000 fs² in 51 steps. The averaged excitation power was kept constant over all values of β .

The pulse sequence consisting of two pulse replica with a fixed relative phase difference and variable delay τ was introduced by

$$T_{\text{mod}} = \left| \cos \left(\frac{1}{2} [(\omega - \omega_{\text{mod}})\tau + \Phi] \right) \right| \quad (3.4)$$

$$\varphi_{\text{lock}} = \frac{\pi}{2} \text{sgn} \left[\cos \left(\frac{1}{2} [(\omega - \omega_{\text{mod}})\tau + \Phi] \right) \right] . \quad (3.5)$$

The T_{mod} modulates the spectral amplitude of the excitation periodically with $\frac{1}{\tau}$ and the relative phase between the pulse replica is locked to 0 by φ_{lock} , where sgn denotes the signum function. For all double pulse sequences produced the additional phase invariable Φ was set to 0 and τ was varied from 0 to 300 fs. Again, note that the CM described above were added to all phase masks. As the amplitude modulation affects the overall power of the excitation an additional amplitude mask of $T_{\text{mod}} = C$ with $C \in [0, 1]$ was added to compensate that modulation and to ensure a constant averaged excitation power through all values of τ .

Additionally to the phase only approach above, a double pulse excitation scheme was generated by a linear phase function (for one half of the laser spectrum). This in turn produces two pulses with different carrier frequency. The function reads

$$\varphi_{\text{mod}} = \begin{cases} 0 & \omega \leq \omega_0 \\ \tau(\omega - \omega_0) & \omega > \omega_0 \end{cases} , \quad (3.6)$$

where τ is the delay between the unchanged low energy wing pulse and the delayed high energy wing pulse, and can be varied from negative to positive values.

Chapter 4

Ultrafast Measurements and Coherent Control of Single Molecules

Coherent control of single quantum systems, in particular single organic molecules, embedded in a complex environment at room temperature involves many difficulties, such as extremely short dephasing times, complex sample-host interactions due to the highly dynamic surrounding and the requirement of chemical photostability. However, it's worth the effort to overcome these problems, because the information gained by these experiments is highly fundamental to understand photoinduced chemical and biological processes on a truly molecular level. In the following an amplitude and phase shaping approach is used to generate ultrafast double pulse excitation schemes. With this pulse sequence one is able to measure the coherence decay of single MeLPPP embedded in a solid polystyrene matrix. Note that these coherence decays can be identified with the envelope of the ultrafast optical free induction decay (oFID), taking into account that the time average is equivalent to the ensemble average (ergodic principle [20]). Based on the information obtained by this experiment, phase-only shaping approaches will yield more information, in particular, about the Rabi-coupling. Furthermore, the coherent control of processes beyond the pure two-photon absorption will be presented and extend in a fundamental manner the quantum mechanical picture of the sample. In combination, this chapter will proof the strength and flexibility of our experimental and theoretical joint approach. This chapter is based on two publications from 2018 and 2019: “*Visualizing Hidden Ultrafast Processes in Individual Molecules by Single-Pulse Coherent Control*” in the *Journal of American Chemical Society*, 2018, 140, 15329-15335 and “*Two-Photon Induced Ultrafast Coherence Decays of Highly Excited States in Single Molecules*” in *New Journal of Physics*, 2019, 21, 045001.

4.1 Introduction

Quantum coherent control (CC) describes the active steering of quantum mechanical (QM) processes towards a desired final state. These schemes exploit induced QM interferences between excitation pathways, unwanted outcomes are efficiently suppressed by destructive interference and constructive interactions are used to force a process to a desired final state. The idea behind these experimental approaches emerged in the field of laser chemistry around 1980 to 1990 [113–118], where, *inter alia*, different products of a chemical reaction were selectively addressed under the irradiation of optimum waveforms of a pulsed excitation field. Today CC schemes are applied to a large variety of samples, including ions [23], molecules [20, 119–121], plasmonic nanostructures [122] and semiconductors [24, 123, 124]. In order to exploit quantum interferences, the existence of coherence is a prerequisite. However, in such complex systems, interacting with highly dynamical surroundings, the usual lifetime of coherence is in the order of some tens of fs up to several hundreds. Hence, a pulsed excitation with pulse widths in the same order or even smaller than typical dephasing times is one of the key components in such experiments.

Next to only manipulating the outcome, CC can help to understand fundamental underlying processes. For photo active systems, the interaction with its environment will change the outcome of a photoinduced process. Thus embedding a quantum system in a complex environment, which indeed corresponds to reality for the majority polymers or proteins, constitutes a great challenge in this field. A first step towards the active control of chemical and biological processes on a truly molecular level is the CC of single molecules in complex environments. Usually CC schemes exploit multiphoton processes, which require relatively strong excitation powers [22, 27, 125], therefore a high photostability of the material under investigation is essential. Furthermore, the interaction of a single molecule with its local surrounding increases the difficulty of understanding these systems. Each environment is different and therefore QM properties, such as the energetic excited state landscape or the ultrafast dynamics are *a priori* unknown for the respective molecule, which finally complicates the analysis of the matter - electromagnetic (EM) field interaction of the CC experiment.

The central aspect of this thesis is a new approach of combining an ultrafast pulse shaping setup with a theoretical quantum dynamics identification (QDI) procedure. With a pulse shaper, user defined phase and amplitude masks are modulated on top of the pulsed excitation field. Using MeLPPP, a CP with high photostability, 2P based CC experiments yield different PL signals in dependency of the modulation pattern. The QDI procedure is then able to find a model, based on the Lindblad-master equation,

which reproduces the experimentally obtained data with high quality and with minimal residual S (see Eq.2.36). Section 4.2 demonstrates the generation of coherence between two electronic levels by a first excitation pulse and subsequent probing of this coherence by the second pulse. Usually, the coherence decay is probed by one-photon transitions. However, here, two-photon absorption processes between two electronic levels are exploited. The QDI procedure extracts information about the involved energetic levels and ultrafast dynamics, but stays independent under variation of the Rabi-coupling. Therefore, more complex phase-only shaping approaches, shown in Section 4.3, are used to refine those parameters and finally obtain reliable information about the coupling strengths. Moreover, the latter experiment demonstrates that processes beyond the pure two-photon absorption can take place with significant probabilities and change the expected 2P absorption response, based on well-established theories [22], towards unexpected chirp dependencies.

4.2 Two-Photon Induced Coherence Decays

Experimental

The MeLPPP film were produced as described in section 3.2 and mounted to the x-y-z-sample holder in between the excitation and detection objective. The optimum position of the cover slip, which is reflected by the highest 2P induced PL signal, was found by tuning the z-direction screw and stayed unchanged during the whole experiment. The Ti:Sa oscillator was set to produce a spectrum overlapping considerably with the pure electronic peak of the 2P allowed absorption at 26380 cm^{-1} of MeLPPP (two photon energy), but still in the spectral transmittance of the pulse shaper between 11764 cm^{-1} and 13333 cm^{-1} (one photon energy). The time-averaged excitation energy was 2.5 mW, measured in front of the excitation objective. With the objective of NA=0.5, this translates into $\approx 90 \frac{\text{kW}}{\text{cm}^2}$, and with the repetition rate (80 MHz) into an energy per pulse and area of $\approx 1 \frac{\text{mJ}}{\text{cm}^2}$. To separate the PL from the excitation, two blue glass filters of thickness 3 mm (BG39) and one dielectric filter (short pass 492 nm) were used. To clarify the spectral overlap, both, the normalised excitation and absorbance, are shown again in Fig. 4.1 (a). The excitation spectrum is plotted against the 1P energy of the field, whereas the absorption against the 2P energy, reflecting actual energy of the 2P allowed excited state above the ground state. The data of the fluorescence excitation spectrum are taken with permission from reference [93]. The spectral overlap is big enough to generate sufficient excitation probability in S_2 and after internal conversion into S_1 the radiative depopulation of S_1 can be detected with the photon counting

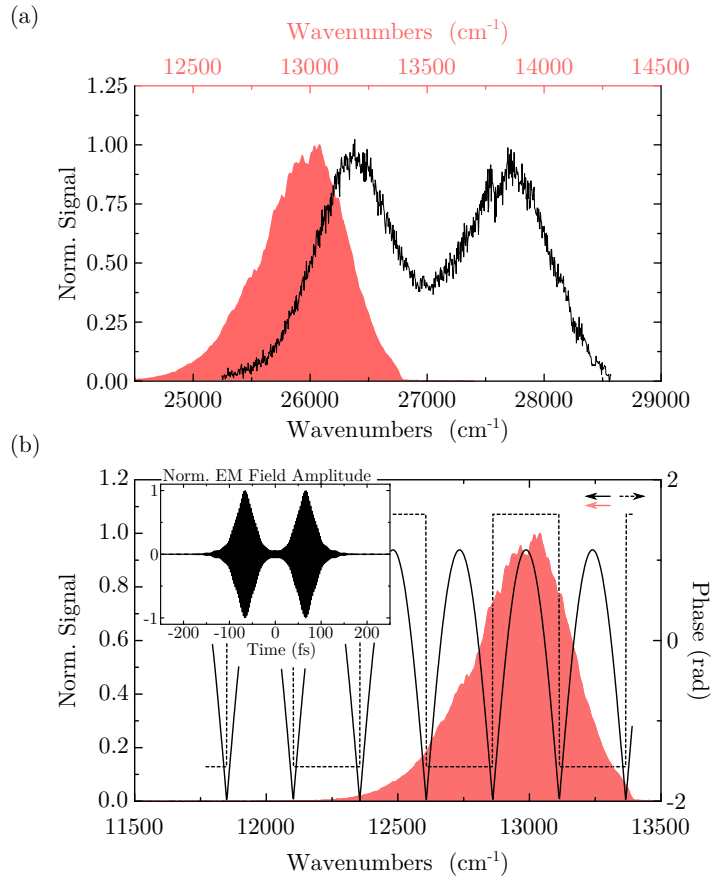


Fig. 4.1: Time and Spectral Dependent Characteristics of the Excitation. (a) Respective spectrum of the excitation of the Ti:Sa oscillator (red filled area) in dependency of the one photon energy (red scale) and two-photon induced fluorescence excitation spectrum of a MeLPPP film at room temperature (black solid line) in dependency of twice the one photon energy (black scale). (b) Amplitude (solid) and phase (dashed) mask in dependency of the energy, with respect to the excitation spectrum (red filled). The delay was set to 132 fs and the center modulation energy was 12987 cm⁻¹ (770 nm). For calculation of the amplitude and phase mask see equations 3.4 and 3.5. The inset shows the normalised time dependent electro-magnetic (EM) field amplitude of this particular modulation, which was calculated BY Fourier transform of the spectrally modulated amplitude.

module. However, the off-resonance with the first vibronic peak of the 2P allowed state is still big enough, which, if not, would complicate the interpretation a lot.

The generation of a double pulse sequence of two pulse replica requires an oscillatory amplitude modulation (see Eq. 3.4), where the inverse period of the spectral modulation reflects the time dependent delay τ . Furthermore, the defined exploitation of quantum interferences makes the knowledge about the relative phase between the pulse replica necessary, why the relative phase difference was fixed to 0 for all values of τ (Eq.3.5). The modulation patterns are plotted in Fig.4.1 (b) for a delay of $\tau = 132$ fs and a center

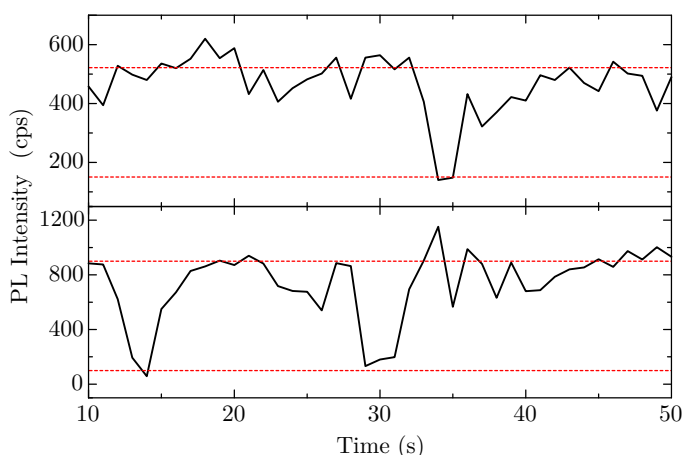


Fig. 4.2: Intensity Trace of Two Single Molecules Under Constant Excitation. Intensity trace of two individual MeLPPP molecules at room temperature embedded in polystyrene under constant excitation (solid black) in dependency of the elapsed time. Red dashed lines represent a guide to the eye for the two intensity intermittency levels: “on” (upper line), with emission of the molecule and “off” (lower line), which is the background.

modulation energy of 12987 cm^{-1} in dependency of the energy. The Fourier transform of this shaped excitation yields the time dependent EM field amplitude shown in the inset, reflecting two pulse replicas centred around 0 fs with a delay of 132 fs.

To test, whether multiple or single chromophores are in the excitation volume, the 2P induced PL intermittency under TL excitation was checked before the data was taken (see Fig.4.2). If the intermittency jumps digitally between a finite signal strength and the background (red dashed lines), the measurement was started. At this point the emission originates only from one single chromophore on the MeLPPP chain. Furthermore, for all measurements a “number-of-emitter” test was added: in the beginning and end of each τ -scan a TL excitation was performed for one second. If the signal strength between the TL excitation before and after the τ -scan differ significantly, the number of emitting chromophores has changed and the data was not taken into account. Hence, all data shown in the following sections deal with single emitters and therefore the usage of the phrase “single molecule” is justified. This is exemplary shown for two different MeLPPP molecules in Fig.4.2. The PL intensity jumps between two average counting rates (marked with red lines as guide to the eye), which represent the on- and off-states of the molecule inside the excitation volume. The lower limit represents the background counts around 100 cps. As the generation of a double pulse sequence requires amplitude shaping techniques, the equal time-averaged excitation power for all applied delays τ must be ensured. Therefore additional transmission masks were further applied to each particular modulation pattern.

	Energy E_2 (cm^{-1})	Dephasing time $\frac{1}{\gamma_2}$ (fs)	Relaxation time $\frac{1}{\Gamma_{21}}$ (fs)
Molecule in (b)	26010	77	146
Molecule in (c)	25951	72	155
Molecule in (d)	25947	52	265

Tab. 4.1: Optimal Model Parameters for Three Individual Molecules. Parameters of the energetic landscape and ultrafast dynamics for the minimum model describing the data shown in Fig. 4.3 (b, c, d).

Results

The well-known energy landscape of the ground, the first excited and the second excited state [93], which is only accessible via 2P absorption, allow to perform the measurement of the coherence decay induced by 2P absorption between S_0 and S_2 . As the PL originates solely from S_1 upon the excitation of S_2 , the IC into S_1 is highly efficient with a rate of $\frac{1}{150} \text{ fs}^{-1}$ [38], and the detected signal reflects the generated population in S_2 . These fundamental informations are summarised already in Fig.4.3 (a). The double pulse experiment works as follows: the first pulse generates 2P-induced coherence between S_2 and S_0 , which starts to get lost over the time due to molecule-host interactions. The characteristic time constant describing this decay is called dephasing time. The second pulse induces quantum mechanical excitation path interferences, which finally generates more or less population in S_2 depending on the remaining coherence in the system. This experiment is shown for three different molecules in Fig.4.3 (b, c, d) for delays between 0 and 250 fs in 6 fs steps (empty circles). Although the signal strengths are significantly different, especially between the first and the third one, the shape of the decay itself is similar and despite the noisy data, a clear reproducible change in the intensity can be determined. Note that all displayed measurements are not background corrected in order to demonstrate the absolute magnitude of the observed effects in comparison to the background and noise level. All coherence decays exhibit a fast reduction of the PL intensity for delays smaller than 75 fs (grey dashed line). If the delay exceeds this value, the PL counts do not change dependent on the delay and the so called *incoherent signal* level is reached. The obtained optimal values from the QDI procedure for the three molecules are listed in Table 4.1. Sudden variations in the PL intensity, e.g. jumps to intensity levels considerably higher or lower than the signal before and after (see Fig.4.3 (b) high data point below 200 fs), can be ascribed to spectral diffusion and background fluctuation, which is a well-known artefact of single-molecule experiments. The grey filled area in (b) reflects the measured collinear intensity autocorrelation envelope of the TL excitation pulse.

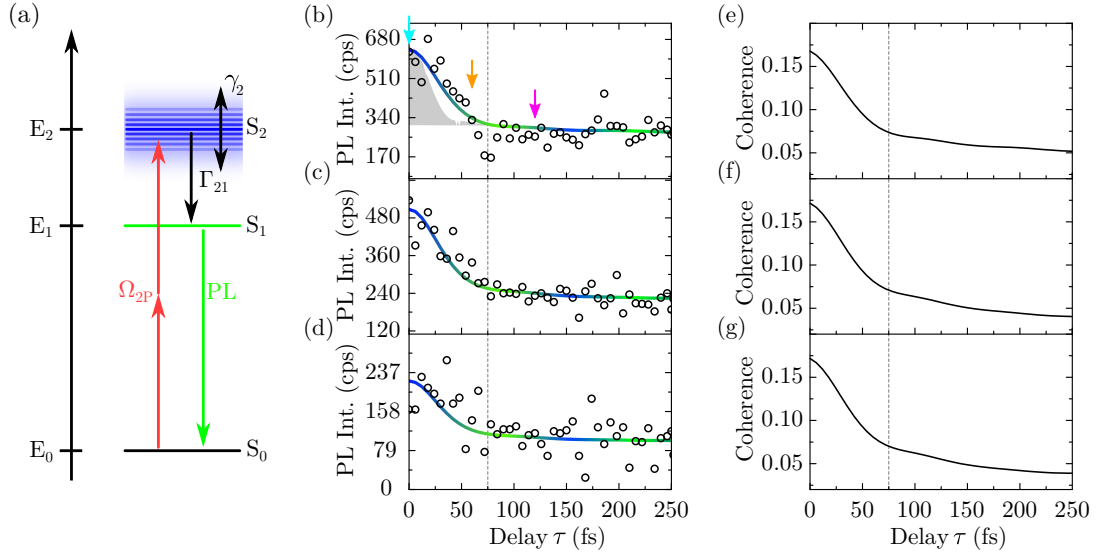


Fig. 4.3: Coherence Decays of Single Molecules. (a) Energy level diagram and dynamics involved in the coherence decay measurements. Population is transferred from the ground state S_0 to the second excited state S_2 via two-photon absorption processes (red arrows, described by the Rabi-coupling Ω_{2P}). Dephasing (γ_2) effects the generated coherence and the population can relax with rate Γ_{21} into the radiative first excited state S_1 , from where photoluminescence (PL) can be detected. (b, c, d) coherence decays of three different molecules in dependency of the delay τ . The grey dashed line reflects 75 fs and the arrows mark positions, which refer to Fig.4.6. The grey filled area presents the collinear intensity autocorrelation envelope of the excitation pulse. (e, f, g) Delay dependent simulations of the quantum coherence, calculated from the identified coherence decays in (b, c, d). Grey dashed lines mark a delay of 75 fs.

To demonstrate the reliability of the obtained coherence decays of intra-molecular processes, Fig.4.4 shows the PL intensity for a variation of the phase parameter δ from 0 to 6π in 51 steps for an ensemble of MeLPPP dissolved in toluene. Thereby the delay τ between the pulse pair was fixed to 70 fs, which exceeds the pulse width. Therefore all possible excitation power influence due to intensity autocorrelation effects can be excluded at this time. The measurement was carried out on an ensemble of MeLPPP, as photobleaching-effects complicate the acquisition of various subsequent measurements on one and the same molecule. Clear variations with a maximum contrast of around 0.4 are obtained between even and uneven multiples of π . The grey dashed line reflects the time averaged excitation power which was set to be equal for all modulation masks.

Following the measurement, the QDI procedure was carried out for each single molecule trace by Prof. Dr. Chuan-Cun Shu (Institute of Super Microstructure and Ultrafast Processes, Central South University, Changsha, China). The input parameters were chosen based on the known parameters from earlier publications for the energetic landscape and ultrafast dynamics [38, 53, 93]. The values of E_0 , E_1 and Ω_{Rabi} were fixed to 0 cm^{-1} , 22000 cm^{-1} and 120 cm^{-1} , respectively, and the initial parameters

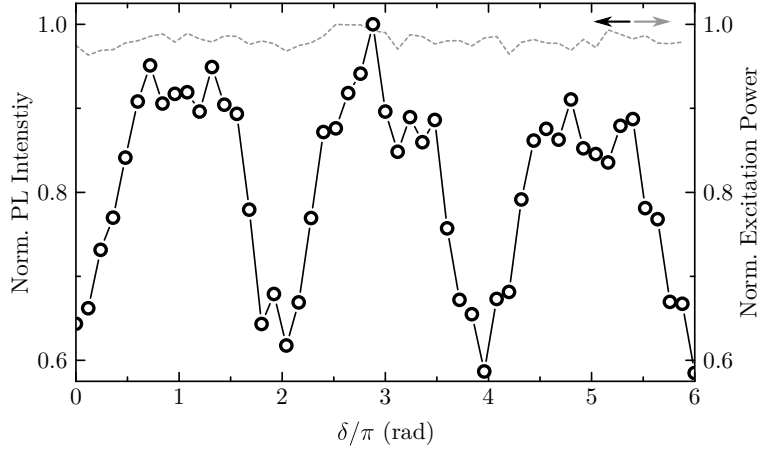


Fig. 4.4: Phase Scan of Double Pulse Sequence for an Ensemble Sample. Normalised photoluminescence (PL) intensity of an ensemble MeLPPP sample in dependency of the phase parameter δ . Modulation masks of the amplitude and phase have been set to $T_{\text{mod}} = |\cos(\frac{1}{2}[(\omega - \omega_{\text{mod}})\tau + \delta])|$ and $\phi_{\text{mod}} = \frac{\pi}{2}\text{sgn}(\cos(\frac{1}{2}[(\omega - \omega_{\text{mod}})\tau + \delta]))$, respectively, with $\tau = 70$ fs and $\omega_{\text{mod}} = 12903$ cm^{-1} . The grey dashed line reflects the averaged excitation power for each modulation mask. The data was taken with the modified setup described in Section 3.3 in “Setup Modifications for S-CBT Measurements” with $P_{\text{exc}} = 3$ mW.

were set to $E_2 = 26000$ cm^{-1} , $\frac{1}{\gamma_2} = 75$ fs and $\frac{1}{\Gamma_{21}} = 150$ fs, but kept variable to find the minimum model. The fixed values are justified because on one hand S_1 is not optically addressed at all by the laser pulses and on the other hand the QDI procedure was not sensitive to the precise value of Ω_{Rabi} . As the population is taken 400 fs after the first interacting pulse not all excitation is decayed into S_1 , thus to resemble the experimental data, the population of both electronic states, S_1 and S_2 , is included. Thus the population obtained by the QDI is reflected by green-blueish solid line which refers to the color code in Fig.4.3 (a). Since the QDI is based on the Lindblad-master equation, see section 2.6, the procedure yields for each delay the time-dependent density matrix elements of the system (see also section 2.5). Next to the population of the electronic states, the off-diagonal elements ρ_{20} and ρ_{02} of the density matrix can be determined and plotted against the delay τ . This dependency is shown in the last panel in Fig.4.3 in (e, f, g). The coherence terms also resemble the dephasing dynamics within 75 fs, but however, slightly slower than the calculated population. The QDI procedure was carried out for 30 molecules and yields the statistics shown in Fig.4.5. The mean energy E_2 is 26000 cm^{-1} inside a bin width of 100 cm^{-1} . Furthermore, the dephasing is centred at 75 fs and spreads between 50 and 120 fs, whereas the relaxation time with an average of 150 fs is distributed between 100 fs and 260 fs.

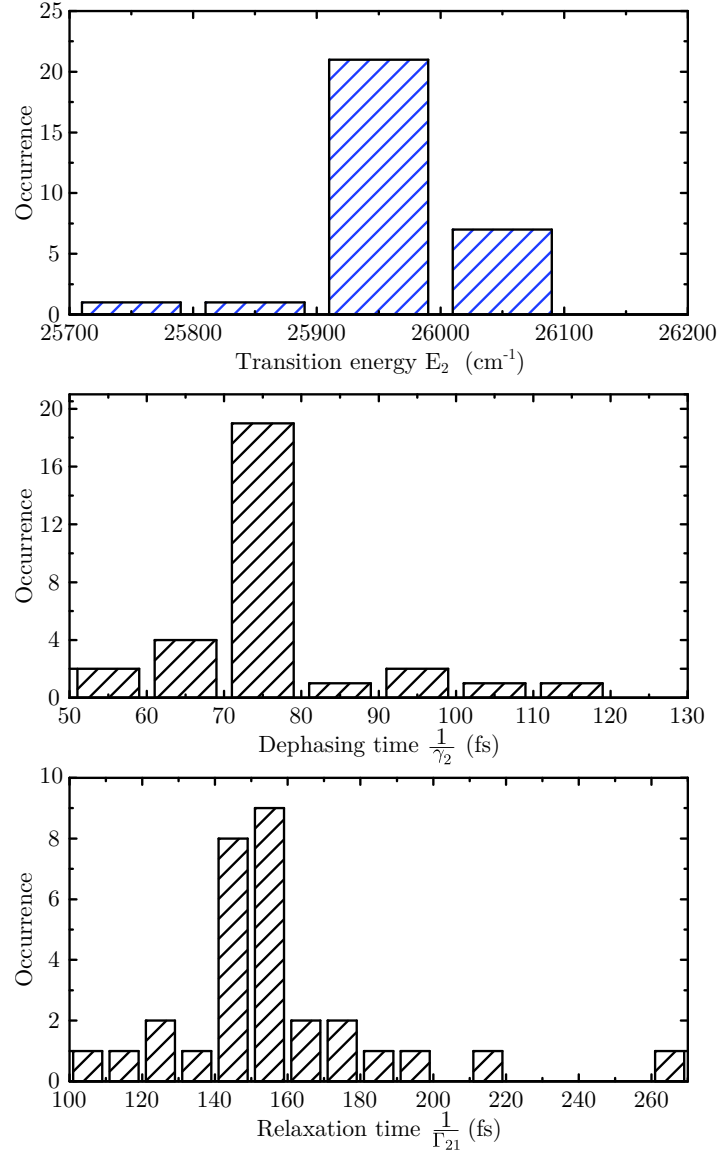


Fig. 4.5: Statistics on Energetic Landscape and Ultrafast Dynamics of Single Molecules. (a) Distribution of transition energy E_2 , with bin size 100 cm^{-1} (b) Occurrences of the dephasing time $\frac{1}{\gamma_2}$ and the relaxation times $\frac{1}{\Gamma_{21}}$ in (c), each with bin size of 10 fs.

Discussion

Fig. 4.3 (b, c, d) proof that high power multiphoton transitions are possible to induce in single MeLPPP molecules. Furthermore, the high 2P efficiency of MeLPPP, due to its strong symmetry relations (see section 2.3), and the high room temperature PL quantum yield of 25 % of state S_1 [108] lead to a considerably strong PL signal. Thus the 2P induced PL and changes due to pulse shaping approaches can be detected with

confidence. The shape of the obtained dependencies reflects constructive excitation pathway interferences, leading to an enhanced population transfer from the ground state S_0 to the second excited state S_2 of MeLPPP for short delays and no interference effects at all for larger delays. The maximum enhancement due to constructive interferences in a two level system is 2, which is true for the data shown (PL for $\tau \ll 50$ fs and $\gg 50$ fs). The comparison with the collinear intensity autocorrelation demonstrates, that the measured signal trace indeed resembles intrinsic ultrafast properties of MeLPPP, which is the coherence decay. Further proof provides the ensemble phase scan in Fig.4.4, with clear modulation of the PL with the parameter δ and therefore population transferred into S_2 . The considerable contrast taken for a double pulse sequence with $\tau = 70$ fs suggests still existent coherence, in agreement with the simulated coherence decays in Fig.4.3 (e, f, g). The steep and flat changes at even and uneven multiple of π can be ascribed to the detuning, as this data set was taken on an ensemble solution. The detuning will highly affect the PL response upon the double pulse excitation in a non-linear manner. The single molecule data is reliably reproduced by the QDI procedure with a mean dephasing time of 75 fs, mean relaxation time of 150 fs and mean transition energy of 26000 cm^{-1} , for all analysed molecules. These parameters perfectly resemble the already shown energy level diagram, with ultrafast dynamics included, shown in Fig.4.3 (a). The transition energy is near-resonant within the FWHM of the excitation of about 400 cm^{-1} , which makes sense, as in single-molecule experiments only those emitters are detected which lead to a high PL signal (which depends strongly on the spectral overlap). In contrast, for a PL-detected coherence decay of an ensemble solution in toluene clear detuning effects, reflected by oscillatory modulations, are evident (see appendix Section A.3). The statistics of E_2 with width 400 cm^{-1} therefore does not reflect the actual energetic landscape distribution inside the sample, but more the fraction of molecules with spectrally shifted absorption to resonance (within the excitation bandwidth). The actual distribution would exhibit a bigger bandwidth, which can be estimated from the ensemble absorption spectrum to be around 800 cm^{-1} (see Fig. 3.1 (c) and [93]).

The mean dephasing time $\frac{1}{\gamma_2} = 75 \text{ fs}$, ranging between several tens to 120 fs, translates into an upper limit for the mean homogeneous bandwidth of $\approx 450 \text{ cm}^{-1}$ (and 670 cm^{-1} to 280 cm^{-1} for the statistics boundaries). Earlier publications [13, 49] have shown, that the RT linewidth (FWHM) of state S_1 of a single MeLPPP chromophore of 260 cm^{-1} makes up a significant part of the ensemble spectra (600 cm^{-1}), indicating homogeneous broadening (HB), i.e. the dephasing, as a large influence in this quantum system. Note that for S_1 the radiative excited state lifetime of 800 ps is long compared to any dephasing effect and thus the effective dephasing time T_2 can be approximated

with the pure dephasing T_2^* [13, 49]. The HB influence holds also true for the second excited state S_2 investigated in this work. The ensemble linewidth is about 800 cm^{-1} , which is also approximately twice the homogeneous linewidth determined from the coherence decay measurements of 450 cm^{-1} . In analogy to S_1 this indicates also a significant contribution of HB to the ensemble inhomogeneous linewidth. However in the case of S_2 , the fast relaxation $\frac{1}{\Gamma_{21}}$ with mean time constant of 150 fs (in agreement with [38]) into the first excited state is not negligible any more in the consideration of the effective dephasing. Hence, the obtained decays of the coherence here, represent a decrease of the generated population ρ_{22} with a decay rate consisting of the sum of the dephasing and relaxation rates, γ_2 and Γ_{21} , respectively. This is further corroborated by the fact, that the delay dependent coherences in Fig. 4.3 (e, f, g) decay considerably slower than the population. Whereas coherence is still not fully lost at 75 fs (grey dashed line), the data in (b, c, d) almost reached the incoherent level. Hence, T_2 , the effective dephasing, is 50 fs, consisting of the pure dephasing (75 fs) and further population decay rates of the actual state, in this case the relaxation to S_1 (150 fs), which is perfectly resembled by the coherence decays. The fast relaxation is an internal conversion process. It depends strongly on the relative energetic positions between the pure electronic state of S_2 and higher vibrational levels of the first excited state S_1 [16], denoted with $S_{1,\nu}$. After transferring population from S_0 into S_2 iso-energetic internal conversion into $S_{1,\nu}$ and further vibrational relaxations takes place. The broad distribution of these relaxation times reflects therefore the energetic landscape of the analysed molecules inside the disordered matrix and agrees with the statistics of E_2 .

The QDI procedure is based on the Lindblad master equation (see section 2.6), thus, next to the state's populations, the time dependent coherences, i.e. the off-diagonal elements of the density matrix, can be extracted, too. With Eq. 2.33, the projection of the Bloch vector tip onto the z-y-plane can be calculated and plotted. This yields a figurative way to look at the ultrafast dynamics for distinct selected delays. In Fig.4.6 the Bloch vector dynamics of two single MeLPPP molecule (shown in Fig.4.3(a) and (c)) are plotted for three values of τ , 0 fs, 60 fs and 120 fs (turquoise, orange and magenta). Changes along the z-direction reflect population transfer from the ground state S_0 to the second excited state S_2 , whereas changes along the y-axis are ascribed to pure dephasing effects. Clearly the dynamics take place in the lower part of the Bloch sphere, with a maximum population transfer of 20 % from the ground state to S_2 for $\tau = 0$ fs. For bigger delays the dephasing clearly affects the trace between the double pulse interaction, reflected by the horizontal decline in the orange and magenta lines. Although both graphs show similar behaviours, with equal population transfer rates, the trace in the right panel is considerably stronger affected by a stronger

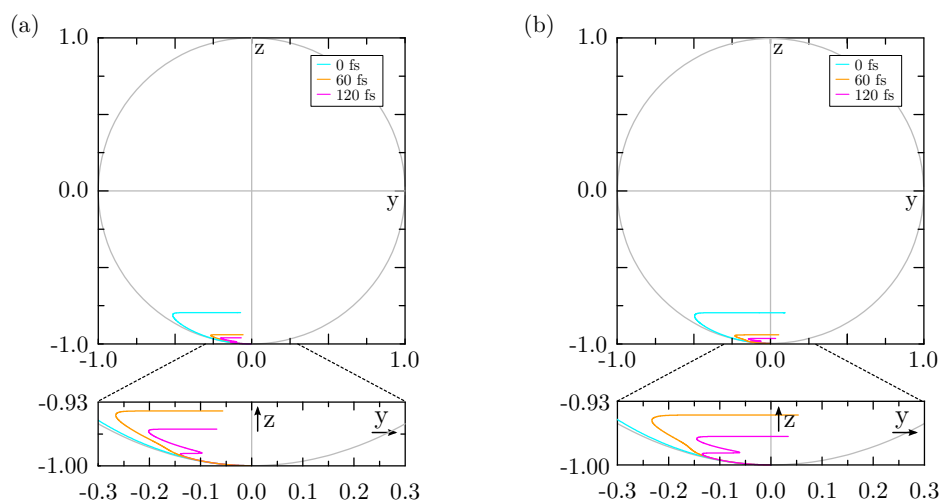


Fig. 4.6: Bloch Vector Tip Dynamics of Two Individual MeLPPP Molecules. (a) Bloch vector tip projected onto the y - z -plane for the molecule shown in Fig. 4.3 (a) for three different delays τ . (b) Bloch vector tip projected onto the y - z -plane for the molecule shown in Fig. 4.3 (c) for three different delays τ .

loss of coherence for delays $\tau > 75\text{ fs}$ (magenta line). This molecule does exhibit a faster dephasing time of $\frac{1}{\gamma_2} = 52\text{ fs}$ than the molecule in the left panel with $\frac{1}{\gamma_2} = 77\text{ fs}$ (see Table 4.1), which reduces the possibility of constructive excitation pathway interferences. However the relaxation is considerably slower for the former molecule which finally yields a comparable effective dephasing with T_2 and similar shape of the coherence decay. Furthermore, all decay traces analysed exhibit a contrast of 2, i.e. the ratio between $\tau = 0\text{ fs}$ and $\tau \gg 75\text{ fs}$, which is the theoretical maximum, but the Bloch plots in Fig. 4.6 clearly fail to reproduce that measured contrast, reflected by the z -axis intersections in the Bloch plots. This discrepancy can be explained by the populations shown here. Whereas the coherence decay represents the population dynamics of both states S_1 and S_2 the Bloch plots only reflect the dynamics between S_0 and S_2 . Thus, relaxation effects into S_1 , which reduce the population of S_2 with a mean rate of $\frac{1}{150}\text{ fs}^{-1}$, will be evident in the calculated Bloch vector tip dynamics and increase the contrast between $\tau = 0\text{ fs}$ and $\tau \gg 75\text{ fs}$.

Conclusions

The shown data demonstrate the first ultrafast, 2P-induced measurements of the coherence decay in individual organic molecules in a disordered matrix at room temperature. These decays can be identified with the envelope of the optical free induction decays of single emitters, taking the ergodic principle into account [20]. Although each molecule represents a completely unknown system at first, the combination of

the experimental approach with a novel QDI procedure yields reliable and physically reasonable parameters to describe the obtained PL dependencies with a minimum model of the ultrafast dynamics. As each molecule faces different surroundings, both, the energetic landscape as well as the ultrafast dynamics are strongly influenced. The histograms of the obtained optimum parameters of the transition energy E_2 , the dephasing time $\frac{1}{\gamma_2}$ and the relaxation time $\frac{1}{\Gamma_{21}}$ reflect the diverse energetic landscape through the sample from molecule to molecule. However, this variety of interactions and surroundings is not directly accessible through the shape of the decay in this case, as e.g. the Rabi-coupling did not influence the shape of the simulations. All traces itself exhibit a contrast of 2 between $\tau = 0$ fs and $\tau \gg 75$ fs and decay within the first 75 fs to the incoherent level. The combination of possible relaxations from S_2 into S_1 and the fast dephasing lead to similar behaviour of the measured PL dependency for all analysed molecules. Different contrast factors were not obtained. This is in agreement with the QDI results on the population transfer efficiencies between the ground state and the second excited state. These were determined to be around 20 % which finally suggest the interaction of the molecule with the EM field to take place in the weak coupling regime.

4.3 Visualising “Hidden” States by Single Pulse Coherent Control

Experimental

In order to perform single-molecule phase dependent two-photon absorption measurements, similar samples, as described before, were produced. The cover slip, with the film on top, was again mounted to the excitation/detection unit into the setup and the optimal position with maximum 2P induced PL was found by moving the sample along the direction of beam propagation and simultaneous detection of the signal strength. The averaged excitation power, measured in front of the $NA = 0.5$ excitation objective was set to 3 mW. The PL was again collected with an objective of $NA = 0.85$ and to block all excitation two blue glass 39 filters of thickness 3 mm and one dielectric filter blocking everything above 20325 cm^{-1} (short pass 492 nm) were used.

The generated modulation pattern reads $\varphi_{\text{mod}} = \frac{1}{2}\beta(\omega - \omega_{\text{mod}})^2$ for values of β ranging from -3000 fs^2 to 3000 fs^2 in 51 steps. Furthermore, a $\varphi_{\text{mod}} = 0$ and $T_{\text{mod}} = 1$ mask was added in the beginning and end of each β -scan, to check whether the molecule has photobleached or the PL has significantly changed. Two exemplary phase modulations are plotted in Fig.4.7 (a) for a TL pulse (dashed) with $\varphi_{\text{mod}} = 0$

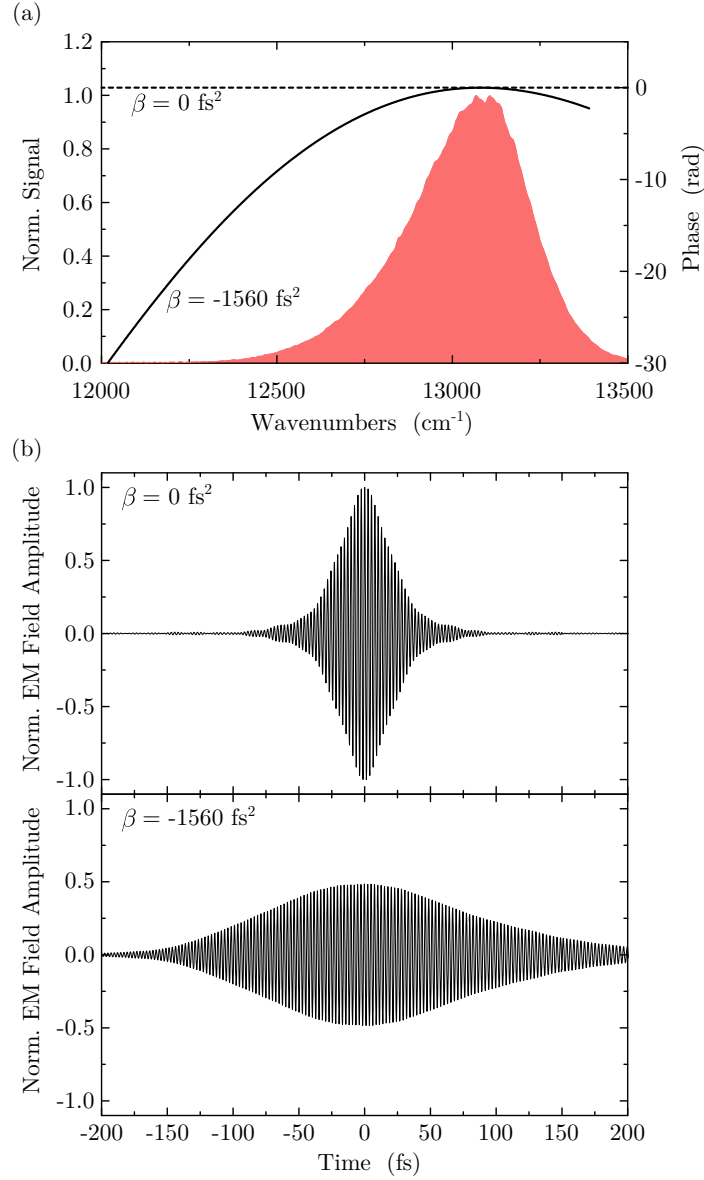


Fig. 4.7: Spectral and Time-Dependent Characteristics of the Excitation. (a) Laser spectrum against one-photon energy scale, centred around 13080 cm^{-1} with full width at half maximum of $\approx 400 \text{ cm}^{-1}$ (red) and two exemplary spectral dependent phase functions for a value of $\beta = 0 \text{ fs}^2$ (dashed) and -1560 fs^2 (solid, see Eq.3.3). (b) Respective Fourier transform of the experimental spectral amplitude of the electro-magnetic (EM) field with phase modulation for a transform limited (upper panel) and negatively chirped (lower panel) pulse.

and negatively chirped pulse with $\varphi_{\text{mod}} = -\frac{1}{2}1560 \text{ fs}^2 (\omega - \omega_{\text{mod}})^2$ (solid line) over a respective spectrum at 13000 cm^{-1} with $\text{FWHM} = 400 \text{ cm}^{-1}$. In (b) the respective Fourier transform of the shaped experimental spectrum is plotted. Clearly, the phase affects the overall peak power and shape of the time dependent pulse envelope.

Furthermore, each energy is linearly shifted in time, higher energies to earlier times with respect to the low energy part of the laser spectrum. Finally a negatively (positively) chirped pulse exhibits a linear sequence of energies beginning with the blue (red) side of the spectrum and continuously decreasing (increasing) in energy. Note that a quadratic phase modulation of the EM field is commonly referred to as *linear chirp*, as the energies through the EM spectrum will be shifted linearly in time with dependency on the applied β value. The measurement was carried out for multiple molecules under ambient conditions.

Results

The phase dependent measurement was carried out at first for an ensemble film sample of MeLPPP (embedded in polystyrene as well). The obtained 2P induced PL dependency on β is shown in Fig.4.8 (a). The maximum PL signal is centred at $\beta = 0$ fs² and for increasing $|\beta|$ -values the signal vanishes symmetrically around its global maximum. The grey solid line reflects the calculated 2P absorption probability P for an applied linear chirp phase function and reads [22]

$$P = \left| \int A\left(\frac{\omega_0}{2} + \Delta\right)A\left(\frac{\omega_0}{2} - \Delta\right)e^{i[\varphi\left(\frac{\omega_0}{2} + \Delta\right)\varphi\left(\frac{\omega_0}{2} - \Delta\right)]}d\Delta \right|^2, \quad (4.1)$$

where A is the spectral amplitude of the excitation, with a detuning of Δ from the half of the transition energy $\omega_0 = 27188$ cm⁻¹, and φ is the respective spectral phase of the EM field (in this case φ is equal to the pure phase function φ_{mod}). The maximum of the calculated 2P transition is also located at 0 fs² and decreases symmetrically for increasing $|\beta|$ -values.

In Fig.4.8 (b - g) the same measurement on six different single MeLPPP molecules is shown, which demonstrates the reliable control of the 2P induced PL (open circles) with a linear chirp. The first three datasets (b - d) exhibit the same symmetric behaviour (with respect to their maximum and to $\beta = 0$ fs²) under variation of β as the ensemble data, with the highest PL signal under a TL pulse excitation. In contrast, the remaining three single molecule PL traces in Fig.4.8 (e - g) differ considerably from the symmetric shape, with steeper in- or decreases for positive and negative values of β . This behaviour was found for a significant part of the analysed molecules and is denoted as asymmetric response. “Asymmetry” describes the difference of the PL signal for a positive and a negative β , with equal absolute value (grey dashed lines in Fig.4.8 (e - g)), which is significantly bigger than the calculated error of ± 42 cps. For example, does molecule 4 in Fig.4.8 (e) exhibit a clearly steeper decrease of the PL for negative values of β than for positive ones. Opposite behaviour is found for molecule 5 and 6, with a steeper

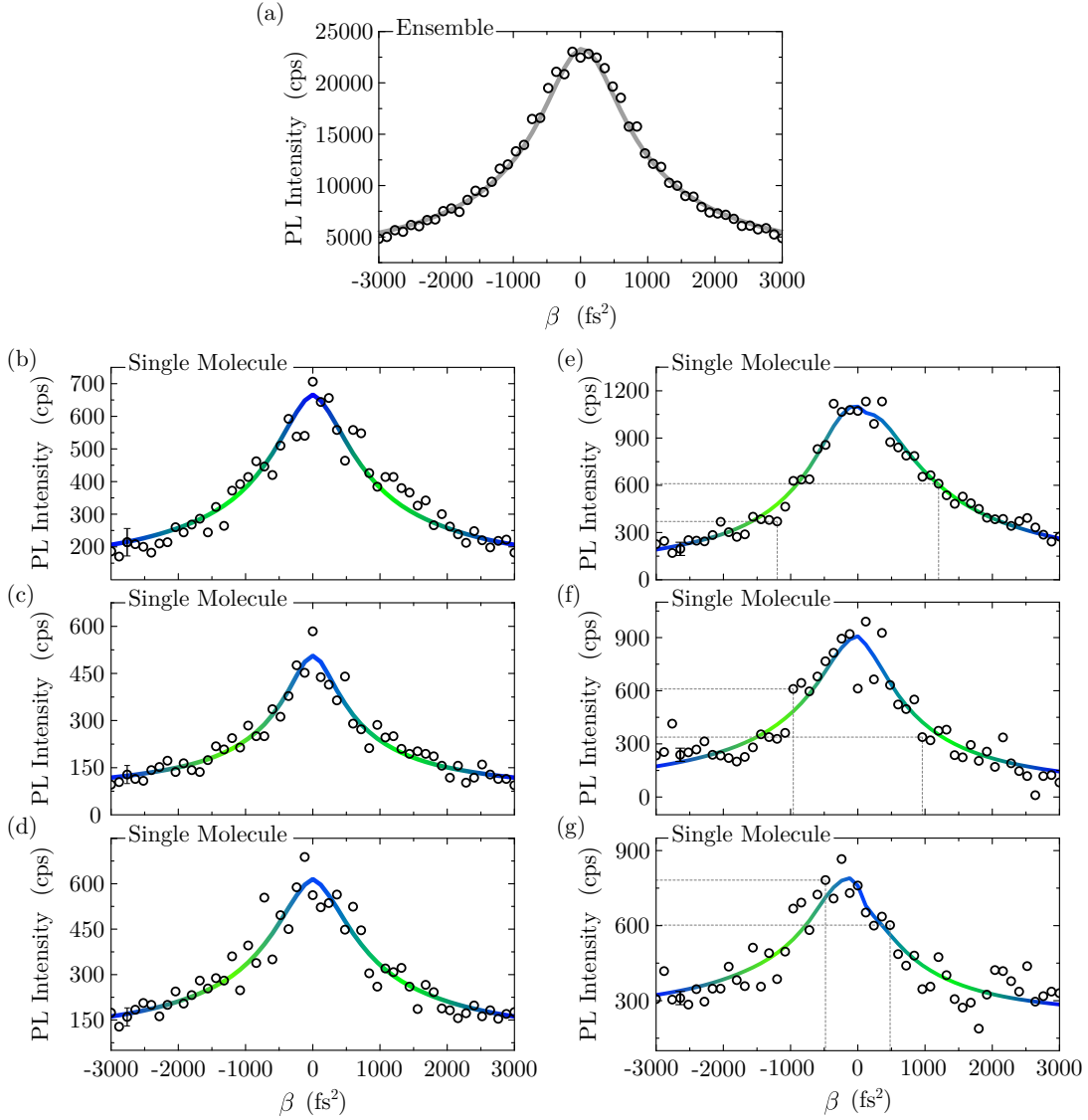


Fig. 4.8: Coherent Control of Two-Photon Induced Absorption in an Ensemble and in Single Molecules. (a) Photoluminescence (PL) detected linear chirp measurement of an ensemble MeLPPP sample under ambient conditions (open circles) and calculated two-photon absorption probability according to [22] (solid grey line). (b, c, d) Measurements of the PL in dependency of β for three different single MeLPPP molecules (open circles, 1, 2 and 3 from top to bottom) and QDI results on a minimum three-level model with parameters shown in Table 4.2 (green-blue solid line). (e, f, g) Same measurement on three different molecules (open circles, 4, 5 and 6 from top to bottom) and QDI results on a minimum four-level model. Obtained parameters are listed in Table 4.2. The grey dashed lines reflect the different PL signal strengths for symmetric values of β . The calculated error is ± 42 cps (counts per second).

decrease for $\beta > 0$. Additionally to this asymmetric behaviour some molecules feature maximum PL counts for (weakly) chirped pulses, rather than for a TL excitation, which is evident in Fig.4.8 (g) with maximum signal at $\beta = -240$ fs².

4.3 Visualising “Hidden” States by Single Pulse Coherent Control

	Energy (cm ⁻¹)		Rabi freq. (cm ⁻¹)		Decay times (fs)		
	E_2	E_3	Ω_{2P}	Ω_{1P}	$\frac{1}{\gamma_2}$	$\frac{1}{\gamma_3}$	$\frac{1}{\Gamma_{21}}$
Mol.1 in Fig.4.8 (b)	25940	-	531	-	61	-	191
Mol.2 in Fig.4.8 (c)	26039	-	198	-	65	-	179
Mol.3 in Fig.4.8 (d)	25923	-	590	-	83	-	135
Mol.4 in Fig.4.8 (e)	25855	38626	674	366	72	73	152
Mol.5 in Fig.4.8 (f)	25914	39051	595	151	88	94	140
Mol.6 in Fig.4.8 (g)	25712	38712	619	338	62	52	172

Tab. 4.2: Three- and Four-Level Simulation Parameters. Obtained Parameters for a minimum three-level model and for a minimum four-level model for molecules shown in Fig.4.8(b - g).

The QDI procedure was carried out for all measured molecules as follows: the energies E_0 and E_1 were again fixed to 0 cm^{-1} , 22000 cm^{-1} , respectively. The initial parameters were set individually for each particular molecule and kept variable to find the minimum model. The specific values can be found in the appendix Section A.2 Table A.3. The green-blue solid line reflects in all cases the results of the QDI procedure, as equation 4.1, does not yield any information about the parameters inherent to the sample. The minimum model found for the symmetric cases, consists of three levels, the electronic ground state S_0 , the first excited S_1 (far off resonant with the excitation) and the second excited state S_2 , which is accessible by 2P absorption of the excitation. The determined parameters describing the ultrafast dynamics and the involved energetic landscape are listed in Table 4.2. Whereas the energy E_2 of state S_2 is again in near resonance with twice the excitation, the dynamical parameters, as well as the coupling strength are distributed around a mean value of $\frac{1}{\gamma_2} \approx 70 \text{ fs}$, $\frac{1}{\Gamma_{21}} \approx 169$ and $\overline{\Omega_{2P}} \approx 440 \text{ cm}^{-1}$ (see Fig.4.3 (a)).

To describe the asymmetric data, a pure three level model is not sufficient any more and the model has to be extended beyond that. Including a fourth highly excited singlet state S_3 , centred around 39000 cm^{-1} , as an additional loss channel for the population in S_1 & S_2 , the QDI procedure is able to reproduce the found behaviour with high quality (green blue solid lines). This third level was already measured in [38] and is accessible via a 1P absorption from the ground state S_0 . Using an Ulbricht-sphere, the PL quantum yield of this highly excited state was found to be less than 1 %, which justifies the loss channel character of this state. Finally, S_3 is depopulated non-radiatively and can not be detected by the photon detector. Furthermore, the missing signal in the 1P, as well as the 2P absorption spectrum between 26000 cm^{-1} and 39000 cm^{-1} justifies the denotation S_3 .

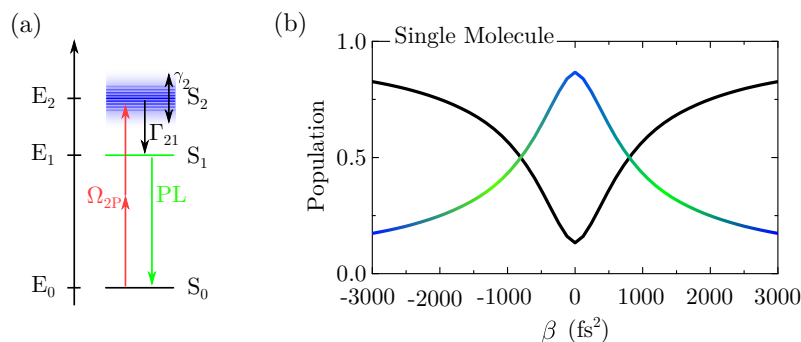


Fig. 4.9: 3-Level Model Simulations of β -Dependent Populations of a Single Molecule. (a) Minimum model to describe the symmetric single molecule data, yielded by the quantum dynamics identification (QDI) procedure, including the energies $E_{0,1,2}$ of states $S_{0,1,2}$, the dephasing rate γ_2 of S_2 and the relaxation rate from $S_2 \rightarrow S_1$, Γ_{21} . (b) Simulated populations of the ground state S_0 (black) and the sum of S_1 and S_2 (green-blue) in dependency of β .

Again, the QDI yields information about the involved energy landscape and ultrafast dynamics of each distinct molecule. The optimised parameters for the presented simulations in Fig.4.8 (b -g) can be found in Table 4.2, whereas new parameters, such as the energy E_3 of state S_3 , the 1P Rabi-frequency Ω_{1P} (coupling S_2 and S_3) and the dephasing of state S_3 , γ_3 were added. Now, this set describes a four-level model instead of a three-level model. The dephasing and relaxation of S_2 still vary around a mean of 74 fs and 155 fs, respectively. The energy E_2 is in near resonance with the excitation and $\overline{\Omega_{2P}}$ is approximately 630 cm^{-1} . The additional parameters are distributed around 285 cm^{-1} for the 1P Rabi-frequency and 73 fs for the dephasing of state S_3 .

Discussion

The ensemble data in Fig.4.8 (a) reflect the well known behaviour of a pure 2P transition between two electronic states in dependency of an applied linear chirp (see Eq.4.1). The maximum probability to induce a pure 2P transition is given for a TL pulse, which is $\beta = 0 \text{ fs}^2$, and the probability decreases symmetrically around that maximum. This quantum mechanical transfer of population probability can be traced by the emitted PL, as the population in the electronic states is proportional to the transfer probability and finally the PL is connected with the population only by multiplicative and constant factors (quantum yield of the state and detection efficiency of the setup). This symmetric behaviour can be found down to the level of single molecules, which is proven by Fig.4.8 (b-d). However, to determine the energetic landscape and the ultrafast dynamics, a complex model must be included, which is done by the QDI procedure. The traces are reproduced with high quality and the obtained

parameters fit well to earlier measurements (see section 4.2 and [9, 13, 38]). For the symmetric single molecule data, the QDI yields a minimum model consisting of three states, S_0 , S_1 and S_2 (see Fig.4.9 (a)). The important parameters are the dephasing γ_2 of S_2 which is finally responsible for the fast loss of coherence, the relaxation $S_2 \rightarrow S_1$ and the energy E_2 . Latter is in near resonance with doubled the excitation energy, centred at around 13000 cm^{-1} . Again, in single molecule experiments, only those emitters will be detected with confidence, which produce the highest PL signal, i.e. the absorption overlaps significantly with the excitation spectrum. Consequently the Rabi-coupling is relatively strong with an obtained average of 630 cm^{-1} . The determined values for γ_2 perfectly fit to the experimentally obtained values of the dephasing, analysed in section 4.2, where the measurement of the coherence dynamics yield a mean dephasing of 75 fs. Furthermore, the relaxation Γ_{21} was already found to be around 150 fs [38] by fs-pump-probe measurements on an ensemble of MeLPPP, which is in agreement with the identified three-level model here. The strong variety of all obtained parameters determine the shape of the β -dependent traces, including the steepness of the curvature of the rising or decreasing wing and the width of the trace (measured at half maximum) (see appendix Section A.4). This diversity reflects the heterogeneity from molecule to molecule inside the disordered matrix at room temperature and, furthermore, fit to the statistics found in section 4.2. Next to the excited state landscape, the depopulation of the ground state can be additionally determined from the QDI procedure, which provides a direct access of all instantaneous processes involved in the 2P absorption from S_0 to S_2 . For molecule 1 in Fig.4.8 (b) this graph is shown in Fig.4.9 (b). Clearly, all population, in the ground state and in both excited states decrease and increase symmetrically around $\beta = 0 \text{ fs}^2$. In other words, the depopulation of S_0 takes place to the same extent as the population in state S_2 and S_1 . This means that the first and only process generating the obtained PL signal is indeed the 2P absorption into S_2 from the electronic ground state.

Remarkably, a significant part of the single molecule data exhibit asymmetric PL decreases in dependency of β . The examples shown here in Fig.4.8 (e-g) furthermore proof that this asymmetry is reproducible but does not resemble the exact shape from molecule to molecule, with varying steepness. Next to the asymmetric wings of the trace, even the global maximum can be shifted to values different from $\beta = 0 \text{ fs}^2$. These shapes can not be reproduced with the simpler model shown in the paragraph above in Fig.4.9 (see appendix Section A.5). The extended model is shown in Fig.4.10 (a): 2P absorption takes place between the ground state and S_2 , whereas relaxation from the latter to S_1 is still highly efficient. Now, the existence of the highly excited state S_3 , gives rise to an additional transition $S_2 \rightarrow S_3$. Due to symmetry considerations this

1P absorption is allowed and the probability to induce this transition is non-negligible. The symmetry relations for the point group C_{2h} of MeLPPP set the product of the symmetry species of the one-photon dipole operator with the initial and final state ones to be an even species, otherwise the transition matrix dipole element is 0 and the transition is forbidden. With the alternating symmetry of the quantum mechanical wave functions of the molecules [40] S_3 is found to be an uneven species and the transition is described by

$$\begin{aligned} \Gamma(S_3) \times \Gamma(\hat{p}_{x,y}) \times \Gamma(S_2) &= A_g \\ B_u \times B_u \times A_g &= A_g \quad \text{with} \quad \Gamma(\hat{p}_{x,y}) = B_u \quad , \end{aligned} \quad (4.2)$$

whereas the z-component of \hat{p} was neglected again (see section 2.3). However, the reverse transition, i.e. the relaxation from S_3 into S_2 does not take place, as the isoenergetic transitions from S_3 into a manifold of highly excited states (vibrational, charge separated etc.) of preceding singlets and triplets is more efficient (crossed grey arrow), which is proven by the extremely low quantum efficiency of $< 1\%$ of S_3 . Finally, all population transferred into S_3 is deactivated non-radiatively and cannot be detected with the photon counting module, which constitutes as a loss channel for this experiment and the simulation. This extension yields extremely good agreement between the data and the QDI simulations shown in Fig.4.8 (e, f, g).

Again, the populations of all involved states can be accessed by the QDI procedure and are plotted in Fig. 4.10 (b, c, d). Although the obtained PL signal and population of S_2 and S_1 is clearly asymmetric, the depopulation of the ground state (black solid line) of each molecule is symmetric around $\beta = 0 \text{ fs}^2$. This leads to the conclusion, that the first step of this complex sequence of processes is always a non-resonant 2P absorption into the second excited state in analogy to the symmetric cases shown before. However, the β -dependent populations of S_3 exhibit strong asymmetric shapes, notably, with opposite behaviours with respect to the population of S_1 & S_2 . This additional 1P transition is highly dependent on the interplay between the energy mismatch $E_3 - E_2$, the instantaneous excitation frequency of the linearly chirped pulse and the 1P Rabi-coupling Ω_{1P} . In other words, for a fitting sequence of excitation energies (i.e. negative or positive β) S_3 is efficiently populated and the population in S_1 , conducting to a PL intensity signal, is lost. Finally the asymmetry is due to the chirp-dependent efficiency of the transition $S_2 \rightarrow S_3$ and therefore the process taking place can be denoted as a quasi-instantaneous 3-photon or (2+1)-photon transition.

To demonstrate the dynamical influence of the $S_2 \rightarrow S_3$ transition, Fig.4.11 displays the time-dependent population dynamics for two molecules (Fig.4.8(e) and (g)) for two different values of $\beta = \pm 1560 \text{ fs}^2$, $\pm 240 \text{ fs}^2$, which are also marked in Fig.4.8 with the

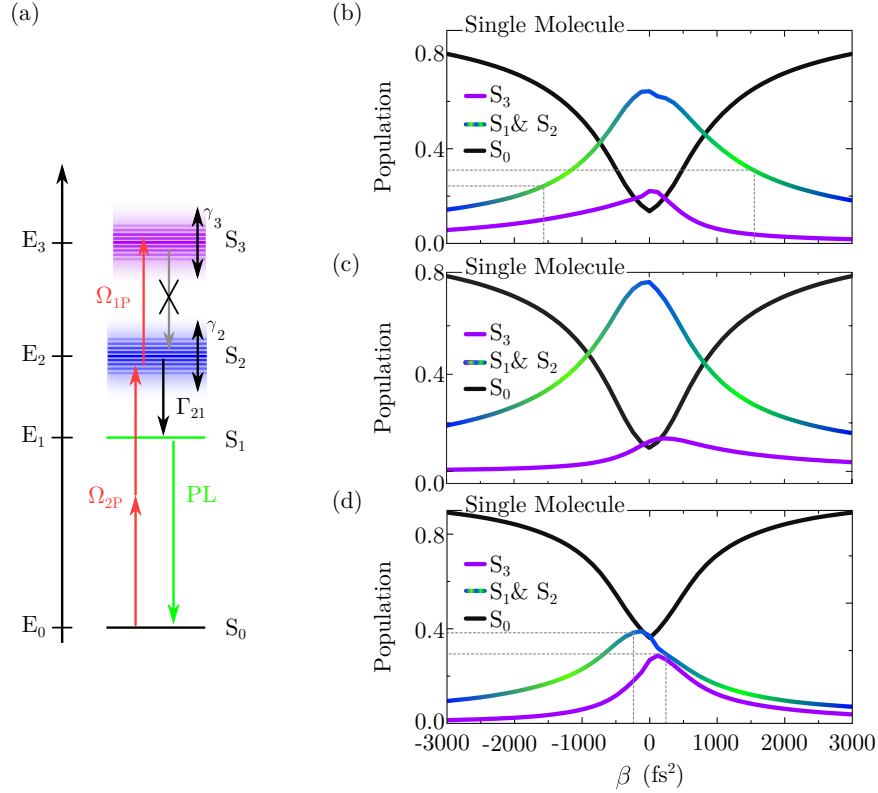


Fig. 4.10: 4-Level Model Simulations on the Population of Three Single Molecules. (a) Minimum model to describe the asymmetric single molecule data, yielded by the quantum dynamics identification (QDI) procedure, including the energies $E_{0,1,2,3}$ of states $S_{0,1,2,3}$, the dephasing rate γ_2 of S_2 and the relaxation rate from $S_2 \rightarrow S_1$, Γ_{21} , the one-photon and two-photon Rabi-couplings $\Omega_{1P,2P}$ and the finally the additional energy E_3 of S_3 and the respective dephasing rate γ_3 . (b, c, d) Simulated populations of S_0 (black), the sum of S_1 and S_2 (green-blue) and of the highly excited state S_3 (magenta) in dependency of β for the three different molecules shown in Fig.4.8 (e, f, g). The grey dashed lines in (b) and (d) mark the values of $\beta = \pm 1560$ fs² and $\beta = \pm 240$ fs².

grey dashed lines. The dynamics for each involved electronic state $S_{0,1,2,3}$ are plotted against the time in fs¹. The gradient coloured area reflects the strongly or weakly chirped pulse with increasing and decreasing energy in time. The first observation is that for the negatively chirped pulse the 2P transition from the ground state into the second excited state starts around -50 fs owing to a change in the population of S_1 & S_2 . The interplay between the absorption of the molecule, which is red shifted with respect to the ensemble absorption (see Fig.3.1) and the instantaneous excitation energy ω_i fulfils the resonance condition at this point in time and population is efficiently transferred. Close to 0 fs this transition is most efficient due to resonance and highest excitation

¹The notation “ S_1 & S_2 ” refers to the fact, that the populations of state S_1 and S_2 are summed up for graphic displaying

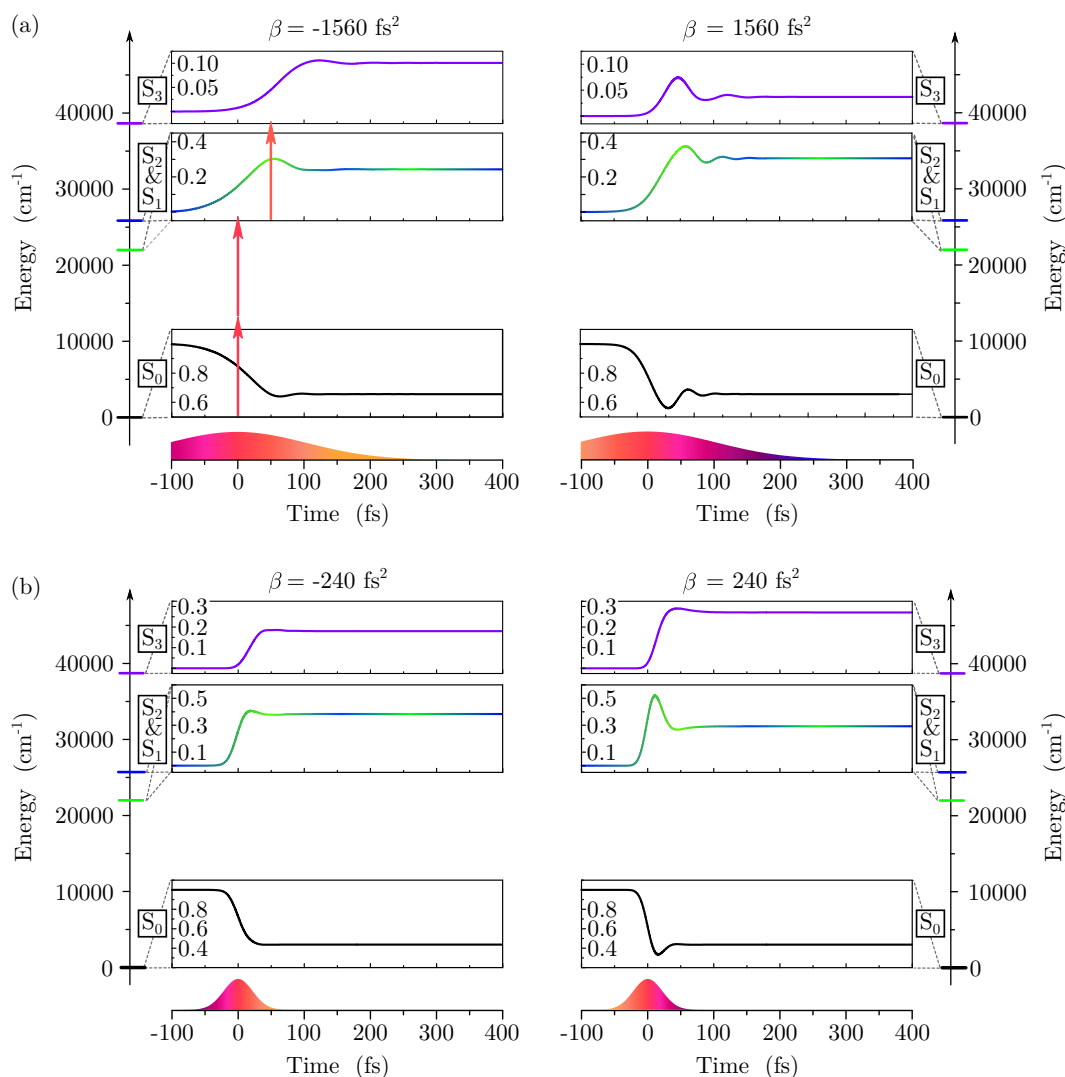


Fig. 4.11: Time-Dependent Population Dynamics for Different Values of $\pm\beta$. (a) Population dynamics of the single molecule shown in Fig.4.8 (e) for the states S_0 (black), S_1 & S_2 (green-blue) and S_3 (magenta) for a chirp parameter of $\beta = \pm 1560 \text{ fs}^2$ (left and right). The lower panel for $\beta = \pm 1560 \text{ fs}^2$ reflects schematically the linearly chirped pulse (large pulse width) with decreasing (increasing) energy in time. The red arrows display the two-photon absorption at $t = 0 \text{ fs}$ and for a lower energy the one-photon absorption from S_2 into S_3 at 50 fs . (b) Population dynamics of the single molecule shown in Fig.4.8 (g) for the states S_0 (black), S_1 & S_2 (green-blue) and S_3 (magenta) for a chirp parameter of $\beta = \pm 240 \text{ fs}^2$ (left and right). The lower panel for $\beta = \pm 240 \text{ fs}^2$ reflects schematically the linearly chirped pulse (small pulse width) with decreasing (increasing) energy in time.

power density. The transfer of population probability into S_3 , however, is delayed in comparison to S_1 & S_2 with an evident rising component starting tens of fs after the 2P process was induced. This behaviour is additionally demonstrated by the fast decrease of population of S_1 & S_2 around 50 fs , reflecting the transfer between S_2 and S_3 . This

subsequent 1P absorption, as mentioned above, is strongly dependent on the interplay between the instantaneous excitation energy, the energy difference between S_2 and S_3 and Ω_{1P} . With $E_3 - E_2 \approx 12770 \text{ cm}^{-1}$ only the lower energy wing of the excitation is resonant and for a negatively chirped pulse this transition is induced later. Although the 1P absorption $S_2 \rightarrow S_3$ is delayed, the efficiency is relatively high with transfer of population probabilities of $\frac{1}{3}$ of the amount in $S_1 \& S_2$, reflected by a significant loss of detectable PL intensity in the experiment. For the positively chirped pulse, on the other hand, both transitions, 2P and 1P absorption, start simultaneously closely to 0 fs, due to resonance conditions. Nevertheless, the interplay between the increasing energy of the instantaneous energy ω_i , the mismatch $E_3 - E_2$ becomes more off-resonant and reduces the efficiency of the 1P absorption. Furthermore, the large 1P Rabi-coupling allows for transferring population back from S_3 to S_2 . The created population in S_3 is therefore lower, than for the negatively chirped pulse and the PL signal strength higher for $\beta > 0 \text{ fs}^2$. This difference in population transfer probability from S_2 to S_3 between $\beta < 0 \text{ fs}^2$ and $\beta > 0 \text{ fs}^2$ gives finally rise to the obtained asymmetry in the measurements.

In analogy to the above made conclusions, the example in Fig.4.11 (b) can be explained. However, the PL trace and also the dynamics show completely opposite behaviour for this molecule, with a higher PL signal for a negatively chirped pulse with $\beta = -240 \text{ fs}^2$. The dynamics of S_3 clearly demonstrate the population transfer $S_2 \rightarrow S_3$ starting almost simultaneously with the 2P absorption process for both values of β , but with significant higher efficiency for $\beta = +240 \text{ fs}^2$. Again this depopulation of S_2 is additionally indicated by the strong decrease of population in the green-blue line for the states $S_1 \& S_2$. Hence, the asymmetry in the data can be figurative analysed with the time-dependent dynamics and furthermore do these graphs clearly demonstrate the strong dependency of the (2+1)-photon transition from the electronic ground state S_0 through S_2 into a highly excited state S_3 on Ω_{1P} , $E_3 - E_2$ and the instant energy ω_i of the excitation.

Conclusions

The measurements on single MeLPPP exposed to a linear chirped pulse excitation scheme proof the first time genuinely active coherent control of single organic molecules embedded in a disordered matrix at room temperature. The combination of a material with strong 2P absorption and high photostability and ultrafast single molecule excitation scheme enable the reliable and reproducible measurement of the phase dependent 2P and (2+1)P absorption response of each individual emitter. The deviation of the obtained results from the well known theoretical description of 2P transition

probability between two states lead to the extension of the model for the ultrafast dynamics of MeLPPP. A fourth highly excited electronic level, which is not accessible via usual spectroscopic techniques, enables a 1P transition from the 2P accessible state and constitutes therefore as loss channel for the detectable PL. However, all single molecule data show a distribution of the optimal parameters found by the QDI procedure. This variety proofs the strong electronic heterogeneity from molecule to molecule embedded in the disordered matrix at room temperature. This fundamental information can not be obtained by measuring only the response of an ensemble sample. The ensemble measurement shown in Fig. 4.8 (a) clearly fails to reproduce especially the asymmetry and therefore the existence of this hidden highly excited state. Note that, although the ensemble trace is perfectly symmetric, the resonance condition of the additional 1P transition between S_2 and S_3 will be fulfilled always for a considerable part of the molecules inside the sample. However, the heterogeneity of the asymmetry (higher PL for $\beta > 0$ fs² and vice versa) and fraction of molecules with a symmetric response will average out this effect and the final results could be naively interpreted as a pure 2P absorption process for the ensemble.

4.4 Conclusion on Coherence Decays and β -dependent Measurements

Both measurements, the decay of the coherence and the phase-dependent 2P absorption, have been performed with similar excitation powers of 2.5 mW and 3 mW, respectively. However, the QDI procedure yields maximum population transfer efficiencies of 20 % for the coherence decay measurements but much bigger values, between 40 % to 80 % for the β -dependent measurement. All obtained decays have been very well reproduced with the simpler 3-level model and a fixed 2P Rabi-coupling Ω_{2P} around 120 cm⁻¹, which is considerably low in comparison with the found values for the asymmetric cases. In contrast to the decay measurements, the asymmetric shaped PL traces in dependency of β required the extension of the model by the hidden highly excited state S_3 and, furthermore, coupling strengths three times higher than for the latter case (about 500 to 600 cm⁻¹ for Ω_{2P} and 150 to 400 cm⁻¹ for Ω_{1P}). As the sample and the experimental conditions were similar between those measurements, this discrepancy suggest, that measuring the pure coherence decay is not sufficient enough to obtain a full set of information for this system.

To corroborate this, in Fig.4.12 four β -dependent measurements (a) and two coherence decays (b) are shown for one and the same MeLPPP molecule. These measurements

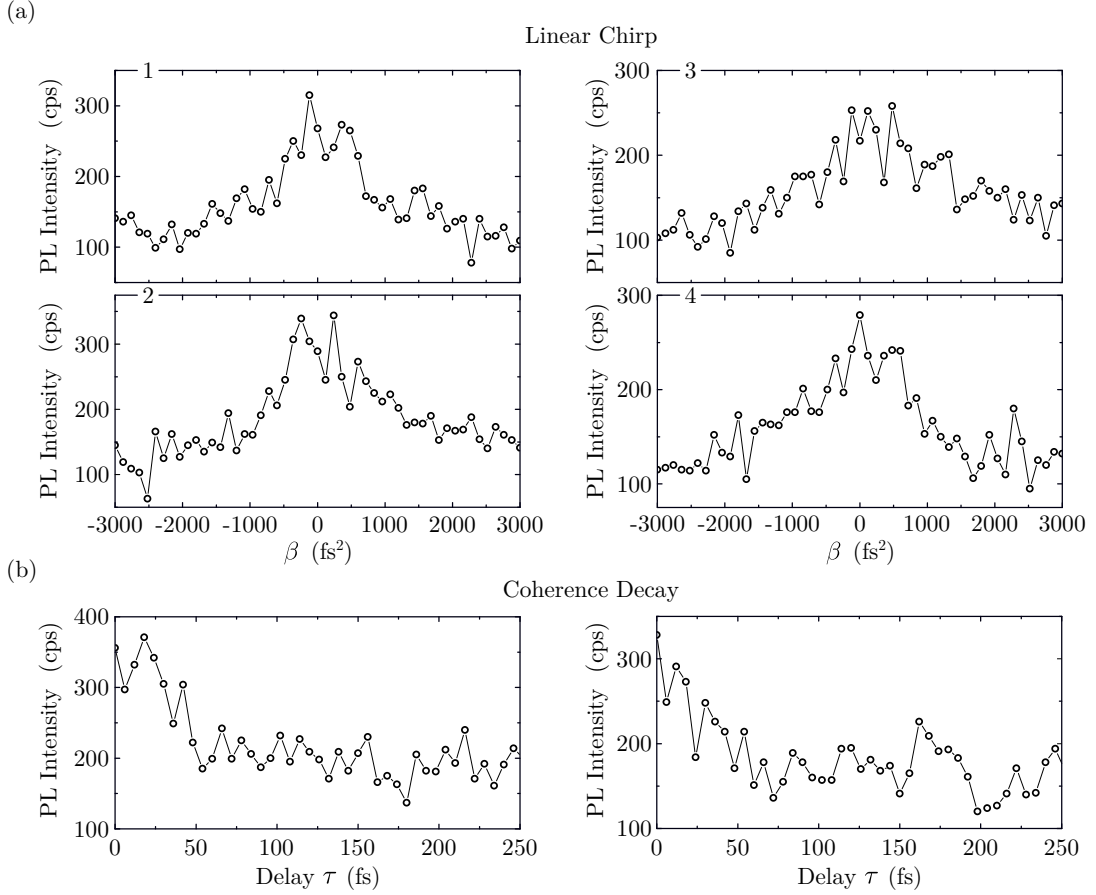


Fig. 4.12: Amplitude and Phase-Shaping Experiments on One Individual Molecule. (a) Four consecutive linear chirp measurements of the β -dependent photoluminescence (PL) of one and the same MeLPPP molecule at room temperature embedded in polystyrene. (b) Two subsequent measurements of the coherence decay envelope of the delay dependent PL of the same molecule shown in (a).

have been carried out consecutively without damaging the molecule with an averaged excitation power of 2.5 mW, measured in front of the excitation objective. As this set of data was taken shortly before finishing this work, the time was not enough to perform the QDI procedure. However, already the raw measurements are enough to illustrate the above assumption. The β -traces show different behaviour between each measurement. Whereas trace 1 follows the asymmetric behaviour, the remaining traces 2, 3 and 4 clearly exhibit asymmetric shaped wings. Furthermore, do these wings differ in their steepness between $\beta < 0$ fs² and $\beta > 0$ fs² from measurement to measurement, indicating the strong dynamical behaviour of the local surrounding and the molecule itself at room temperature.

The decay traces in (b), both, resemble the already known behaviour from section 4.2. The PL signal decreased with increasing delay between both excitation pulses

within the first 50 fs to the incoherent level. The contrast between the signal strength for $\tau \ll 50$ fs and for $\tau \gg 50$ fs is 2, which fits the measurements and theoretical description in 4.2. Although this molecule clearly exhibit asymmetric behaviour in traces 2, 3 and 4 in (a) the coherence decay did not follow any deviations from the simple Bloch-description. Hence, for the system MeLPPP the ultrafast measurement of the coherence decay can yield information about the time dependent dynamics such as the dephasing time γ_2 , the relaxation from S_2 into S_1 Γ_{21} and the energetic landscape, but this still lacks a complete set of parameters describing the quantum mechanical dynamics. It is important to note, that this finding only refers to the system analysed here. In [20] it was proven, that the coherence decay of single terrylene-molecules can also exhibit different shapes, in particular the mentioned contrast, due to different 1P Rabi-couplings between the transition dipole moment and the excitation field. Finally, the combination of the coherence decay and β -dependent measurement enables on one hand the description of the system with a complex model and on the other hand a consistency check for a fraction of the obtained parameters.

To summarize, in the first section of this chapter, the coherence decays have clearly proven the possibility to induce multi-photon transitions in single MeLPPP molecules at room temperature. With the newly developed QDI procedure, this combination is able to retrieve the ultrafast dynamics of a single molecule and its energetic landscape. To get deeper insights into the system this experiment was changed to a phase-only shaping approach, with a quadratic phase function modulated on top of the excitation. The deviation from well-established theory lead to an extension of the former model, which finally yields more complex ultrafast dynamics. With changing the parameters β and therefore the probability to induce the subsequent 1P transition from S_2 into S_3 , this experiment proofs the genuine coherent control of single organic molecule at room temperature. Other ultrafast techniques such as 2D-spectroscopy are able to extract similar parameters about the ultrafast dynamics and energetic landscape. Nonetheless, up to now, this technique lacks to perform these experiments on the single molecule level, which is mandatory to obtain fundamental information about molecules in complex environments. From this point, an interesting approach would be to perform the QDI procedure on the β -dependent measurements on one individual MeLPPP molecule and with the obtained model, to simulate the response to the e.g. double pulse excitation scheme. In such a way one could be able to predict ultrafast responses and quantum dynamical behaviour of single quantum systems with respect to other excitation schemes.

Chapter 5

Ultrafast Processes upon Aggregation in Supramolecular Structures

After the successful characterisation of single organic molecules in complex environments, the question arises, if the experimental setup is capable of extracting information of more complex systems beyond the isolated molecule level. The carbonyl-bridged triarylamine (CBT) derivative with *s*-chiral side chains (complete S-CBT) shows solvent dependent aggregation behaviours ranging from the fully dissolved isolated molecule to single nanofibres and up to bundles of them. In the aggregated form of a nanofibre, S-CBT shows long range energy transfer and therefore provides a perfect and very interesting sample system for investigating the ultrafast and coherent dynamics in its different aggregation states. In the second part of this work, amplitude as well as phase shaping approaches will be exploited to characterise the quantum mechanical probabilities of the generated wave packets in the isolated molecule and the single nanofibre.

5.1 Introduction

Energy transfer is a central aspect in the research field of modern light-energy conversion architectures [126–129]. The prototype model system, many times investigated and cited, is the light harvesting apparatus of, for example, green sulphur bacteria, living in the depth of the sea and taking advantage of the heat radiations of hot smokers [130]. Thereby a photon is absorbed and efficiently transferred by the chromophores built in the light harvesting complex until the energy is further converted by different protein structures inside the membrane of the bacteria. This transfer can be classified into two groups, the incoherent and coherent energy transfer. While the incoherent transfer is dominated by excitonic hopping, which was not found to exceed around 100 nm in its transfer distance [131–133], the coherence is suggested to be responsible for long-range energy transport, which may open the route to sophisticated organic nano photonic

devices. Haedler et al. [29, 94] introduced a new and promising compound, the carbonyl-bridged triarylamine derivative with emissive side-chains. This system assembles to supramolecular nanofibres exhibiting unidirectional long range energy transport at room temperature. This long-range behaviour strongly suggests that coherent effects play a key role in this system. Due to the energy transport from the CBT-core to the emissive side chains, the characteristics of the transport mechanism is hidden. To investigate this transport mechanism of the CBT core the side groups were changed [28] in a way, that the energy transfer into the periphery is not possible any more. Then, the detection of the fibre core's photoluminescence itself enables the investigation of the ultrafast dynamics of the CBT derivative. As described in 3.2 the self-assembly of S-CBT can be controlled via the solvent. Whereas tetrahydrofuran (THF) produces fully dissolved isolated molecule solutions, in n-dodecane single nanofibres and in anisole bundles of these nanofibres emerge. The characterisation of the aggregation state or its quality can be described with the spectral characteristics of the absorption as described in section 2.4. The first step is now to understand the ultrafast dynamics of the compound S-CBT itself. Only then, a comparison to the more complex aggregated form, the single fibre, is possible.

In the first section of this chapter, both coherence decay measurements and phase-only approaches are shown with the isolated S-CBT molecule. Therefore the setup was slightly changed in order to place a glass cuvette in the excitation plane. Three different centre energies of the excitation spectrum give insights into the dynamics of the particular broad exciton band. With the obtained results on the isolated molecule in solution, similar measurements on the single nanofibres in solution can be analysed and compared. Next to the extracted parameters on the ultrafast dynamics, the data suggest a strictly one-photon forbidden, but two-photon allowed state in between the lowest excited singlet state and a higher excited singlet state. The electronic structure of this revealed state seems not to change at all upon aggregation. Furthermore, the ultrafast dynamics of the population generated by non-resonant two-photon absorption are analysed with respect to internal conversion and intersystem crossing processes.

5.2 Experimental

The sample preparation was performed by B. Wittmann (Spektroskopie weicher Materie, Universität Bayreuth). The absorption and PL of S-CBT dissolved in tetrahydrofuran (THF) is again plotted in Fig.5.1 (a) with the chemical structure included. As described in section 2.3, the first excited singlet state of S-CBT is accessible by both, 1P and 2P

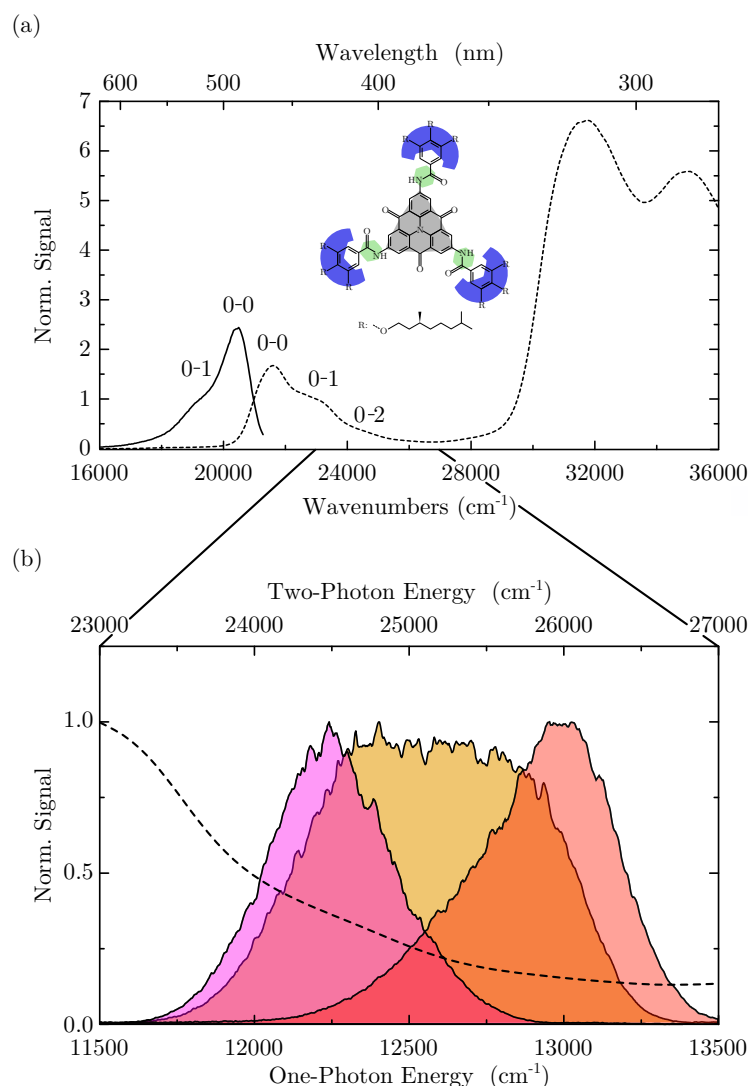


Fig. 5.1: Spectral Characteristics of S-CBT in THF and of the Excitation Source. (a) Normalised (to the particular 0-1 peak) absorption (dashed) and photoluminescence (solid) of the carbonyl-bridged triarylamine (CBT) derivative with s-chiral side chains (S-CBT) in tetrahydrofuran (THF) and chemical structure of the isolated S-CBT in the inset. (b) Three different laser spectra of the Ti:Sa oscillator set to excite the compound at different spectral positions: 12987 cm^{-1} with $\text{FWHM} \approx 500\text{ cm}^{-1}$ (red), 12500 cm^{-1} and $\text{FWHM} \approx 925\text{ cm}^{-1}$ (orange) and 12225 cm^{-1} with $\text{FWHM} \approx 440\text{ cm}^{-1}$ (magenta) in dependency of the one-photon energy and two-photon energy for better comparison with the linear absorption of the sample (dashed line).

absorption processes, which is due to its point group (D_{3h}) symmetry. The transition into the second excited singlet state, denoted with S_2 , is only 2P allowed and thus can not be measured by conventional linear absorption spectrometers. This will be important for the comprehension of the obtained data. The output of the Ti:Sa oscillator

was set between 13000 cm^{-1} and 12000 cm^{-1} , which is in the range of the pulse shapers transmission and the Ti:Sa gain profile and overlaps significantly with the linear absorption of the first electronic state to induce 2P transitions. This was done for three different positions, shown in Fig.5.1 (b), to be more and less resonant with the linear absorption. The linear absorption for energies higher than 24000 cm^{-1} does not decrease down to 0, whose origin is not of further interest here.

As described in Chapter 3 Section 3.3 the excitation/detection unit was changed in order to place in the glass cuvette. The excitation objective has a numerical aperture of $\text{NA} = 0.12$ and the averaged excitation power was set to 6 mW, measured in front of the objective. The compensation mask generating a TL pulse in the excitation/sample plane, is a sum of the pure compensations of the setup without the cuvette, the empty cuvette and the light path through the sample solution up to the excitation plane. The temporal profiles of the TL pulses are given for each spectrum in Fig.3.6 (b),(d) and (f). The modulation patterns are similar to the already shown shaping approaches in Chapter 4, generating a double pulse sequence with phase lock of 0 and delays in 6 fs steps from 0 fs to 300 fs and a linearly chirped pulse and two color double pulse scheme for the phase-only measurements (see Section 3.4 equations 3.4, 3.5, 3.3, 3.6) with β varying between -1000 fs^2 and 1000 fs^2 and a stepsize of 40 fs^2 and τ_{TwoColor} between -200 fs and 200 with a step size of 2π .

5.3 Ultrafast Measurements on the Isolated Molecule in Solution

Results

In Fig.5.2 (a, c, e) three coherence decays of the fully dissolved S-CBT compound in THF are plotted against the delay τ from 0 fs to 300 fs taken at room temperature. Each trace reflects the PL in 10^3 counts per seconds for each laser spectrum (centre energy shown in top left of each graph), with respect to the spectra shown in Fig.5.1 (b) (same color code). In analogy to the MeLPPP experiment, the envelope of the collinear intensity autocorrelation of the particular excitation pulse is given (grey filled area), which decays indeed faster than the probed molecular dynamics. The PL decreases for all three traces within the first 50 fs to the incoherent signal level, with an intensity of about half of the global maximum (contrast of 2). Clear oscillations are visible in the PL dependency after 50 fs. The minima are marked with the particular arrow at positions of 72 fs and 144 fs, 42 fs and 78 fs, and 78 fs and 150 fs. The oscillation periods are $\approx 72\text{ fs}$ (converted to energies 460 cm^{-1}) for the data in (a) and (e) and

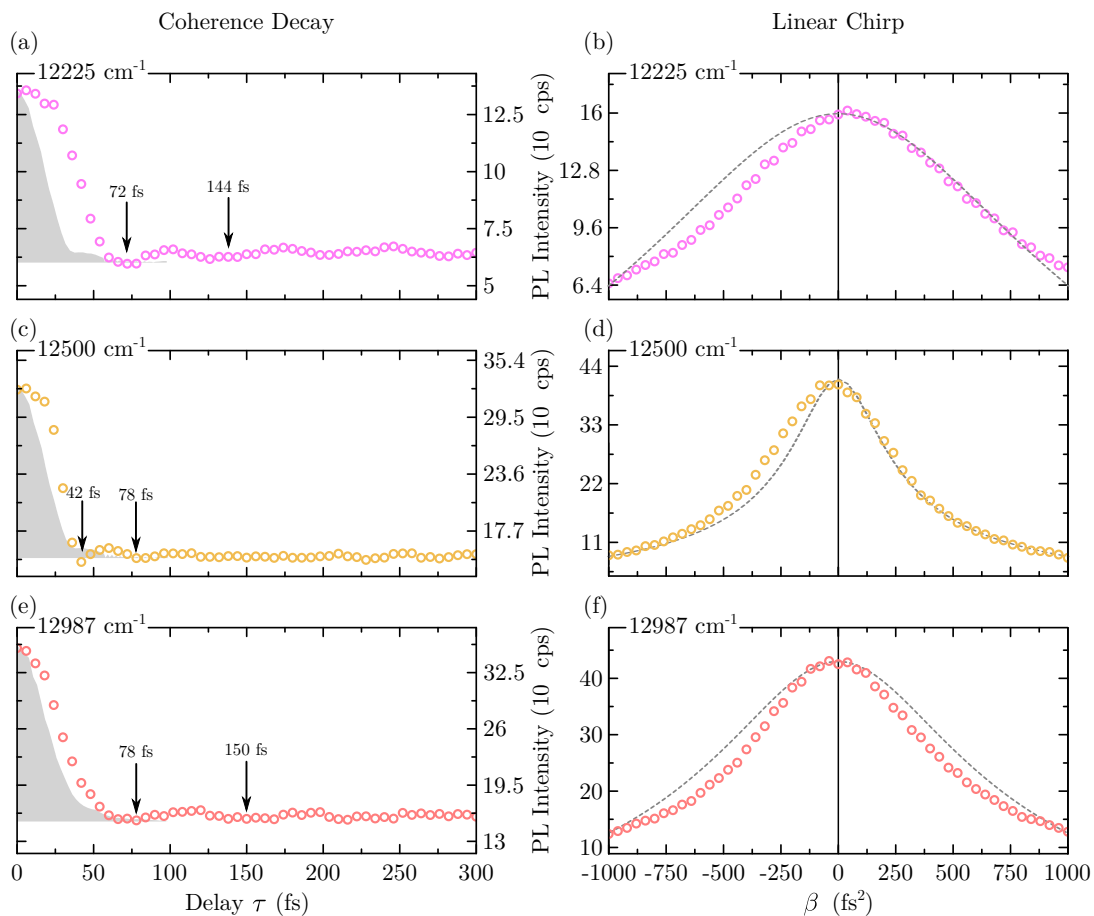


Fig. 5.2: Ultrafast Measurements on S-CBT in THF. (a, c, e) Coherence decay of the photoluminescence (PL) intensity in 10^3 counts per seconds in dependency of the double pulse delay τ (phase difference = 0) for three different central excitation wavelengths (a) 12225 cm^{-1} , (c) 12500 cm^{-1} and (e) 12987 cm^{-1} color coded in analogy to Fig.5.1 (b) of the carbonyl-bridged triarylamine (CBT) derivative with s-chiral side chains (S-CBT) in tetrahydrofuran (THF). The arrows mark particular temporal positions of local minima in the trace and the grey filled area reflect the envelope of the collinear intensity autocorrelation of the excitation pulse. (b, d, f) Phase-only measurements for the same sample and the respective laser spectra for a linear chirp modulation with β varying between -1000 fs^2 and 1000 fs^2 . The black solid line represent 0 fs^2 and the dashed grey lines calculated symmetric signal for each laser spectrum for a pure two-photon transition between two electronic states. The estimated error of the measurements is about ± 150 cps and is smaller than the symbol size.

$\approx 36 \text{ fs}$ (1000 cm^{-1}) for (c). These periodically modulations are more pronounced for an excitation set to 12225 cm^{-1} than for 12500 cm^{-1} and 12987 cm^{-1} , as can be seen from trace (a), with oscillations visible up to a delay of $\tau = 250 \text{ fs}$. Notably, for the same experimental conditions, the PL intensity in (c) and (e) is 3 times bigger than for (a), although the spectral overlap suggested by the linear absorption in Fig. 5.1 (a) is smaller for increasing centre excitation energies.

In Fig.5.2 (b, d, f) the β -dependent measurements for the particular excitation spectrum are plotted. The 0 fs^2 position is marked with the black solid line. For better comparison, a calculated symmetric 2P transition probability signal is drawn as guide to the eye (see Eq.4.1) into the graph. All responses deviate from a perfect symmetric curve, whereas, for an excitation at 12500 cm^{-1} , the curve itself does not exhibit an asymmetric curvature, but more only a shift of the complete trace to negative values. This shift is highly likely due to not fully compensated phase distortion of the laser pulse. The remaining two PL traces do show different curvatures for positive and negative linear chirps, i.e. the PL intensity for $\beta \in [-1000, -0]$ exhibit a steeper increase than for $\beta > 0 \text{ fs}^2$. For a clearer picture, the 1st derivatives of each experimental and simulated curve are given in the Appendix A.6. These systematic deviations from a symmetric curve are considerably bigger than the estimated average error (by photon shot noise $\frac{1}{\sqrt{N}}$ and laser fluctuations of 1% root mean square) of about $\pm 150 \text{ cps}$. In analogy to the coherence decay measurements, the absolute count rate of the linear chirp measurements increases, too. Both measurements in (d) and (f) exhibit a, at least, two times higher maximum intensity than in (b), whereas the spectral overlap with the linear absorption spectrum of S-CBT decreases considerably.

Next to the coherence decay and linear chirp measurements, further experiments on the 2P induced PL in dependency of a phase modulation pattern were recorded. The phase function $\varphi(\omega) = \tau(\omega - \omega_{\text{mod}})$ was only applied to the high energy wing of the excitation spectrum, resulting in two pulses (with different spectral energies), one at 0 fs for the part with zero spectral phase and one delayed by τ . This is a phase locked two color double pulse experiment, as the delay was only varied in steps of 2π between -200 fs and 200 fs . Hence, the sequence of excitation energies is the same for the two color pulse and the linear chirp experiment: negative (positive) values of τ and β reflect higher (lower) energies arriving at the excitation plane first followed by the lower (higher) ones. The only difference is, that in the case of the two color pulse experiment, two transform limited pulses hit the sample, each with equally distributed energies, in contrast to a linear sequence of different excitation energies (for the linear chirp experiment). An exemplary phase is plotted in Fig.5.3 (a) with the lowest energy laser spectrum and the time dependent EM field amplitude of this sequence in (b). The measurement was carried out for all three laser spectra shown in Fig.5.1 (b) and each respective PL response is plotted in Fig.5.3 (c, d, e) in dependency of $\tau \in [-200, 200] \text{ fs}$. Again the PL intensity trace for the excitation at 12225 cm^{-1} and 12987 cm^{-1} slightly suggest asymmetric signals with respect to $\tau = 0 \text{ fs}$, with lower PL for negative delays, in other words, for an excitation scheme with the high energy side hitting first followed

by the low energy side. In contrast, for the excitation centred at 12500 cm^{-1} the PL decay is symmetric around $\tau = 0$ fs.

Additionally to the ultrafast experiments, the spectral shape and thus the electronic origin of the detected PL is to identify. The spectral shape of the PL originating from the first excited singlet state S_1 is determined by the effective vibrational energy $\omega_{\text{eff}} \approx 1260\text{ cm}^{-1}$ and the Huang-Rhys parameter $\lambda^2 = 0.5$. Latter one describes the

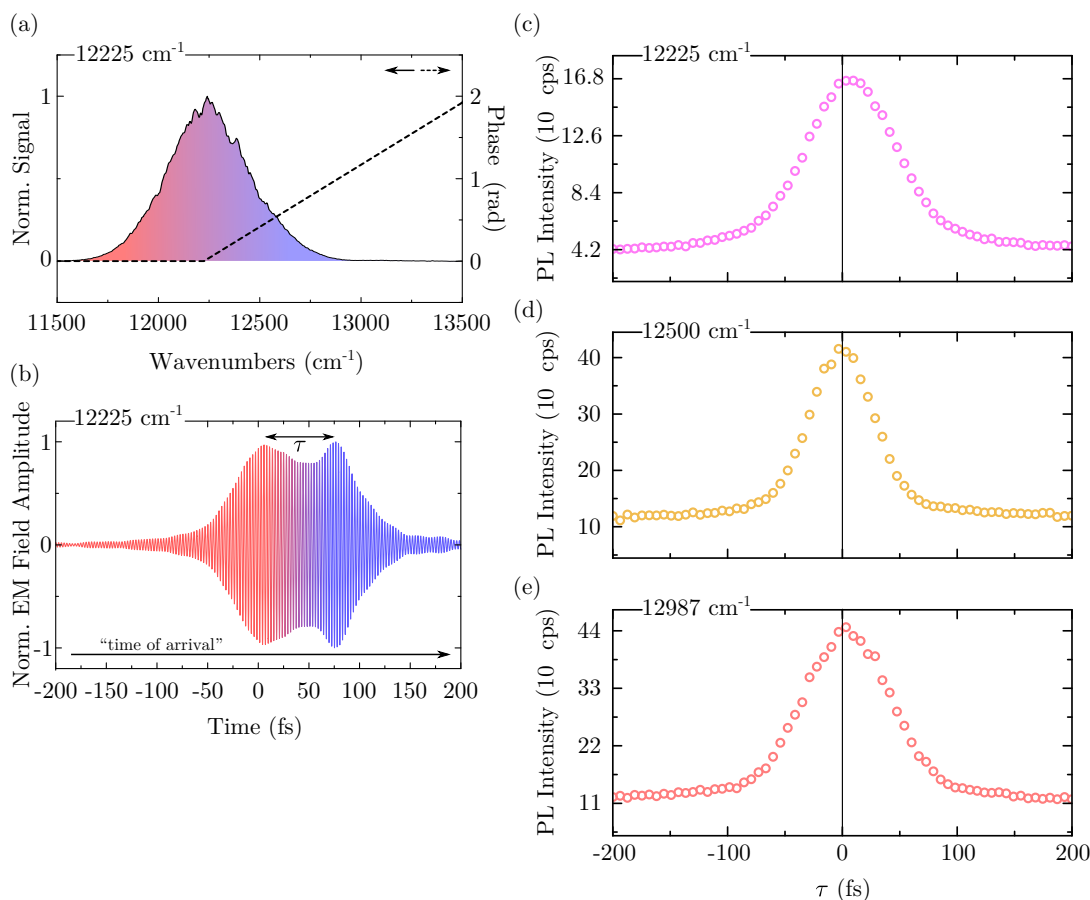


Fig. 5.3: Two Colour Double Pulse Sequence Measurements on S-CBT in THF. (a) Exemplary spectrum centred at 12225 cm^{-1} (solid, filled) with applied linear phase function (dashed) $\varphi(\omega) = 80\text{fs}(\omega - \omega_{\text{mod}})$ (ω_{mod} was set to 12225 cm^{-1}) generating a double pulse sequence with different excitation energies. (b) Fourier transform of the experimental spectrum in (a) with applied phase modulation yields the electro-magnetic (EM) field amplitude in dependency of the time in fs. Colours correspond to the color code in (a), where the high energy side (blue) experiences a delay of $\tau = 80$ fs. The “time of arrival” scale reflects which energies hit the sample first in this case. (c, d, e) Measurement of the photoluminescence of the carbonyl-bridged triarylamine (CBT) derivative with s-chiral side chains (S-CBT) in tetrahydrofuran (THF) for the three excitation spectra given in Fig.5.1 (b) with a delay scan of the high energy side between -200 fs and 200 fs with step size of 2π fs. The estimated error of the measurements is about ± 150 cps and is smaller than the symbol size.

ratio of the 0-1 to the 0-0 peak of the PL. In order to measure the spectral shape of the detected PL intensity in the experiments of this work, narrow transmission bandpass filters are put into the detection path and the excitation stayed constant without any amplitude or phase modulation. The central transmission energy of these bandpass filters are chosen to coincide with the spectral positions of the first excited singlet PL peaks of the 0-0 and 0-1 transition at 20492 cm^{-1} (BP488/10, AHF) and 18796 cm^{-1} (BP532/10, AHF), respectively. The obtained mean count rate (background and detector quantum yield corrected) for the spectral position of the 0-1 peak is 5779 cps and for the 0-0 peak 11292 cps. The ratio of both is 0.51, which is in very good agreement with the ratio of the PL spectrum in Fig. 5.1 (a). Furthermore, measuring the PL signal strength between 24818 cm^{-1} and 23529 cm^{-1} yields an almost vanishing count rate of 800 cps. This signal can be attributed to still not fully suppressed PL of S_1 , as the optical density of the used filter exhibits narrow drops between 18870 cm^{-1} and 16667 cm^{-1} . Taking the ratio of 0.51 and the vanishing PL for higher detection energies into account, the detected PL originates solely from S_1 .

Discussion

The traced PL dependencies in Fig.5.2 (a, c, e) decay within the first 50 fs to an average level, from where no modulation except slight oscillations emerge for larger delays. In analogy to MeLPPP, this dependency reflects the coherence decay of generated electronic and vibronic coherences of each of the accessed state. This coherence decay exhibits a rate of about $\gamma \leq \frac{1}{50}\text{ fs}^{-1}$, which is the effective dephasing rate due to possible relaxations and vibrational transitions. However, the delay-dependent PL oscillations, still evident for $\tau \geq 50\text{ fs}$, suggest that the observed features are due to long living coherence and are indeed intrinsic to the molecular system. This is further corroborated by comparing the PL with the grey filled area, the envelope of the collinear intensity autocorrelation of the laser pulse, which is considerably shorter than the observed PL dynamics. From the PL intensity traces the periods of the oscillations can be determined to 70 fs for (a) and (e), respectively and 36 fs for (c). Translating these oscillations into an energy yields $\Delta \approx 460\text{ cm}^{-1}$ for $E_{\text{exc}} = 12225\text{ cm}^{-1}$ and 12987 cm^{-1} , respectively, and $\Delta \approx 1000\text{ cm}^{-1}$ for $E_{\text{exc}} = 12500\text{ cm}^{-1}$. These oscillations can occur for a detuning from the central transition energy or wave packet interference [21, 70, 134, 135]. The latter option, however, is not very likely, as there is no strong vibronic mode for S-CBT of energies comparable to any Δ . This will be further discussed in the following.

As discussed in Section 2.3 in Chapter 2 the transition from the electronic ground state into the first excited state S_1 is optically allowed, by 1P and 2P transitions. However, the obtained detuning for an excitation of 12225 cm^{-1} does not match the absorption of S_1 . As the excitation nicely overlaps with the 0-2 peak of S_1 and the 0-1 peak is at least 1000 cm^{-1} off-resonant, the delay-dependent oscillations must originate from another transition, which is accessible only via 2P absorption. This is strongly corroborated by the rising 2P induced PL intensity count rate with increasing centre laser frequency, which is in contrast with decreasing spectral overlap with the linear absorption of S_1 (also evident in the β -dependent traces). These findings suggest the existence of a strictly 1P forbidden but 2P allowed electronic state in the spectral range between 24000 cm^{-1} and 28000 cm^{-1} , which is attributed to the second excited state S_2 or denoted with $2^1A'_1$. The increasing value of Δ for excitation energies of 12500 cm^{-1} and decreasing for 12987 cm^{-1} indicates a structured 2P absorption, with at least one vibronic peak, about 460 cm^{-1} off-resonant with the highest energy excitation. Hence, owing to the spectral dependent detunings the 0-0 peak 2P absorption is centred around 24910 cm^{-1} and the first vibronic progression around 26430 cm^{-1} . Furthermore, a Fourier transform of all three coherence decays reveals similar values of the interacting absorption bands, however the small sampling frequency of the experiment does not allow exact indication of this absorption. The difference between both spectral positions, which is one effective vibrational mode, is 1520 cm^{-1} . Considering the temporal resolution, this value fits nicely to an optimised Franck-Condon-progression to PL spectra of S_1 , which yields $\omega_{\text{vib}} = 1263 \text{ cm}^{-1}$.

Next to the clear detuning values, the increasing PL count rate with higher laser energies could originate from two options: (i) due to alternating quantum mechanical symmetry selection rules between the vibronic levels in S_2 , the transition into each of them can be strongly or weakly forbidden, by what the generated population varies; (ii) the structured 2P absorption of S_2 exhibits a Huang-Rhys parameter > 1 , and therefore increasing overlap for higher laser energies.

The first option requires different symmetries between the pure electronic state of S_2 and its vibronic progression. It is already known, that S_2 is of even symmetry (see Section 2.3) and analogue to [53] this yields

$$\begin{aligned} \Gamma(\psi_f) \times \Gamma(\nu_f) \times \Gamma(\hat{\mathbf{p}}_{x,y}) \times \Gamma(\psi_j) &\stackrel{!}{=} A' \\ A'_1 \times \Gamma(\nu_f) \times A'_1 \times A' &= A' \\ \rightarrow \Gamma(\nu_f) &= A' \quad , \end{aligned} \tag{5.1}$$

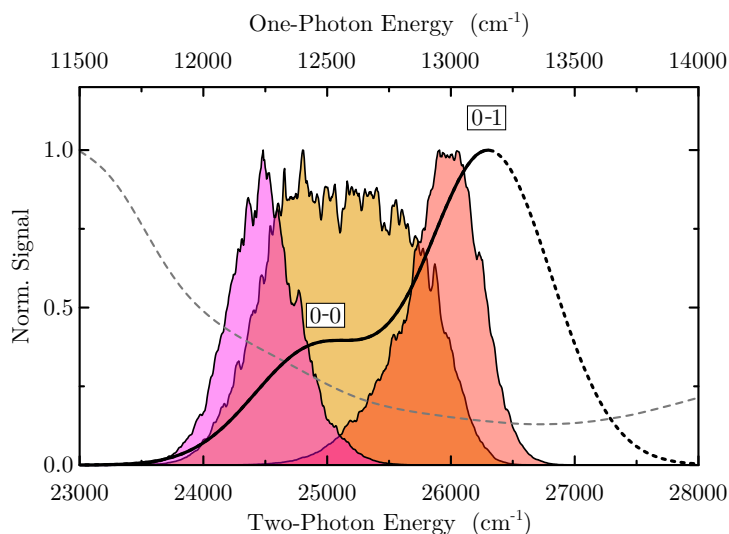


Fig. 5.4: Two-Photon Absorption of S-CBT in THF. All three laser spectra used for the experiment centred at 12987 cm^{-1} (red), 12500 cm^{-1} (orange) and 12225 cm^{-1} (magenta) in dependency of the one-photon and two-photon energy and the linear absorption spectrum (grey dashed). The black line reflects an approximation of the two-photon state based on the coherence decay results with one pure electronic absorption (0-0) and one vibronic (0-1) of the carbonyl-bridged triarylamine (CBT) derivative with s-chiral side chains (S-CBT) in tetrahydrofuran (THF). The spectrum was calculated according a Franck-Condon progression starting at 24909 cm^{-1} with an effective vibrational energy of 1400 cm^{-1} , standard deviation $\sigma = 708\text{ cm}^{-1}$ and Huang-Rhys factor of 2.7 to fit the distinct PL intensities of the measurements in Fig.5.2. The dashed break reflects the fact that the data measured can not give any further information about absorptive features at spectral positions higher than the 0-1 peak.

where $\Gamma(X)$ reflects the symmetry species of X , $\psi_{f,j}$ are the final and initial pure electronic states and ν_f is the final vibrational state. With the condition, that the result must be of even symmetry, the considerations yield, that the pure electronic state in S_2 and all its vibronic levels exhibit the same even symmetry. Hence, each of the transitions into the vibronic levels of S_2 is symmetrically allowed and the increasing PL signal is due to a Huang-Rhys parameter > 1 rather than due to symmetry selection rules. Under the assumption that the detected PL intensity is proportional to the population transfer into S_2 , a calculated Franck-Condon progression gives an estimate about this hidden 2P allowed absorption. The values were chosen to fit at first the tendency of the PL intensity increase, with the data for an excitation at 12500 cm^{-1} and 12987 cm^{-1} to be almost 3 times higher than for $E_{\text{exc}} = 12225\text{ cm}^{-1}$. Another criterion to check, whether this suggested absorption reflects the reality, is the shape of the coherence decay and the period of the oscillations. This final spectrum is shown in Fig.5.4 in comparison to all laser spectra. The values of the Franck-Condon progression are given in Table 5.1. These values were chosen to be not completely different from

	E_0 (cm ⁻¹)	ω_{vib} (cm ⁻¹)	σ_1 (cm ⁻¹)	σ_2 (cm ⁻¹)	λ^2
S ₁	21502	1263	709	993	0.48
S ₂	24910	1400	709	709	2.7

Tab. 5.1: Franck-Condon Progression of S₁ and S₂. Obtained fit parameters for S₁ (first row) and used calculation parameters for S₂ (second row) of the Franck-Condon progression: 0-0 transition energy E_0 , effective vibronic coupling mode ω_{vib} , standard deviations of the 0-0 and 0-1 peaks σ_1 and σ_2 , respectively, the Huang-Rhys parameter S .

the parameters describing the absorption of the first excited singlet state S₁, with equal widths of the absorption bands. The dashed break reflects the fact, that no information was experimentally extracted for energies above 26300 cm⁻¹ and hence the absorption is undefined in that spectral range. Finally, the induced transition is a strictly 2P allowed transition between the electronic ground state S₀ and the second excited singlet state S₂, but as seen in the last paragraph in the results section, the PL intensity solely stems from S₁. In other words, after the population transfer into S₂ vibrational relaxation and internal conversion processes lead to a fast and efficient population of the lowest vibronic state in S₁ from where radiative deactivation leads to the PL signal. Furthermore, the generated coherence for the laser spectra at 12225 cm⁻¹ and 12987 cm⁻¹ is purely electronic. The excitation with the broad spectrum at 12500 cm⁻¹ may induce vibronic coherence. However, as discussed in the beginning, the oscillation energy of 1000 cm⁻¹ could only be ascribed to a very weak vibrational mode [28], and the oscillation for the laser spectra centred at 12500 cm⁻¹ is highly like to reflect only detuning.

In analogy to MeLPPP, the asymmetry of the linear chirp and two-color pulse sequence measurements suggests processes which go beyond the pure 2P absorption between the ground state S₀ and the only 2P allowed state S₂. Nevertheless, the yet unknown process effects the ensemble PL response, indicating the same strong nature among a majority of molecules inside the excitation volume. In the following, several approaches will be discussed in order to give an explanation of the asymmetry. A first interpretation could be, the (2+1)-photon process between S₀, S₂ and a high lying electronic state, while the latter state has small or even vanishing PL quantum yield, similar to MeLPPP. The linear absorption spectrum in Fig.5.1 (a) contains a strong absorbing signal starting at 30000 cm⁻¹ and is denoted with S_{*n*}. Fluorescence spectroscopy of this high lying electronic state reveals, that all detectable PL upon excitation at 35088 cm⁻¹ stems mainly from S₁ (see Appendix Section A.7). PL signals at higher energies were not obtained, indicating that a considerable fraction of the generated population in S_{*n*} is transferred via IC to S₁ from where emission occurs. However, on one hand the energetic mismatch between the second excited state S₂ and

the high lying electronic state S_n of about 8000 cm^{-1} is too small, and on the other hand the spectral width of S_n is too big to exclude optical transitions whether they are induced with the high or low energy side of the particular excitation spectrum. Hence, a (2+1)-photon transition can be neglected at this point to be the origin of the asymmetric shape.

Another option leading to the asymmetric shapes could be the linear chirp dependency of stimulated emission (SE) of one photon (1P-SE), which was already found for dyes in solution by the Dantus group [136]. However, the process analysed in this publication, was a pump-dump process taking place in a 4-level system with 1P transitions instead of 2P processes. The measurement here was carried out with two BG39 glass filters in detection, which allow transmission between 28571 cm^{-1} and 16667 cm^{-1} .

If the SE takes place via emission of one photon, spectral distinction between the PL from state S_1 and 1P-SE from the same state, which is of similar energies, is not acquired. In addition, as mentioned above, no considerable signal was found in the spectral range around double the excitation energy, which would indicate SE. Hence, a loss or enhancement, due to increased 1P-SE can not be the source of the asymmetry in this particular experiment. In contrast, publications have proven the significantly strong effect of simultaneous SE of two photons (2P-SE) of dye molecules in solution [137, 138] (see Fig.5.6 left panel). Then, both photons, are of same energies as the excitation. In this work the experiment is designed to sufficiently suppress the excitation and consequently 2P-SE, too. Finally this would result in a sufficient decrease of the detected PL signal and lead to an asymmetric shape of the linear chirp dependent trace.

Reports on the control over energy flow and internal conversion processes with phase function approaches opens the path to a last option to analyse the asymmetric traces. A generated wave packet and its motion along the potential energy surface is, dependent on the chirp, less or more likely to cross conical intersections between two electronic states [139, 140]. The linear absorption spectrum of S-CBT exhibits a pronounced vibronic progression reflecting the existence of high lying vibrational states of the first excited state, which considerably overlap in their energy with the excitation in S_2 . Hence, the control of IC between the second excited and the first excited state is likely. If the excitation probability in S_2 is not transferred into S_1 , the only possible mechanisms to depopulate that state, would be a radiative decay straight from S_2 into S_0 or IC into an extremely high lying vibrational state of S_0 . The former one can be easily excluded because of two facts: (i) the BG39 filters would not block the PL and therefore no asymmetry would be obtained and (ii) the 1P transition from S_2 into S_0 does not take place at all, as it is symmetry forbidden. The non-radiative transition from S_2 into S_0 is unlikely as well. This would involve as a first step an iso-energetic IC from S_2 into a

highly excited vibrational state of the ground state. Transitions into these states are possible, however, according to the energy gap law the probabilities are vanishing low [16]. Hence, if only the states S_1 and S_2 are considered, the excitation generated in S_2 will finally end up in S_1 and control of IC between those states won't generate any asymmetric PL intensities for different linear chirps in this experiment. The coherent control of IC between S_2 and S_1 can be neglected as source of the asymmetric shapes.

But, the existence of a triplet state, which is efficiently populated, and the coherent control of the transition $S_n \rightarrow T_n$ could give rise to the obtained asymmetric shapes of the β -dependent PL intensities. The low PL quantum yield of S-CBT, which is around 15% in solution [29], hints towards the efficient population of non-radiative states. This state was finally identified with a triplet by time-resolved electron parametric resonance (EPR) measurements, done by Dr. Till Biskup (Albert-Ludwig-Universität Freiburg) [141]. Further flash photolysis measurements performed by Wittmann of S-CBT in THF revealed excited state absorptions from this triplet state [76]. The transient absorption spectra are presented in Fig.5.5 at four different times (8 ns, 63 ns, 203 ns, 403 ns) after the excitation of the pump pulse at 22222 cm^{-1} . The temporal resolution is given by the electronics of the flash photolysis setup and is about 5 ns. Positive ΔOD values reflect real absorption effects, which are created in consequence of the pump excitation, whereas negative values are ascribed to PL or SE. Although the transient absorption spectra in Fig.5.5 exhibit predominant negative ΔOD values, these are only existent for very short delays and hence represent PL and SE. More important, strong positive ΔOD signals are obtained around 11000 cm^{-1} and 18000 cm^{-1} (for delays $\gg 10 \text{ ns}$) indicating further absorption after the system was pumped at 22222 cm^{-1} . Both positive ΔOD bands still exist for very long delays and can therefore be ascribed to an excited state absorption, from the triplet state T_1 into another higher excited triplet states. Cutting the signal at 10309 cm^{-1} and plotting against the delay time, yields a decay consisting of a populating and depopulating component (see Appendix Section A.8 and Fig. A.8). The population rate is denoted with k_{ST} as it describes the ISC from the pumped S_1 into T_1 and the depopulation with k_T , which includes all transition rates from T_1 . By separating the transient into a rising component between $0 \text{ }\mu\text{s}$ and $0.12 \text{ }\mu\text{s}$ and a decreasing one from $0.12 \text{ }\mu\text{s}$ up to $4.5 \text{ }\mu\text{s}$ and further single exponential fitting of both regions the routine yields $k_{ST} = 0.07 \text{ ns}^{-1}$ and $k_T = 0.0011 \text{ ns}^{-1}$. Including the temporal resolution of 5 ns and the width of the pump pulse between 5 ns to 8 ns [142] the found dynamics are in agreement with the values presented in [76], where calculations on the radiative lifetime of S_1 and the respective PL quantum yield result in non-radiative depopulation rate of S_1 of about $k_{ST} = 0.304 \text{ ns}^{-1}$. This

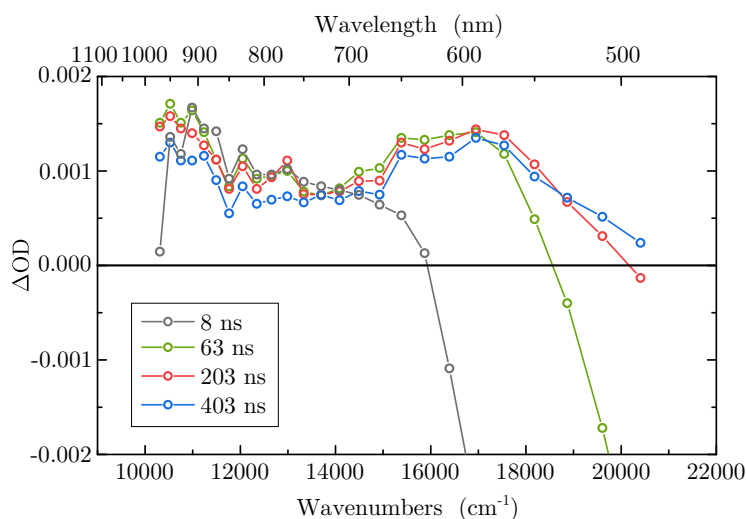


Fig. 5.5: Nanosecond Transient Absorption Spectra of S-CBT in THF. Transient absorption spectra of carbonyl-bridged triarylamine (CBT) derivative with *s*-chiral side chains (S-CBT) in tetrahydrofuran (THF) for four different delays between the pump at 22222 cm^{-1} and the respective probe pulse. The horizontal black line represents $\Delta\text{OD} = 0$. Data was taken with permission of B. Wittmann and further processed for display [76].

fast population of T_1 is also reflected by the instantaneous¹ arising positive ΔOD signal for energies below 12000 cm^{-1} . Finally, both positive ΔOD signals arise within similar time scales and represent therefore the triplet-triplet absorption from T_1 into two higher excited triplet states T_2 and T_n (with $n \geq 3$). Furthermore, A. Köhler and B. Beljonne analysed experimentally and theoretically the exchange energy² ΔE_{ST} of a variety of aromatic compounds [143]. The results suggest that ΔE_{ST} is almost constant over for a large number of analysed aromatic compounds and is close to 0.7 eV , which is 5645 cm^{-1} . Note that this is only a rough estimate, as the publication describes only the exchange energy of conjugated polymers. Subsequently, the energy of T_1 is about 5645 cm^{-1} lower than S_1 , with 15857 cm^{-1} . With the triplet-triplet absorption from the transient spectra located at 10000 cm^{-1} the energy of the nearest higher excited triplet state is 25857 cm^{-1} . This strongly overlaps with the 2P allowed spectra found before between 24000 cm^{-1} and 27000 cm^{-1} . Finally, the existence of T_2 opens up the path for control of the intersystem crossing (ISC) rate between S_2 and T_2 . This, in turn, leads to a linear chirp dependent PL intensity and results in an asymmetry for a scan of β , as shown in Fig.5.2 (b), (d) and (f) and Fig.5.3 (c), (d), and (e). For further support, quantum mechanical calculations give a rough estimate of the shape of the wave function in the excited state. Using a 3-level model, with one level in the

¹Instantaneous within the temporal resolution of 5 ns

²The exchange energy describes the energy gap between the lowest excited singlet and triplet states.

ground state and two in the excited state (for the 0-0 and the 0-1 transitions), the results lack a difference between positively and negatively chirped excitation pulses for the generated wave packets. Therefore low-energy skeletal modes are taken into account. These modes are usually in the low energy wing of each absorption band, and are covered by the inhomogeneously broadened band. With only 2 skeletal modes for each vibronic C-C stretching modes the generated wave packets for laser spectra at 12225 and 12987 cm^{-1} differ between $\beta > 0 \text{ fs}^2$ and $< 0 \text{ fs}^2$, whereas the wave packets for the laser centred at 12500 cm^{-1} completely resemble each other. This nicely reflects the asymmetric behaviours found for each excitation spectrum (see Appendix A.9). Again, note that asymmetry means the different strong crooked curvature of the PL intensity trace for positive and negative values of β , and not the constant shift of the curve to positive or negative values of β . Latter one is highly likely due to a not perfect compensation of the pulse, as the exact light path through the sample volume in the cuvette is difficult to determine. As a longer or shorter actual light path through a dielectric medium affects mostly the second order phase this deviation will be reflected by a constant additive factor in fs^2 .

Including the preceding results, the complete process taking place can be characterised. After a 2P absorption into the only 2P allowed state S_2 the population relaxes via IC, vibrational relaxation into the first excited singlet state S_1 and a fraction via ISC into the triplet state S_1 . The latter process exhibits a dependence on the generated wave packet shape in S_2 and therefore the coherent control via phase shaping approaches can vary the population transfer into T_1 which is finally reflected by the detected PL intensity from S_1 .

Conclusion

Different ultrafast two-photon (2P) absorption measurements, ranging from simultaneous amplitude and phase shaping up to phase-only approaches were performed on the S-CBT derivative dissolved in THF. In this solvent S-CBT appears completely molecularly dissolved. The PL intensity was detected in dependency of the double pulse delay τ , for the pair of identical pulses and the two-color sequence, and the linear chirp parameter β . All measurements have in common the increasing PL intensity signal with the excitation spectrum being tuned from low to higher energies. This is in contrast to the spectral overlap suggested by the linear absorption spectrum of S-CBT in solution. In the spectral range of the induced 2P transitions, the linear absorption significantly decreases with higher energies. Hence, an increasing PL intensity can not be due to absorption taking place between the electronic ground state S_0 and the lowest excited

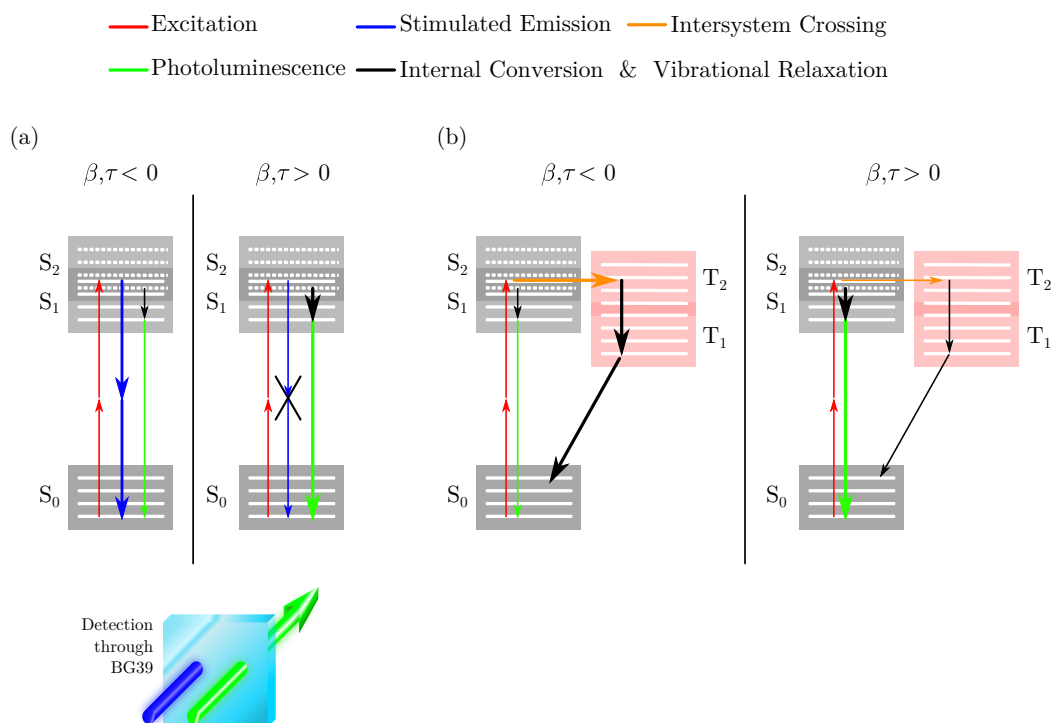


Fig. 5.6: Processes Leading to an Asymmetric Behaviour. Stimulated emission (SE) and intersystem crossing rates for the carbonyl-bridged triarylamine (CBT) derivative with *s*-chiral side chains (S-CBT) in tetrahydrofuran, in dependency of the sequence of the instantaneous excitation frequency. β or τ -values smaller (bigger) 0 represent a decreasing (increasing) instantaneous excitation energy with time. The thickness of the arrows reflect the efficiency of the respective process: thick (thin) arrows represent a process which is more (less) likely to happen. **(a)** Stimulated emission (SE) of two photons (2P) upon 2P absorption into the second excited state S_2 . The process is more likely to take place for negative values of β than for positive ones. The sketch below reflects block and transmission of the SE and the photoluminescence (PL), respectively. **(b)** Intersystem crossing (ISC) from the second excited state S_2 into the second excited triplet state T_2 . The ISC rate is bigger (orange thick arrow) for $\beta, \tau < 0$, which results in a smaller PL (thin green arrow).

singlet state S_1 . This leads to the results on the existence of a strictly 2P allowed state, which is not accessible via conventional absorption spectrometers, as shown in Fig.5.4. Non-resonant 2P excitation in the selected spectral range generates population in an only 2P allowed state denoted with S_2 . Subsequent vibrational relaxations and internal conversions lead to population transfer into S_1 , from where the detected PL signal originates.

The next addressed problem was the asymmetry in the β -dependent traces as well as the two-color pulse experiments. Several approaches were presented which could lead to an asymmetric behaviour of the population and therefore for the PL intensities. Possible options such as the excited state absorption from S_1 or S_2 into a highly excited

state S_n at 30000 cm^{-1} , the stimulated emission of one photon and the PL from S_2 can be excluded. On the one hand, the absorption width of the state S_n is large. Selectivity of the transition $S_{1,2} \rightarrow S_n$ due to the instantaneous excitation energies of the chirped pulses is not achieved. On the other hand, the used detection filters will not block the SE or the PL from S_2 as both types of radiation lie perfectly in between the transmission profile. Finally, only two options of the underlying mechanism remain, which lead to a β - and τ -dependent (two-color pulse experiment) signal asymmetry. Both processes are schematically presented in Fig.5.6: in (a), the SE of two photons at the same time and in (b) the intersystem crossing between S_2 and T_2 . For β and $\tau < 0$ the SE may be more efficient than for positive values. The more excitation probability is deactivated via simultaneous SE of two photons the more detectable signal is lost due to the spectral dependent transmission of the detection filters. Hence, for stronger SE, less PL signal is expected, reflected by asymmetric shapes of the detected signal. The energy diagram in (b) describes the β and τ -dependent intersystem crossing rates. A negative linear chirp could enhance the intersystem crossing rates from the 2P allowed state S_2 into the strong energetically overlapping triplet T_2 . Population transferred into T_2 is efficiently non-radiatively deactivated and finally does not add up to the detectable signal. This would also result in an anomalous behaviour of the chirp and delay dependency of the PL intensity signal.

Overall, both processes could give rise to the asymmetry found in Fig.5.2 and Fig.5.3. But, up to now, there is no further information about two-photon induced SE of two photons and the efficiency of this process for S-CBT. In contrast, the second considered option is strongly corroborated by the intersystem crossing rates found for the first excited state, the energetically overlapping second excited triplet state T_2 with the 2P addressed state S_2 and furthermore the calculations of the shape of the generated wave packets in the excited singlet state. Comparing both processes, the existing information strongly suggest the β - and τ -dependent intersystem crossing probabilities to be the origin of the found asymmetries.

5.4 Ultrafast Measurements on Single Nanofibres in Solution

Changing the solvent, from THF to n-dodecane (DOD) opens up the path to aggregation. S-CBT forms supramolecular nanostructures for different solvents, ranging from nanofibres to fibre bundles. In the case of DOD, single nanofibres with lengths up to several microns are formed [141]. The inset in Fig.5.7 (a) demonstrates the spatial

structure of the S-CBT in its H-aggregated form of the nanofibre. The packing distance of 3.3 Å between the single building blocks is defined by $\pi - \pi$ -interaction.

Results

For better comparison with the spectral positions of the three laser spectra, the linear absorption and PL spectrum of S-CBT dissolved in DOD at room temperature is shown again in Fig.5.7 (a). In (b) the same excitation spectra, as already shown in Section 5.3 Fig.5.1 (b) are plotted against the 1P and 2P energies. The absorption and PL spectra were normalised to the first vibronic exciton band, for reasons of clarity denoted with 0-1. As discussed in Section 2.4, for the absorption the ratio between the 0-0 exciton band and the 0-1 band decreases as the oscillator strength is mainly concentrated in the upper edge of each exciton band compared to the isolated S-CBT molecule. The 0-0 transition in the emission spectrum, however, has completely vanished, as it is forbidden from the lower edge of the exciton band by reasons of symmetry selection rules. Furthermore absorption strength has risen compared to the isolated molecules absorption in Fig.5.1 in the spectral range of doubled the excitation energies between 24000 cm^{-1} and 30000 cm^{-1} .

In analogy to S-CBT dissolved in THF, coherence decays, linear chirps and two-color double pulse measurements were carried out on single nanofibres³ in DOD and are presented in the following. Figure 5.8 shows the coherence decay measurements on S-CBT in DOD (a, c, e) and the phase-only measurement in (b, d, f). In contrast to the THF measurements the average counts are comparable low, ranging for all three excitation positions between 1000 and 7000 cps. The PL intensity increases with higher excitation energies, whereas the counts in (c) and (e) are pretty similar. The count rate for the coherence decay measurements decreases within the first 100 fs, but still exhibiting oscillations for values of τ bigger than 100 fs. The contrast between the PL intensity for $\tau \ll 100$ fs and $\gg 100$ fs is 2 for all three measurements. The oscillations are most prominent for the highest energy excitation at 12987 cm^{-1} with a period of approximately 72 fs. For the middle excitation this periodically modulation is much faster with $T = 42$ fs, whereas for 12225 cm^{-1} the oscillations ($T = 72$ fs) are not as clear as for S-CBT in THF (best evident between 50 fs and 125 fs). For comparison with the pulse envelope, the collinear intensity autocorrelation envelope is plotted against the delay, reflected by the grey filled area. The PL intensity dynamics are clearly slower than the decay of the autocorrelation. In the right panel of Fig.5.8 the measurement of the PL in dependency of the linear chirp parameter β is shown, varied between

³single refers to the nanofibre in solution without any higher dimensionality, e. g. bundles of nanofibres

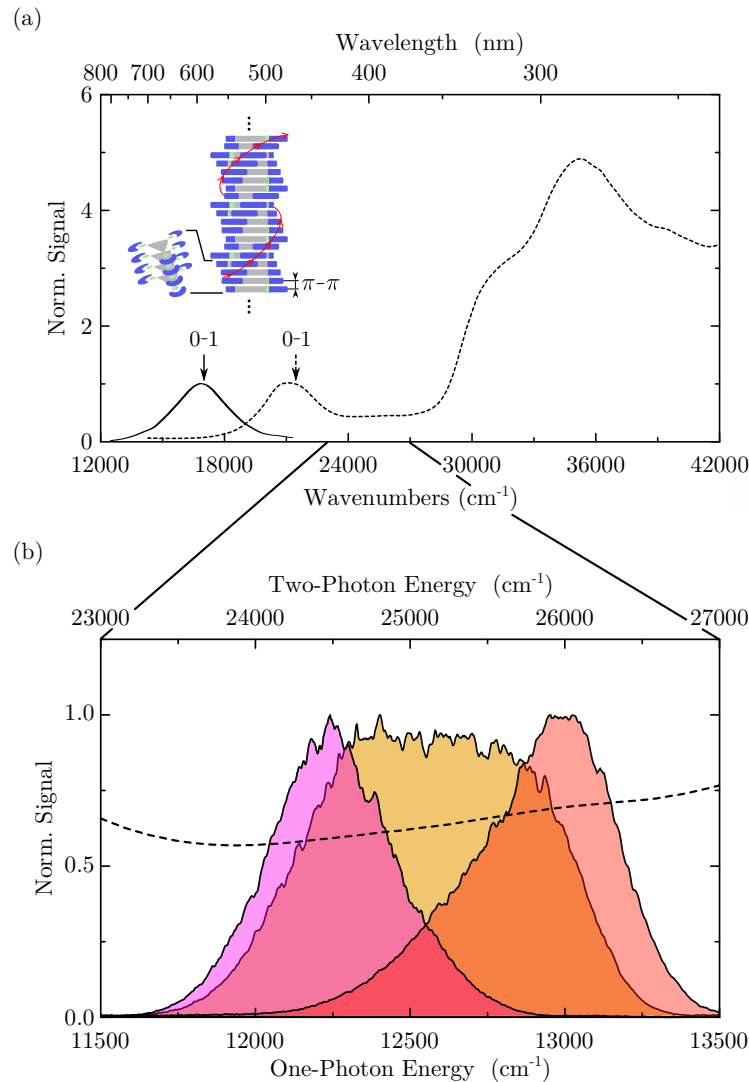


Fig. 5.7: Spectral Characteristics of S-CBT in DOD and Laser. (a) Normalised (to the spectral position of the first vibronic band) absorption (dashed) and photoluminescence (solid) of the carbonyl-bridged triarylamine (CBT) derivative with s-chiral side chains (S-CBT) in n-dodecane (DOD) and spatial structure of the nanofibre in the inset. (b) Three different excitation spectra of the Ti:Sa oscillator set to excite S-CBT at different spectral positions: 12987 cm^{-1} with $\text{FWHM} \approx 500 \text{ cm}^{-1}$ (red), 12500 cm^{-1} and $\text{FWHM} \approx 925 \text{ cm}^{-1}$ (orange) and 12225 cm^{-1} with $\text{FWHM} \approx 440 \text{ cm}^{-1}$ (magenta) in dependency of the one-photon energy and two-photon energy for better comparison with the linear absorption of the sample (dashed line).

-1000 fs^2 and 1000 fs^2 . For comparison with a symmetric curve centred at 0 fs^2 , the grey dashed lines serve as guide to the eye. The PL intensity in (b) exhibits a slight asymmetry with a stronger curvature of the trace for $\beta < 0 \text{ fs}^2$. Whereas the asymmetry in (f) is less pronounced but still exhibits a slight stronger curvature for $\beta < 0 \text{ fs}^2$,

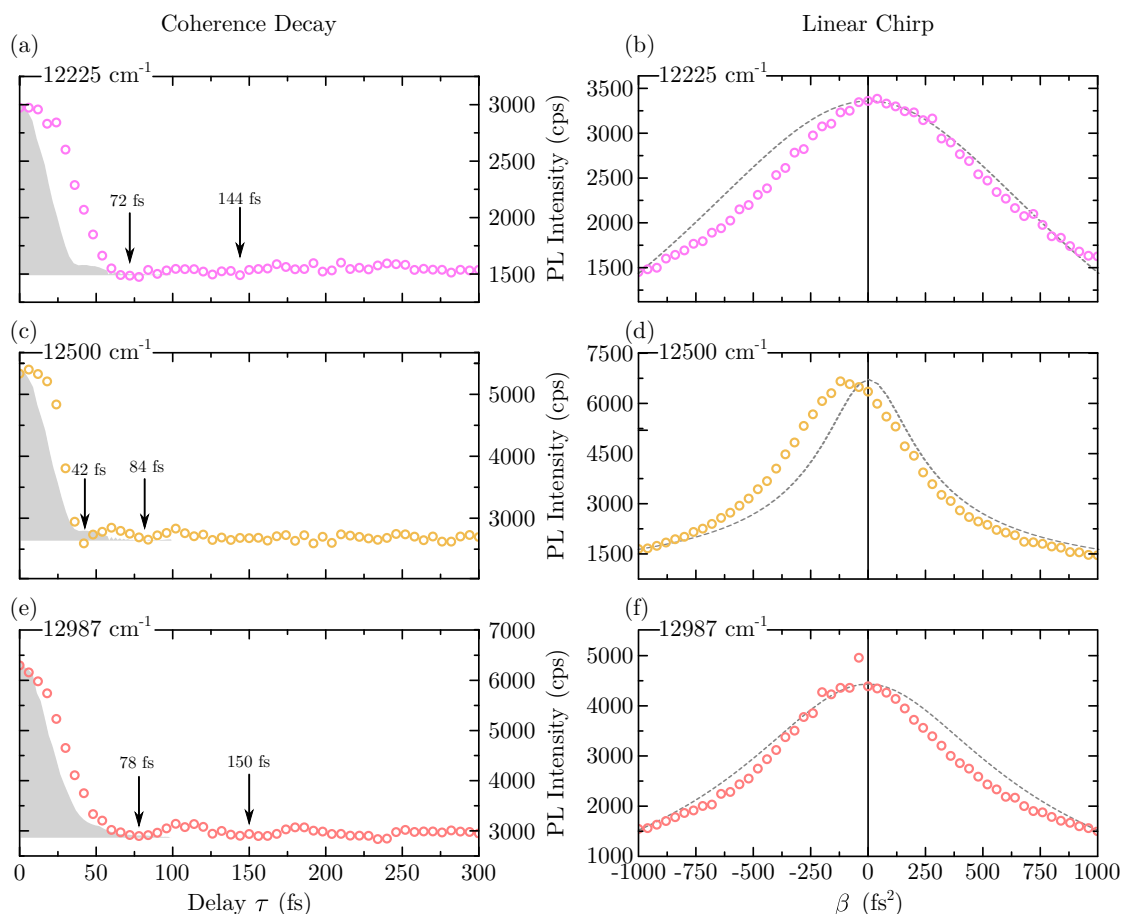


Fig. 5.8: Ultrafast Measurements on S-CBT in DOD. (a, c, e) Photoluminescence (PL) detected coherence decay envelopes of the excited state in counts per seconds in dependency of the double pulse delay τ (phase difference = 0) for three different central excitation wavelengths (a) 12225 cm^{-1} , (c) 12500 cm^{-1} and (e) 12987 cm^{-1} color coded in analogy to Fig.5.1 (b) of the carbonyl-bridged triarylamine (CBT) derivative with s-chiral side chains (S-CBT) in n-dodecane (DOD). The arrows mark particular temporal positions of local minima in the trace and the grey filled area reflects the collinear intensity autocorrelation envelope of the laser pulse. (b, d, f) Phase-only measurements for the same sample and the respective laser spectra for a linear chirp modulation with β varying between -1000 fs^2 and 1000 fs^2 . The black solid line represent 0 fs^2 and the dashed grey lines are a guide-to-the-eye for comparison to symmetrical signals.

with an additional shift to $\beta < 0\text{ fs}^2$, the curve in the middle panel is symmetric in its shape but considerably shifted with the maximum around $\beta = -90\text{ fs}^2$. These findings are in agreement with the results for S-CBT dissolved in THF. Furthermore, tuning the excitation center from 12225 cm^{-1} to 12500 cm^{-1} increases the PL intensity considerably. However, in contrast to the change from (c) to (e) the counts decrease again between (d) and (f).

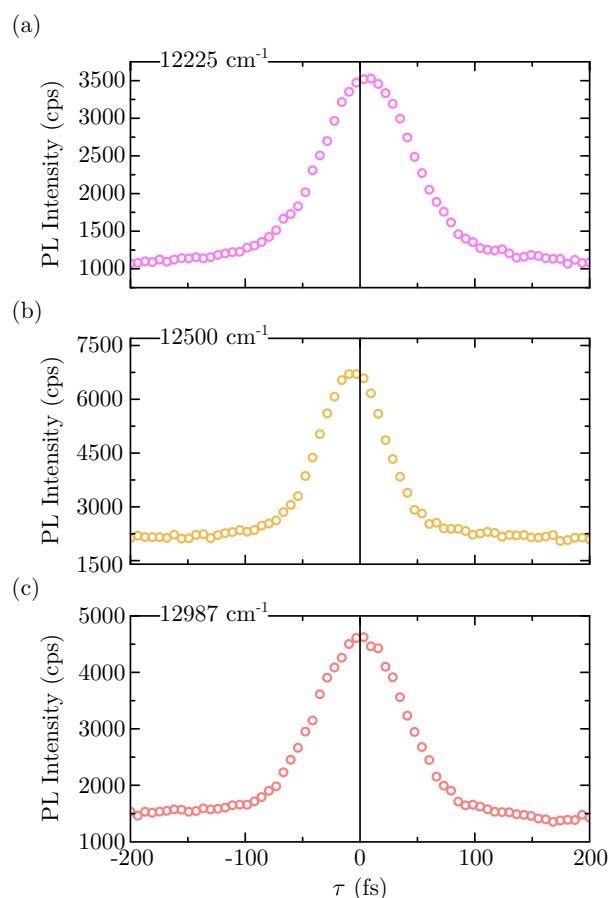


Fig. 5.9: Two Color Double Pulse Excitation Measurements on S-CBT in DOD. (a, b, c) Measurement of the photoluminescence intensity of the carbonyl-bridged triarylamine (CBT) derivative with *s*-chiral side chains (S-CBT) in *n*-dodecane (DOD) for the three excitation spectra given in Fig.5.1 (b) with a delay scan of the high energy side between -200 fs and 200 fs with step size of 2π fs.

Fig.5.9 shows the measurement of the PL intensity in dependence of a delay τ between two pulses, where the double pulse sequence was generated by phase-only shaping, via a linear phase function modulated on the electric field of the high energy wing of the excitation spectrum. This results in a so called two-color double pulse sequence with the delayed pulse possessing higher energies than the unmodulated one. Again the PL is considerably lower, than for the compound dissolved in THF. Asymmetries can be clearly found in (a) and (b), with shifted maximum PL intensity counts to positive and negative values of τ , respectively. In (c) slightly higher counts for $\tau > 0$ fs are evident. The absolute value of the PL counts are rising from changing the excitation center from 12225 cm^{-1} to 12500 cm^{-1} , but decreasing again with tuning to higher energies. The black line marks the position $\tau = 0$ fs, which helps identifying the asymmetry in the traces.

Discussion

The fact, that the 0-0 transition is fully suppressed in the PL emission spectrum of S-CBT in DOD, in comparison to the isolated molecule in THF, is a reliable indicator of H-type aggregation [96, 141, 144]. A further test is the analysis of $R = \frac{I_{0-0}}{I_{0-1}}$, which describes the ratio of the absorption peaks of the purely electronic and the first vibronic exciton bands. A fully suppressed 0-0 peak in emission as well as a decrease of R is clearly evident in Fig. 5.7 (a). Furthermore, atomic force microscope measurements of dropcasted DOD-solutions with S-CBT exhibit fibre-like structures with a thickness and height of 2 nm [141], which is in good agreement with [28].

All three coherence decays in Fig.5.8 (a, c, e) reflect fast dephasing of the generated coherence with an effective dephasing time of ≤ 50 fs. The fact, that the decay is still slower than the collinear intensity autocorrelation and the contrast between $\tau \ll 50$ fs and $\tau \gg 50$ fs of 2 is a strong argument that these data reflect ultrafast dynamics inherent to the nanofibre system. In contrast to this fast decay, oscillations are evident for delays bigger than 50 fs, with similar periods in (a) and (e). The period of the coherence decay in (c) is significantly shorter with $T = 42$ fs, which is almost half the period of the other decays. These characteristics are in agreement with the parameters found for S-CBT dissolved in THF. As described before, the oscillations are due to detuning effects of the central carrier frequency of the excitation and the transition energy of the accessed state. The similar detuning values for all three laser spectra and the constant linear absorption between 23000 cm^{-1} and 27000 cm^{-1} in Fig.5.7 (a) therefore suggest that first, the induced transition is again between the electronic ground state S_0 and second excited (only 2P allowed) state S_2 and second, S_2 does not change in its energetic position upon aggregation. This behaviour was already discussed in Section 2.4 in the theoretical introduction. The electronic and energetic changes introduced by aggregation, strongly depend on the interaction of the dipole moments and therefore on the transition dipole moments of the individual building blocks. For the non-resonant 2P transitions, this interaction must take place during the lifetime of the first accessed state, which is in this case a virtual state with lifetimes usually of several fs. This temporal window in which the dipole moments could interact with each other is too short. Hence, the only 2P allowed states, which are accessed via non-resonant 2P absorption exhibit the same spectral characteristics as the individual S-CBT units of this supramolecular structure. This is in agreement with the suggested spectral positions of S_2 for S-CBT dissolved in DOD and the spectral position of the second excited electronic state S_2 does not change upon aggregation.

The total counts are significantly smaller than for the S-CBT solution in THF. This is due to an overall reduction of the PL quantum of the system, with S-CBT in DOD possessing a PL quantum yield of around 1% instead of 15 % for S-CBT in THF [141]. In contrast to the THF data, the total PL intensity counts are not in agreement throughout all measurements. Whereas the counts in the coherence decay measurements increase from lower to high excitation energies, the counts in Fig.5.8 (b, d, f) and in Fig.5.9 first increase but then stay constant or decrease slightly. Although a total increase could be ascribed to the spectral shape shown in Section 5.3 in Fig.5.4, the subsequent decrease for the linear chirp and the two color pulse experiment does not match it. The only origin from which this discrepancy could evolve is possible local heating effects inside the solution. As both, the THF sample as well as the DOD sample, were measured completely during one single day and the highest excitation spectrum was set in the end of the session, it is not unlikely that local heating affects the results. Degradation can be excluded, as test measurements of the liner absorption and PL in the end of the experiments did not show any change. Therefore this fact will be ignored in the following and the considerations will further stick to the transition $S_0 \rightarrow S_2$.

The asymmetry in the traces in Fig.5.8 (b, d, f) is also resembled by the PL intensity dependencies on τ in the two color pulse experiments shown in Fig.5.9. Furthermore, the asymmetric shapes with respect to its particular global maximum, are still in agreement with the isolated S-CBT molecule data in Fig.5.2 and Fig.5.3, with higher PL intensity counts for positive values of β for excitations centred at 12225 cm^{-1} and 12987 cm^{-1} . The complete shifts of the symmetric traces in Fig.5.8 (d) and Fig.5.9 (b) are most likely due to remaining phase distortions in the laser pulse and thus this particular shift is not of interest. The two color double pulse experiment exhibits in general similar time-dependent sequences of instantaneous excitation energies as the linear chirp approach: for negative values of τ and β , respectively the high energy wing of the excitation spectrum hits at first the sample, whereas for $\tau, \beta > 0$ the sequence is reversed. The only difference is the linear sequence of excitation energies for the linear chirp, whereas as for the two color pulse two TL pulses hit the sample, one with lower equally distributed energies and one with higher ones. However, for both measurements the asymmetry is on similar time scales, because $\beta \leq 1000 \text{ fs}^2$ translates into pulse width of around $\leq 100 \text{ fs}$. For the S-CBT dissolved in THF, the asymmetry was found to originate most likely from either, stimulated emission of two-photons or enhanced intersystem crossing rates from the second excited state S_2 into a highly excited triplet state T_2 . Latter option was corroborated (for S-CBT in THF) by time-resolved EPR and transient absorption measurements, which revealed the existence of a triplet state and furthermore triplet-triplet absorptions in the fitting spectral regions. In the case of

DOD as solvent, both options present possible mechanisms, too. Although transient absorption measurements of S-CBT in DOD are not possible yet, comparison of EPR measurements between S-CBT dissolved in THF and DOD show similar behaviours of both samples without any significant change of the response [141]. In other words, the excitonic structure of the analysed triplet state T_1 did not change significantly upon H-aggregation and probably holds true for the complete triplet manifold. With less changes of the electronic triplet structure and the 2P allowed state S_2 , discussed above, the origin of the asymmetric shapes can be confidently ascribed to the β -dependent intersystem crossing rates, in analogy to the THF samples.

Conclusion

Preparing S-CBT in n-dodecane leads to a controlled aggregation from the isolated molecule form into individual nanofibre-like structures serving as H-aggregates. This was proven by the absorption and PL spectra of the S-CBT dissolved in n-dodecane, exhibiting a sufficiently suppressed 0-0 transition. Due to an alternating phase arrangement of the interacting transition dipoles, this transition is simply symmetry forbidden in the H-aggregated structure. However, defects in the nanofibre, such as kinks or impurities can lead to a softening of this usually ultimate symmetry rule, leading to a not-completely vanishing 0-0 peak in the PL spectrum.

The next addressed question, deals with the electronic states upon aggregation. It is known, that electronic states will mix and form a completely new electronically structure upon aggregation [65]. However, in the case of non-resonant two-photon absorptions the first interaction is between the ground state and a virtual state, usually with lifetimes of 2 - 3 fs. As discussed in the theoretical introduction in Section 2.3, this time span is too short to allow efficient interaction of the involved transition dipole moments. Hence, an electronically reorganization of the only two-photon allowed states is not likely to take place in the case of a structural aggregation. These findings were proven by the coherence decay measurements of S-CBT dissolved in n-dodecane. The decay exhibits very similar oscillations to the signals found for S-CBT dissolved in THF. For THF, these oscillations could be ascribed to detuning effects of the carrier frequency of the excitation field to the maximum of the transition of the S-CBT compound. For the nanofibres in n-dodecane similar oscillations of the delay dependent photoluminescence suggest the accessed states exhibit the same spectral positions. Hence, an energetically reorganization of this two-photon accessible state is not achieved by the H-type aggregate. Discrepancies between the coherence decay and the linear chirp, as well as the two color pulse measurements complicate the further

interpretation of the data. These differences are highly likely due to degradation of the sample, which is a common problem for this system, as all measurements shown in this chapter were taken at one single day one after another. Besides that, in all probability is the accessed state for S-CBT in n-dodecane the same state, found in Section 5.3, which has not significantly changed in its electronic structure upon aggregation.

The remaining ultrafast experiments all exhibit a slight asymmetry which was also found for the S-CBT in its fully dissolved form. Note that, the asymmetry in the latter case, was found to originate from phase-dependent intersystem crossing rates from the second excited state S_2 into a higher excited triplet state T_2 . Additional nanosecond pump-probe measurements, as done for S-CBT in THF, are missing and can not be performed in near future on S-CBT in DOD, due to problems of the flash photolysis setup and synthesis difficulties. However, time-resolved electron parametric resonance measurements revealed a lowest excited triplet state in the fully dissolved form. Moreover no significant change of the analysed triplet states upon H-aggregation was found. This is in agreement with the similar asymmetric shapes of the data and suggest that also for the nanofibre the intersystem crossing rate, can be slightly controlled via the linear chirp or the delay in the two-color pulse experiment.

5.5 Conclusions on the Isolated Molecule and Nanofibres

Both measurements of S-CBT, dissolved in THF and n-dodecane, revealed the existence of an only two-photon allowed state. States of this kind were already discussed in the theoretical introduction in Section 2.3. The first excited singlet state for a structure with symmetry D_{3h} is accessible via one- and two-photon absorption, while the second excited state only via the simultaneous absorption of two photons. This latter state can be identified with the one, accessed and analysed in the experiments in this chapter. Nevertheless it is important to note, that absorption into S_1 is still possible, but due to the decreasing spectral overlap between the laser and the S_1 absorption this signal will not contribute significantly.

The low PL quantum yield of S_1 therefore reflects fast non-radiative relaxation channels via a dark state. Identification of this dark state with the lowest excited triplet state was possible due to time-resolved electron parametric resonance experiments [141]. Furthermore, transient absorption measurements revealed a triplet state manifold above T_1 with the next triplet state T_2 centred at 25857 cm^{-1} . This triplet significantly overlaps with the spectral positions of the 2P allowed state S_2 , which mainly was accessed in the experiments. Hence, after the non-resonant two-photon absorption

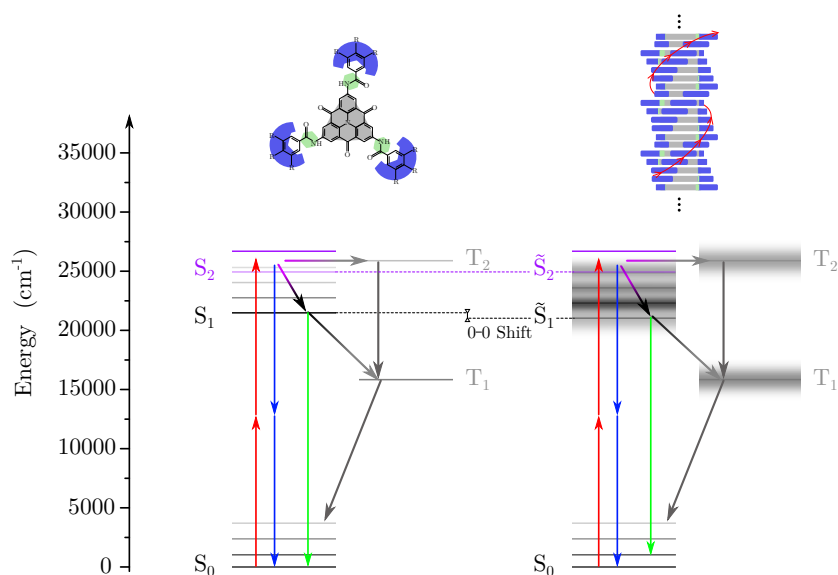


Fig. 5.10: Energy Diagram and Sketch of Ultrafast Processes for the Isolated Molecule and Nanofibre. Energy diagram of all involved states for the individual S-CBT compound and nanofibre-like form, stated in the preceding discussion. Two-photon (2P) absorption (red arrows) generates population in the only 2P allowed second excited state S_2 (magenta), which can relax via a variety of processes: (i) 2P induced stimulated emission (SE, blue arrows) due to the spectral width of the laser pulse and dependent on the linear chirp rate; (ii) internal conversion into S_1 and following vibrational relaxation (magenta-black arrow) leads to either photoluminescence (green arrow) or intersystem crossing into T_1 (black-grey arrow), with subsequent (non-)radiative deactivation of the excitation energy into S_0 (grey arrow); (iii) linear chirp dependent intersystem crossing from S_2 into T_2 (magenta-grey arrow) followed by non-radiative transitions into T_1 and S_0 (grey arrows).

process, the generated population in S_2 then, can either, be transferred to the first excited singlet state S_1 by internal conversion and is radiatively deactivated or be transferred to the second excited triplet state T_2 via intersystem crossing.

Figure 5.10 shows a sketch of the overall energy diagram of the isolated S-CBT compound and the H-aggregated structure, based on the obtained results. The energetic position of the first exciton singlet band, for reasons of clarity also denoted with S_1 , for the nanofibre was taken from [76], whereas, as stated above, the second excited singlet state \tilde{S}_2 does not change electronically upon aggregation. Note that, the only difference in the electronic structure between the isolated molecule and the nanofibre shown here, is the position of S_1 (marked by the dashed lines) and the formation of exciton bands. Note, this sketch represents only a simplified picture of the reality. All possible (non-)radiative transitions, which are important for this work, are reflected by the particular arrows. In order to interpret the asymmetric shapes of the PL traces in Figures 5.2, 5.3, 5.8 and 5.9 two possible situations arise: (i) after the non-resonant

2P absorption into S_2 , stimulated emission of two photons can take place, which is induced by the negatively chirped pulse, i.e. the decreasing instantaneous excitation energy. This SE signal is of similar energies as the excitation spectrum and therefore is sufficiently suppressed by the detection filters; (ii) due to the different sequences of the instantaneous excitation energies for negative and positive values of β , the generated wavepacket and therefore the intersystem crossing rate from S_2 into T_2 can vary. Subsequently, the detected PL signal from the first excited singlet state S_1 is highly dependent on that loss channel efficiency, which will be evident in the linear chirp or the two-color pulse PL traces. Although the SE of two photons was already found for a variety of dye molecules in solution [137, 138], there is not much information about S-CBT with respect to stimulated emission. In contrast the low PL quantum yield in solution, in other words, the extremely high intersystem crossing rates and the fact that a triplet T_2 is highly likely to significantly overlap with S_2 strongly indicate that phase-dependent intersystem crossing efficiencies are the origin of the obtained asymmetric shapes.

The next steps include further analysis of the EPR measurements, and extension of the flash photolysis experiment to S-CBT in solvents besides THF. The main question which should be addressed is the spectral position of the lowest excited triplet state as well as the behaviour of the triplet manifold upon aggregation. Solvents such as toluene or anisol will induce bundling of H-type nanofibres [141]. These bundles exhibit more complex exciton dynamics than the single nanofibre. Extending the experiments to these solvents, will shed light on the intrinsic ultrafast dynamics of the formed excitons, which are transferred coherently and non-coherently through the aggregated structure. The ultimate goal will be the analysis of the ultrafast exciton dynamics of these structures deposited on a glass cover slip with a fixed orientation, with microscopic precision.

Appendix

A.1 Group Theory Calculations on the S-CBT Core

S-CBT belongs to the degenerate D_{3h} point group (see Section 2.3, Fig.2.6) of order 12. The 1P and 2P dipole operators for D_{3h} read [89, 90, 92]

$$\Gamma(\hat{\mathbf{p}}) = \begin{pmatrix} E' \\ E' \\ A_2'' \end{pmatrix}, \quad \Gamma(\hat{\mathbf{p}}_{2P}) = \begin{pmatrix} A_1'/E' & E' & E'' \\ E' & A_1'/E' & E'' \\ E'' & E'' & E'' \end{pmatrix}, \quad (\text{A.1})$$

where two components in the 2P operator can exhibit A_1' (even) or E' (uneven) symmetry species, due to the degeneration of the point group (' and ' denote the symmetry and antisymmetry with respect to the mirror plane). The z-component can be neglected, as the molecular transition dipoles lie in the plane of the core. With the ground state having the highest symmetry A_1' , the symmetry relations for 1P transitions are

$$\begin{aligned} \Gamma(\psi_f) \times \Gamma(\hat{\mathbf{p}}_{x,y}) \times \Gamma(\psi_j) &\stackrel{!}{=} A_1' + \dots \\ \Gamma(\psi_f) \times E' \times A_1' &= A_1' + \dots \end{aligned}, \quad (\text{A.2})$$

where $\psi_{j,f}$ are the initial and final state wavefunctions and $A_1' + \dots$ reflects the fact, that the final integrand must contain at least one totally symmetric part. In case of a non-vanishing transition probability, $\Gamma(\psi_f)$ is E' as the multiplication of E' with itself yields $A_1' + A_2' + E'$ (see Table A.1). A_1' is totally symmetric and the transition from the ground state with A_1' via 1P absorption (E') into a state with E' is allowed. For 2P transitions, these considerations get more complex, as the 2P dipole operator can exhibit even and uneven symmetry species.

$$\begin{aligned} \Gamma(\psi_f) \times \Gamma(\hat{\mathbf{p}}_{2P}) \times \Gamma(\psi_j) &\stackrel{!}{=} A_g \\ \Gamma(\psi_f) \times \begin{pmatrix} A_1'/E' & E' & 0 \\ E' & A_1'/E' & 0 \\ 0 & 0 & 0 \end{pmatrix} \times A_1' &= A_g \\ &\rightarrow \Gamma(\psi_f) = A_1'/E' \end{aligned} \quad (\text{A.3})$$

D_{3h}	A'_1	A'_2	E'	A''_1	A''_2	E''
A'_1	A'_1	A'_2	E'	A''_1	A''_2	E''
A'_2	A'_2	A'_2	E'	A''_2	A''_1	E''
E'	E'	E'	$A'_1 + A'_2 + E'$	E''	E''	$A''_1 + A''_2 + E''$
A''_1	A''_1	A''_2	E''	A'_1	A'_2	E'
A''_2	A''_2	A''_1	E''	A'_2	A'_1	E'
E''	E''	E''	$A''_1 + A''_2 + E''$	E'	E'	$A'_1 + A'_2 + E'$

Tab. A.1: Multiplication Table of Point Group D_{3h} . Results of the multiplication of the symmetry species of the D_{3h} point group.

For the case of even symmetry species along the diagonal of $\Gamma(\hat{\mathbf{p}}_{2P})$ (black) the symmetry species of the final state can be A'_1 or E' , respectively. Both solutions results in at least a partly totally symmetric species. On the other hand, if $\Gamma(\hat{\mathbf{p}}_{2P})$ contains only the symmetry species E' (red case), the transition is only possible into states with $\Gamma(\Psi_f) = E'$, in analogy to the 1P transition. Therefore, the final conclusion is, 1P transition can only take place into states with the symmetry species E' , whereas 2P transitions are allowed into both, even (A'_1) and uneven (E') states.

A.2 Technical Details

A.2.1 Spincoater Settings

ramp1	ramp2	ramp3	rpm1	rpm2	rpm3	time1	time2	time3	ramp4
5 s	10 s	1 s	500	2000	2000	10 s	60 s	0 s	1 s

Tab. A.2: Settings of the Used Spincoater Program. Different ramps in seconds to tune the rotation in rounds per minute (RPM) to the desired RPM number and the particular time.

A.2.2 Quantum Dynamics Identification

A residual estimator for each iteration is defined by

$$s = \sqrt{\sum_{m=1}^{\mathcal{M}} \frac{\mathcal{P}_m(\beta_m) - [aP_m(Q, \beta_m) + b]}{\mathcal{M} - 2}}, \quad (\text{A.4})$$

with $\mathcal{P}_m(\beta_m)$ and $P_m(Q, \beta_m)$ being the experimentally obtained photoluminescence (PL) signals and the theoretically calculated quantum yields, respectively. The parameters a and b are adaptively updated and optimize the simulation to the experimental

A.3 Coherence Decay of an Ensemble MeLPPP Sample in Toluene

Molecule in	Energy (cm ⁻¹)		Rabi freq. (a.u.)		Decay times (fs)		
	E_2	E_3	Ω_{2P}	Ω_{1P}	$\frac{1}{\gamma_2}$	$\frac{1}{\gamma_3}$	$\frac{1}{\Gamma_{21}}$
Fig.4.8 (e)	25633	38663	0.00219	0.00255	75	75	150
Fig.4.8 (f)	25852	38641	0.00165	0.00304	75	75	150
Fig.4.8 (g)	25712	38716	0.00151	0.00281	75	75	150

Tab. A.3: Initial Values for the 4-Level Identification for MeLPPP. Initial parameters for the identification of the extended 4-level model for the asymmetric traces shown in Fig.4.8(e - g).

data. Due to the low signal and the considerable noise, the convergence of Eq.A.4 is dependent on the initial guess and the found minimum of the set of parameters is only a local minimum. As a result, the identified model may be not unique. However, by performing the same QDI procedure, but with different initial values of the parameters, no significant improvement between the several guesses was obtained. Therefore it is enough to perform the QDI procedure once, if the final set of parameters is reasonable in a physical sense. The prior knowledge from, for example, ensemble measurements is still helpful to improve the QDI procedure with respect to convergence time. Note that, no parameters are constrained during the procedure.

In Table A.3 the initial values of the optimised parameters for the 4-level model are listed.

A.3 Coherence Decay of an Ensemble MeLPPP Sample in Toluene

The envelope of the coherence decay of an ensemble sample of MeLPPP dissolved in toluene was measured under ambient conditions. The time-averaged excitation power (measured in front of the excitation lens) was set to 3 mW. The time-averaged excitation power for each double pulse delay $\tau \in [0, 300]$ fs (varied in 6 fs steps) was corrected and adjusted to stay constant through all amplitude masks. This data is plotted against the applied delay τ in Fig.A.3 with the constant excitation in red. The PL decays within the first 50 fs to 100 fs to the incoherent level, but clearly exhibits strong oscillations modulated on top of the trace beyond 100 fs. The period of the modulation is approximately 60 fs, which translates into an energy of 555 cm⁻¹. The ratio of the PL intensity for $\tau \ll 50$ fs and for $\tau \gg 100$ fs is again around 2, as in the single molecule experiments. Although considerable modulations of the PL intensity are found, the

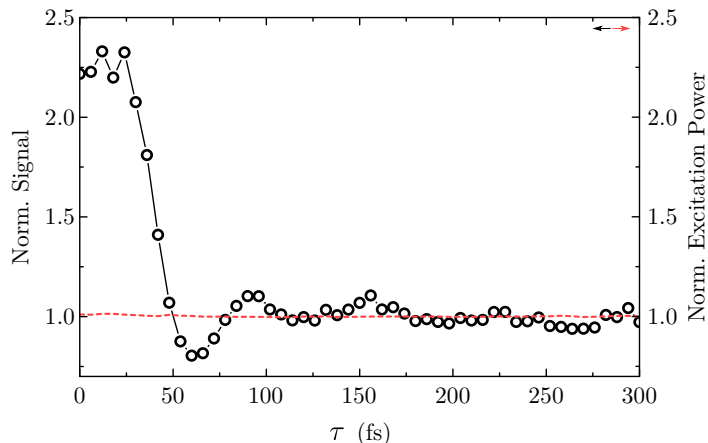


Fig. A.3: Coherence Decay Envelope of a MeLPPP Ensemble. Open circles: Detected photoluminescence intensity reflecting the envelope of the coherence decay of an ensemble sample of methyl-substituted ladder type poly(*para*-phenylenes) (MeLPPP) dissolved in toluene. The time-averaged excitation power stays constant for all delays (red dashed). The error bars are smaller than the size of the empty circles with $\pm 2\%$.

time-averaged excitation power stays constant for all modulation masks (red dashed line).

The oscillations arise as a result of detuning of the carrier frequency of the laser and the main transition energy of the ensemble absorption of the dissolved molecules. The 2P absorption shown in Fig.4.1 (a) belongs to a thin MeLPPP film in polystyrene, but will be comparable to that in solution. From Fig.4.1 (a) the detuning can be calculated and is around 410 cm^{-1} . From the trace in Fig.A.3 the amount of detuning can be estimated, too, and is the inverse of the oscillation period with 60 fs, which yields 555 cm^{-1} . Including the 6 fs step size of the measurement and a spectral shift due to embedding an organic dye into a solid matrix both values match nicely. The difference between the single molecule measurement and the one shown here, is, that in SM experiments only those emitters will be detected, which yield the strongest signal. Detection efficiencies of typical SM setups are below 10%, therefore a big spectral overlap with the absorption of the sample is required. Finally, the amount of molecules analysed in a SM experiment represents only a small fraction of emitter inside the sample film, which are spectrally shifted to resonance with the laser and not the actual distribution. However, in solution all molecules inside the excitation volume contribute to the signal and as the average absorption of MeLPPP is detuned with respect to the excitation spectrum, the coherence decay differs considerably in its shape. Remarkably, these oscillations are evident for values of the delay far beyond 75 fs, which is the dephasing time found by the QDI procedure. This proves, the long living coherence

generated between S_2 and S_0 by the first excitation pulse, which was already suggested by the simulations of the pure coherence in Fig.4.3 (e, f, g) and the scan of δ in Fig.4.4.

A.4 Shape of the Linear Chirp Dependent Photoluminescence Traces

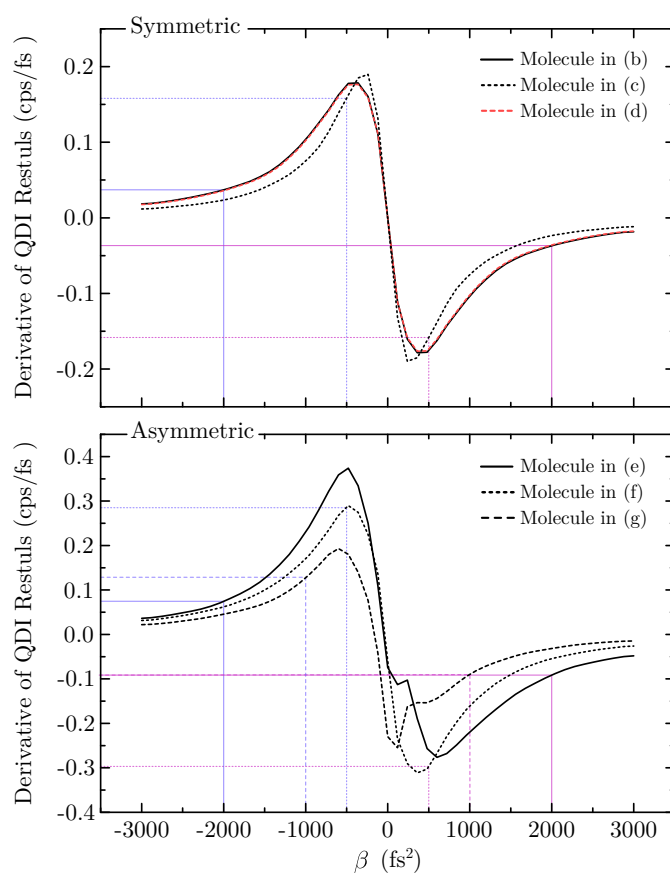


Fig. A.4: Derivative of Calculated Two-Photon Induced Population of Single MeLPPP Molecules. Derivative with respect to β of the six (symmetrical and asymmetrical) traces shown in Fig.4.8 (b - g) with the solid, dotted and dashed line respectively. For reasons of clarity the dashed line was coloured in red in the upper panel. The coloured guidelines clarify the different intercepts for the derivatives for exemplary values of β .

Not only the asymmetry in the β -dependent traces found in Section 4.3 reflects the strong variety of the energetic landscape through the sample and therefore the obtained parameters, but also the symmetrically shaped PL intensity traces do so. The calculation of the first derivative with respect to β of the QDI results of both cases, symmetric and asymmetric, yields a clear picture of the distribution of the steepness of

the rising and falling wings. These derivatives are plotted for the six molecules shown in Fig.4.8 (b - g) in Fig.A.4. Whereas the derivatives for the first two symmetric cases are nearly identical (solid and dotted), the third one differs considerably (dashed). The two coinciding lines in the upper panel in Fig.A.4 reflects the similar obtained QDI parameters for these two molecules. The FWHM of the three symmetrical responses are 1420 fs^2 for Molecules shown in Fig.4.8 (e, g) and 1200 fs^2 for (f). These parameters and the derivatives reflect the diversity even among the MeLPPP molecules which exhibit a symmetric PL intensity response upon variation of β . For the sake of completeness the derivatives of the asymmetric simulations are shown, too. Clear deviations are evident and more important, the derivative of the QDI simulation of molecule shown in Fig.4.8 (f), corroborates the stated asymmetric character of the PL intensity measurement.

A.5 Symmetric Simulations to Asymmetric Data

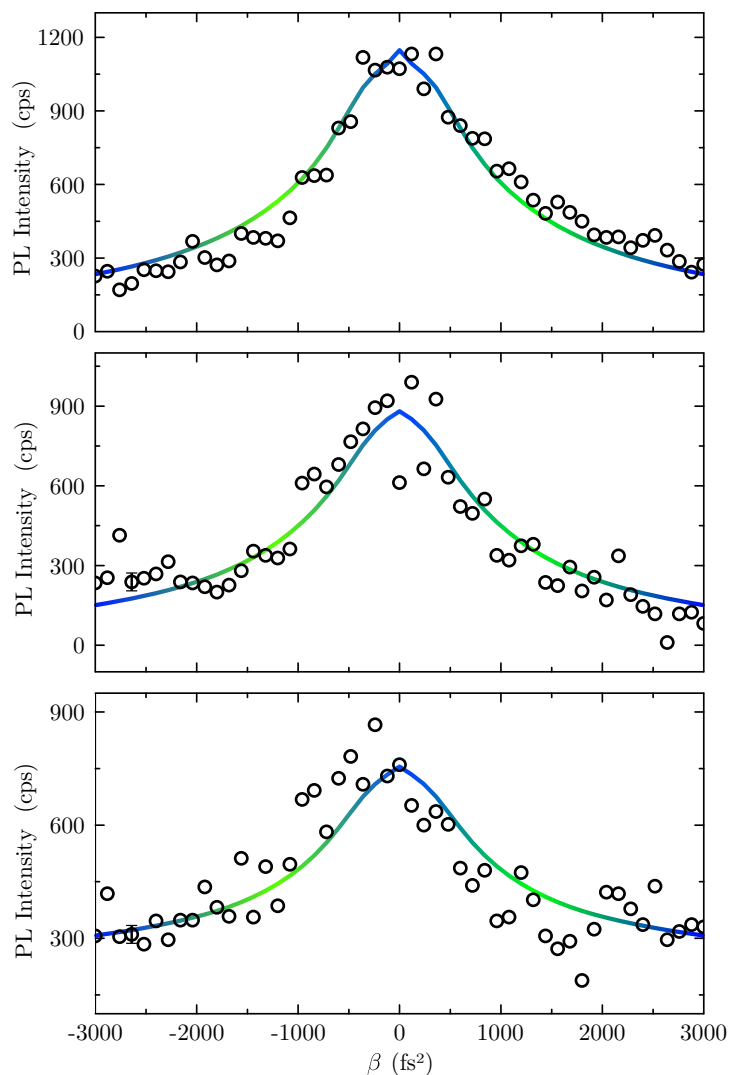


Fig. A.5: Symmetric Calculations on Asymmetric Datasets from MeLPPP. Photoluminescence (PL) intensities in counts per seconds for molecules shown in Fig.4.8 (b-d) and 2-level model simulations instead of a 3-level model

To test whether the asymmetric data shown in Fig.4.8 (b, c, d) are reproducible with a much simpler model, i.e. a two level instead of a three level model, the asymmetric data and the two-level model calculations are shown in Fig.A.5. Within the given error, the simulation could reproduce the traces for most of the data points. However, the deviations are significant and systematic through all values of β . For example, the simulated counts are constantly larger for values $\beta < 0 \text{ fs}^2$ and lower for $\beta > 0 \text{ fs}^2$ in

the upper panel. Deviations are furthermore evident for the middle and lower panel, with higher counts than the simulation for negative values of β and lower counts for positive ones. Finally, this proves, that the physics behind the PL intensity response upon variation of β go beyond a simpler two level model and an extended model needs to be included.

A.6 Asymmetry of Linear Chirp Dependent S-CBT Measurements

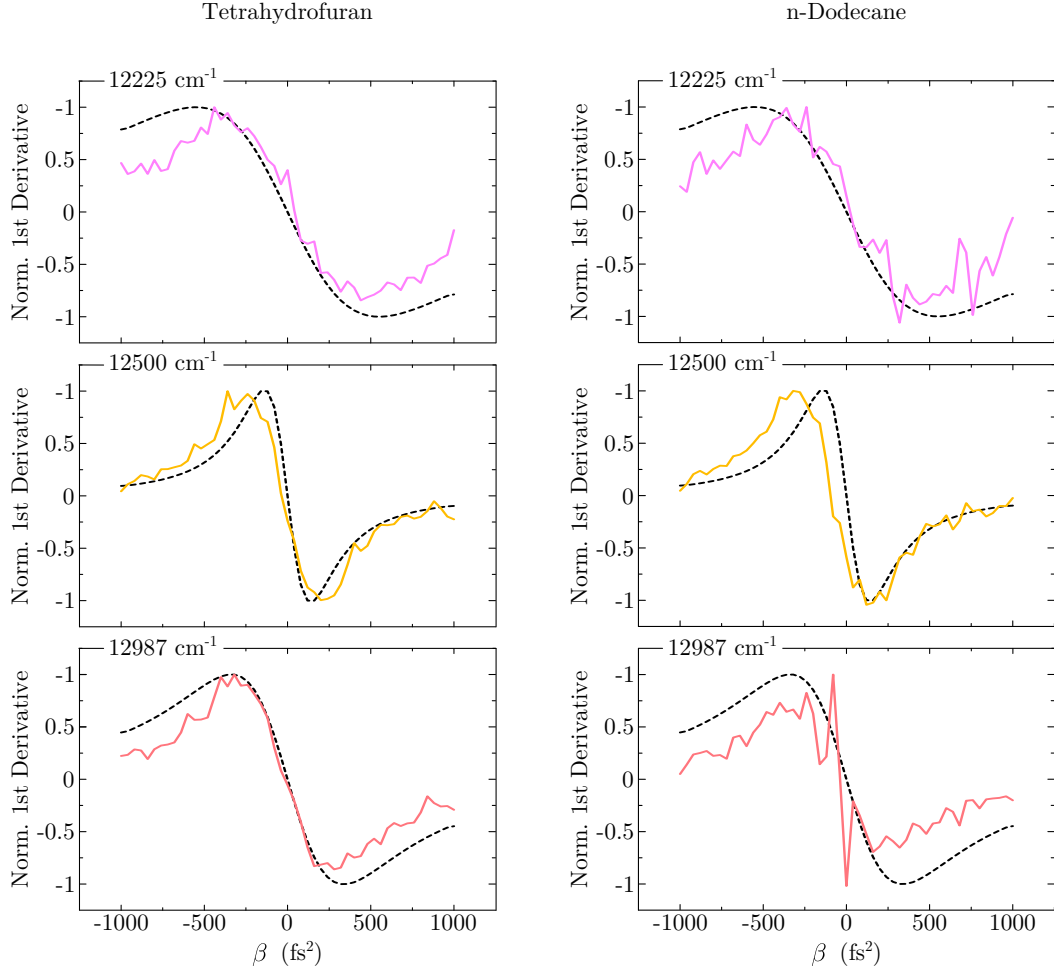


Fig. A.6: 1st Derivative of Linear Chirp Measurements on S-CBT in THF and DOD. Left (right) panel: derivative with respect to β of the traces shown in Fig.5.2 (b, d, f) for S-CBT in THF (DOD) with the solid line for the experimental and dashed line for the simulated datasets.

For reasons of clarity the 1st derivatives (with respect to β) of all presented experimental and simulated data shown in Fig.5.2 (b, d, f) and Fig.5.8 (b, d, f) were calculated and are plotted in Fig.A.6 for each laser spectrum (color code as in main text). Again the simulated symmetric curves are centred at $\beta = 0 \text{ fs}^2$ which is responsible for different zero crossing points for experiment and simulation. For S-CBT in THF as well as in DOD for the data set acquired with the laser centred at 12225 cm^{-1} and 12987 cm^{-1} the differences between the dashed and the solid lines for $\beta >$ and $< 0 \text{ fs}^2$ deviate

for each graph. In other words, for negative values of β the absolute value of the 1st derivative is higher than for $\beta > 0$ fs². This is not the case for the data set with the laser spectrum centred at 12500 cm⁻¹. Although the overall trend is similar for S-CBT in THF and in DOD, the difference between $\beta <$ and > 0 fs² shown for DOD and 12987 cm⁻¹ is not that pronounced as for S-CBT in THF.

A.7 Fluorescence Spectroscopy of Highly Excited States in S-CBT

Fig.A.7 shows the detected PL signal upon excitation at 35088 cm⁻¹, which is 285 nm. No signal is obtained between 27000 cm⁻¹ and 32000 cm⁻¹ and the PL stems exclusively from S₁. In other words, next to all possible non-radiative decay channels, the generated excitation probability is transferred into S₁, which is deactivated under emission of photons.

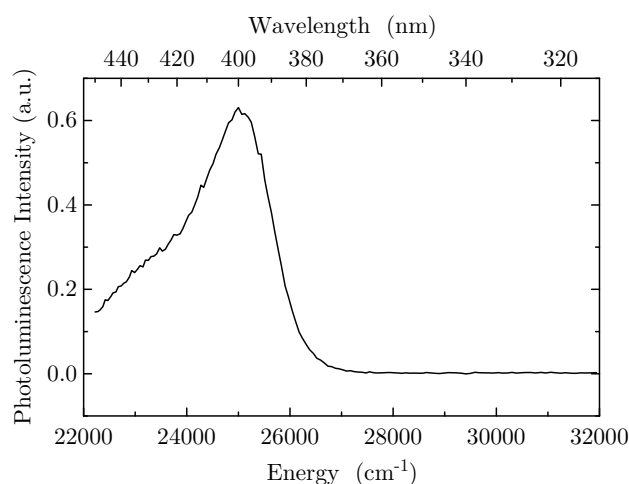


Fig. A.7: Photoluminescence Spectra of S-CBT in THF. Photoluminescence spectrum of the carbonyl-bridged tryarylamine (CBT) derivative with s-chiral side chains (S-CBT) dissolved in tetrahydrofuran (THF) excited at 35088 cm⁻¹ (285 nm).

A.8 Transient Absorption Spectroscopy

In order to measure very small optical density (OD) signal a flash photolysis setup is used. Via a continuous white light source, a laser providing the pump pulse and nanosecond-triggered electronics the transmittance of the sample is measured in dependency of the time, ranging from nano- to microseconds with and without preceding pump pulse. Measuring the laser and white light signal without the sample inside the beam path is not required, which can be seen with the following equation:

$$\begin{aligned}\Delta\text{OD} &= \text{OD}_{\text{exc}} - \text{OD} \\ \Delta\text{OD} &= \log\left(\frac{I_0}{I_{\text{exc}}}\right) - \log\left(\frac{I_0}{I}\right) \\ \Delta\text{OD} &= \log\left(\frac{I}{I_{\text{exc}}}\right) .\end{aligned}\tag{A.5}$$

The transient absorption with the pump beam at 22222 cm^{-1} and the probe energy at 10309 cm^{-1} (excited state absorption, i.e. triplet-triplet absorption) for S-CBT dissolved in THF is shown in Fig.A.8. To fit the rising and decaying component the data was separated in two parts. The fit for both parts reads

$$f(t) = Ae^{-\frac{t}{\tau_c}} + C_0 ,\tag{A.6}$$

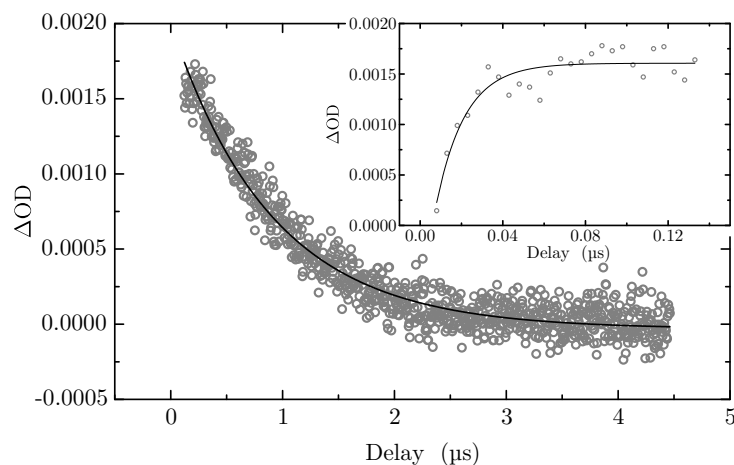


Fig. A.8: Transient Absorption of S-CBT in Tetrahydrofuran. Transient absorption with pump at 22222 cm^{-1} and probe at 10309 cm^{-1} of the carbonyl-bridged tryarylamine (CBT) derivative with s-chiral side chains (S-CBT) for delays between the pulses ranging from $0\text{ }\mu\text{s}$ to about $4.5\text{ }\mu\text{s}$. The transient was separated in two different parts: one with rising component for short delays (inset) and one with decreasing behaviour for larger delays (main panel). The fits, represented by solid black lines, reflect mono exponential functions. The data was taken with permission of B.Wittmann and further processed for analysis and display [76].

where t is the dependent parameter for the delay, τ_c the decay constant, A the amplitude and C_0 an offset. For the rising component the obtained parameters are: $A = (-0.00243 \pm 3.810^{-4})$, $C_0 = (0.00161 \pm 3.710^{-5})$ and $\tau_c = (14.1 \pm 2.5)$ ns. The fit to the decreasing signal yields: $A = (-0.00203 \pm 210^{-5})$, $C_0 = (-3.210^{-5} \pm 7.310^{-6})$ and $\tau_c = (907 \pm 18)$ ns. Owing to the time resolution of the setup of about 5 ns the estimated error of τ_c is bigger than given by the fit.

A.9 Wavefunctions upon Linearly Chirped Excitation

In order to check whether the wavefunctions exhibit different shapes upon a linearly chirped excitation and inversion of the sign of the chirp parameter β , calculations on the solution of the time-dependent Schrodinger equation were performed. The results shown in the following stick to references [135] and [145], but were slightly modified in accordance to the different experimental conditions. The wavefunction coefficients after interaction with an electro-magnetic field read

$$c_n(t) \approx \frac{i}{\hbar} \mu \langle n|g\rangle \int_{-\infty}^t dt' f(t') e^{-i\Delta_n t'} \quad , \quad (\text{A.7})$$

with the time-dependent amplitude of the electro-magnetic field $f(t')$, the detuning between the excitation and molecular transition frequency Δ_n , the transition dipole moment μ and the Franck-Condon factor $\langle n|g\rangle$. For simplifications of the code, the linearly chirped pulse is approximated via a sequence of time-delayed transform limited pulses, each with a different carrier frequency ω_i . By neglecting the interference of the EM-field of each TL laser pulse p_i with ω_i Equation A.7 can be further approximated with

$$c_n \approx \frac{i}{\hbar} \mu \langle n|g\rangle \sqrt{2\pi} \Delta_t f_0 e^{-\frac{\Delta_n^2 \Delta_t^2}{2}} \quad , \quad (\text{A.8})$$

where the time-independent EM field amplitude f_0 and the pulse width Δ_t was introduced. In order to include the widened pulse width of the chirped field f_0 is assumed to be a Gaussian distribution of values. The delay between the pulses can be calculated according to the value of the chirp parameter β via $\tau = \frac{\partial}{\partial \omega} (\varphi_{\text{mod}}) = \beta (\omega - \omega_{\text{mod}})$, with $\omega_{\text{mod}} = \omega_i$.

A snapshot is taken 100 fs after the pulse of energy ω_i interacted with the system. Hence, each final wavefunction for the molecular system **after** interacting with each laser pulse with energy ω_i is governed by the radiation-free Hamiltonian:

$$|\psi\rangle (r, t, \beta) = \sum_i \sum_n c_{n,i} e^{-i[\omega_n t + \frac{1}{2}\beta(\omega - \omega_i)^2]} |\chi_n(r)\rangle \quad . \quad (\text{A.9})$$

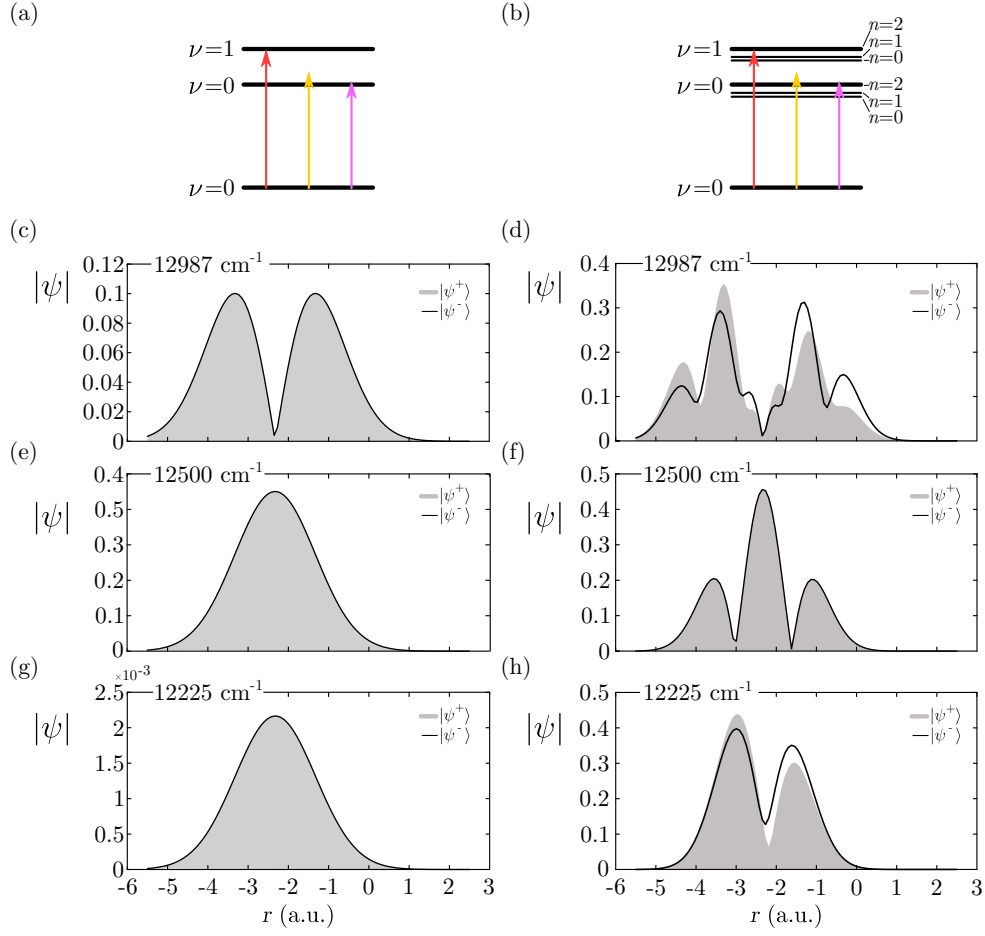


Fig. A.9: Excited State Wavefunctions for Different Excitation Spectra. (a,b). Sketched representations of the used models, with 3-levels and 7 levels, whereas the thin black lines represent the skeletal modes denoted with n' and the thick black lines the C-C stretching modes denoted with n . The color coded arrows represent the centre excitation energy of the three spectra shown in the main text in Fig. 5.1 (b) and Fig.5.7 (b). **(c, e, g)** Absolute of the excited state wavefunction calculated for the 3-level model for the three excitation spectra, for $\beta = \pm 500 \text{ fs}^2$. All input parameters were taken from Tab. 5.1. **(d, f, h)** Absolute of the excited state wavefunction calculated for the 7-level model for the three excitation spectra, for $\beta = \pm 500 \text{ fs}^2$. The skeletal modes were set to 24250 cm^{-1} , 24450 cm^{-1} , 25750 cm^{-1} and 25950 cm^{-1} .

The index n counts through all excited states and i through the excitation energies. Each wavefunction was calculated at $t=100 \text{ fs}$ after the pulse interaction, which describes the wavefunction immediately after the pulse is off, and the second phase factor in the exponential describes the relative phase between each of the interacting transform-limited pulses [145]. $\chi_n(r)$ is the solution of the stationary Schrodinger equation for a harmonic potential and is basically the Hermite-polynomial function in dependency of a normalised nuclear coordinate and the excited state number n [112].

Two different models are calculated and compared to each other: (i) a 3-level model consisting of the electronic ground state S_0 and the lowest two vibronic levels ($\nu = 0, 1$) in the excited state with indices $\nu = 0, 1$; (ii) a 7-level model, now including 4 low-energy vibronic modes, which are usually in the low energy wing of each of the former vibrational bands. While the 0-0 and 0-1 transition are ascribed to the C-C bond stretching mode at $\approx 1300 \text{ cm}^{-1}$, these low-energy modes are due to movement of the skeleton of the compound with an energy of $\approx 200 \text{ cm}^{-1}$ [48]. Finally, the latter model will exhibit $n^{(\nu)} = 0^{(0)}, 1^{(0)}, 2^{(0)}, 0^{(1)}, 1^{(1)}, 2^{(1)}$, whereas ν counts the 0-0 and 0-1 transition and n the skeletal modes inside each vibronic band of number ν . This is included in the calculation by multiplication of a hermite polynomial function of order n to each of the polynomial functions of order n' . Both models are sketched in Fig.A.9 (a) and (b), with the respective centre transition energy of the particular excitation spectrum (color code with respect to the spectra in main text 5.1).

The results on the three level model are shown in Fig.A.9 (c, e, g) for $\beta = \pm 500 \text{ fs}^2$ denoted with $|\psi^\pm\rangle$. Clearly, linearly chirping the excitation pulse with positive and negative values does not induce any change of the generated wave packet, which is in contrast to the found results in Chapter 5. Therefore the model was extended to the 7-level model including low-energy skeletal modes in the low energy wing of the 0-0 and 0-1 peak of the absorption. These modes are narrowly spaced with only 200 cm^{-1} . Now the wavefunctions for the excitations at 12987 cm^{-1} and 12225 cm^{-1} clearly differ between $\beta < 0 \text{ fs}^2$ and $\beta > 0 \text{ fs}^2$. However, for the middle excitation at 12500 cm^{-1} the wavefunction does not exhibit any difference. This is in perfect agreement with the data, where asymmetric values of the β -dependent PL intensity were obtained only for the high and low excitation energy. Although these simulations are only a rough estimate, they provide an understanding of the initially generated wave packet and their shapes, which can finally result in different ISC crossing rates (see [140]). Furthermore, this proves that these mostly hidden low-energy modes, can make a significant contribution to the ultrafast dynamics and quantum mechanical properties of such systems.

Bibliography

- (1) Moerner, W. E.; Kador, L. *Phys. Rev. Lett.* **1989**, *62*, 2535–2538.
- (2) Orrit, M.; Bernard, J. *Physical Review Letters* **1990**, *65*, 2716–2719.
- (3) Issac, A.; Hildner, R.; Ernst, D.; Hippus, C.; Würthner, F.; Köhler, J. *Physical Chemistry Chemical Physics: PCCP* **2012**, *14*, 10789–98.
- (4) Vanden Bout, D. A.; Wai-Tak, Y.; Dehong, H.; Dian-Kui, F.; Swager, T.; Barbara, P. F. *Science* **1997**, *277*, 1074.
- (5) Schörner, M.; Beyer, S. R.; Southall, J.; Cogdell, R. J.; Köhler, J. *Journal of Physical Chemistry B* **2015**, *119*, 13964–13970.
- (6) Issac, A.; Hildner, R.; Hippus, C.; Würthner, F.; Köhler, J. *ACS Nano* **2014**, *8*, 1708–17.
- (7) Wilma, K.; Issac, A.; Chen, Z.; Würthner, F.; Hildner, R.; Köhler, J. *The Journal of Physical Chemistry Letters* **2016**, *7*, 1478–1483.
- (8) Pullerits, T.; Mirzov, O; Scheblykin, I. G. *The Journal of Physical Chemistry B* **2005**, *109*, 19099–19107.
- (9) Hildner, R.; Winterling, L.; Lemmer, U.; Scherf, U.; Köhler, J. *Chemical Physics Chemistry* **2009**, *10*, 2524–2534.
- (10) Kunz, R.; Timpmann, K.; Southall, J.; Cogdell, R. J.; Freiberg, A.; Köhler, J. *Biophysical Journal* **2014**, *106*, 2008–2016.
- (11) Reilly, P. D.; Skinner, J. L. *Physical Review Letters* **1993**, *71*, 4257–4260.
- (12) Krause, S.; Kowerko, D.; Börner, R.; Hübner, C. G.; Borczykowski, C. *Chemical Physics Chemistry* **2011**, *12*, 303–312.
- (13) Hildner, R.; Lemmer, U.; Scherf, U.; Köhler, J. *Chemical Physics Letters* **2006**, *429*, 103–108.
- (14) Ernst, D., *Untersuchung der photophysikalischen Eigenschaften einzelner multichromophorer Farbstoffsysteme*, 2007, Bayreuth, Universität Bayreuth ,Diploma Thesis.

- (15) Lakowicz, J. R., *Principles of Fluorescence Spectroscopy Principles of Fluorescence Spectroscopy*, 2006, Berlin Heidelberg New York, Springer Verlag.
- (16) Köhler, A.; Bässler, H., *Electronic Processes in Organic Semiconductors: An Introduction*, 2015, Weinheim, Wiley–VCH Verlag GmbH & Co. KGaA.
- (17) Wilma, K.; Unger, T.; Tuncel Kostakoğlu, S.; Hollfelder, M.; Hunger, C.; Lang, A.; Gürek, A. G.; Thelakkat, M.; Köhler, J.; Köhler, A.; Gekle, S.; Hildner, R. *Physical Chemistry Chemical Physics* **2017**, *19*, 22169–22176.
- (18) Van Dijk, E. M. H. P.; Hernando, J.; Garcia-Lopez, J.-J.; Crego-Calama, M.; Reinhoudt, D. N.; Kuipers, L.; Garcia-Parajo, M. F.; van Hulst, N. F. *Physical Review Letters* **2005**, *94*, 078302.
- (19) Van Dijk, E. M. H. P.; Hernando, J.; Garcia-Parajo, M. F.; van Hulst, N. F. *The Journal of Chemical Physics* **2005**, *123*, 064703.
- (20) Hildner, R.; Brinks, D.; Van Hulst, N. F. *Nature Physics* **2010**, *7*, 172–177.
- (21) Brinks, D.; Hildner, R.; van Dijk, E. M. H. P.; Stefani, F. D.; Nieder, J. B.; Hernando, J.; van Hulst, N. F. *Chemical Society reviews* **2014**, *43*, 2476–91.
- (22) Meshulach, D.; Silberberg, Y. *Nature* **1998**, *396*, 239–242.
- (23) Higgins, G.; Pokorny, F.; Zhang, C.; Bodart, Q.; Hennrich, M. *Phys. Rev. Letters* **2017**, *119*, 220501.
- (24) Accanto, N.; Roque, P. M. D.; Galvan-sosa, M.; Christodoulou, S.; Moreels, I.; van Hulst, N. F. *Light: Science & Applications* **2017**, *6*, e16239.
- (25) Pachón, L. A.; Yu, L.; Brumer, P. *Faraday Discussions* **2013**, *163*, 485–495.
- (26) Pachón, L. A.; Brumer, P. *Journal of Chemical Physics* **2013**, *139*.
- (27) Liebel, M.; Kukura, P. *Nature Chemistry* **2016**, *9*, 45–49.
- (28) Haedler, A. T.; Meskers, S. C.; Zha, R. H.; Kivala, M.; Schmidt, H. W.; Meijer, E. W. *Journal of the American Chemical Society* **2016**, *138*, 10539–10545.
- (29) Haedler, A. T.; Kreger, K.; Issac, A.; Wittmann, B.; Kivala, M.; Hammer, N.; Köhler, J.; Schmidt, H.-W.; Hildner, R. *Nature* **2015**, *523*, 196–199.
- (30) Siringhaus, H. *Advanced Materials* **2014**, *26*, 1319–1335.
- (31) Chiang, C. K.; Fincher, C. R.; Park, Y. W.; Heeger, A. J.; Shirakawa, H.; Louis, E. J.; Gau, S. C.; MacDiarmid, A. G. *Physical Review Letters* **1977**, *39*, 1098–1101.
- (32) Sharma, G. D.; Roy, M. S.; Mikroyannidis, J. A.; Justin Thomas, K. R. *Organic Electronics: physics, materials, applications* **2012**, *13*, 3118–3129.

-
- (33) Heeger, A. J. *Advanced Materials* **2014**, *26*, 10–28.
- (34) Herbst, S.; Soberats, B.; Leowanawat, P.; Stolte, M.; Lehmann, M.; Würthner, F. *Nature Communications* **2018**, *9*, 2646.
- (35) Lin, H.; Camacho, R.; Tian, Y.; Kaiser, T. E.; Würthner, F.; Scheblykin, I. G. *Nano Letters* **2010**, *10*, 620–626.
- (36) Eisele, D. M.; Knoester, J.; Kirstein, S.; Rabe, J. P.; Vanden Bout, D. A. *Nature Nanotechnology* **2009**, *4*, 658–663.
- (37) Friend, R. H.; Gymer, R. W.; Holmes, A. B.; Burroughes, J. H.; Marks, R. N.; Taliani, C.; Bradley, D. D. C.; Dos Santos, D. A.; Bredas, J. L.; Logdlund, M.; Salaneck, W. R. *Nature* **1999**, *397*, 121–128.
- (38) Harrison, M. G.; Urbasch, G.; Mahrt, R.; Giessen, H.; Bäessler, H.; Scherf, U. *Chem. Phys. Letters* **1999**, *313*, 755–762.
- (39) Demtröder, W., *Molekülphysik. Theoretische Grundlagen und experimentelle Methoden*, 2013; Vol. 2nd Ed. Berlin, Boston: Oldenbourg Wissenschaftsverlag.
- (40) Barford, W., *Electronic and Optical Properties of Conjugated Polymers*, 2013; Vol. 2nd Ed. Oxford, Oxford University Press.
- (41) Blythe, A. R., *Electrical Properties of Polymers*, 2005; Vol. 2nd Ed. Cambridge, Cambridge University Press.
- (42) Tretiak, S.; Saxena, A.; Martin, R. L.; Bishop, A. R. *Physical Review Letters* **2002**, *89*, 097402.
- (43) Bäessler, H. *Physica Status Solidi (b)* **1993**, *175*, 15–56.
- (44) Bäessler, H.; Schweitzer, B. *Accounts of Chemical Research* **1999**, *32*, 173–182.
- (45) Sariciftci, N. S., *Primary Photoexcitations in Conjugated Polymers*, 1997, Singapore, World Scientific Publishing Co. Pte. Lt.
- (46) Schindler, F.; Lupton, J. M.; Feldmann, J.; Scherf, U. *Proceedings of the National Academy of Sciences of the United States of America* **2004**, *101*, 14695–14700.
- (47) Schindler, F.; Jacob, J.; Grimsdale, A. C.; Scherf, U.; Müllen, K.; Lupton, J. M.; Feldmann, J. *Angewandte Chemie International Edition* **2005**, *44*, 1520–1525.
- (48) Baderschneider, S.; Scherf, U.; Hildner, R. *Journal of Physical Chemistry A* **2016**, *120*, 233–240.
- (49) Müller, J. G.; Lemmer, U.; Raschke, G.; Anni, M.; Scherf, U.; Lupton, J. M.; Feldmann, J. *Physical Review Letters* **2003**, *91*, 267403.

- (50) Hohenau, A.; Cagran, C.; Kranzelbinder, G; Scherf, U.; Leising, G *Advanced Materials* **2001**, *13*, 1303–1307.
- (51) Hildner, R., *Investigation of the Photophysical Properties of π -conjugated Polymers. A Study by Non-linear, Time-resolved and Single-molecule Spectroscopy*, 2008, Bayreuth, Universität Bayreuth, Ph.D. Thesis.
- (52) Kanematsu, Y.; Kushida, T. *Physical Review B* **1993**, *48*, 9066–9070.
- (53) Hildner, R.; Lemmer, U.; Scherf, U.; van Heel, M.; Köhler, J. *Advanced Materials* **2007**, *19*, 1978–1982.
- (54) Rebane, L. A.; Gorokhovskii, A. A.; Kikas, J. V. *Applied Physics B* **1982**, *29*, 235–250.
- (55) Loudon, R., *The Quantum Theory of Light*, 2000, New York, Oxford, Oxford University Press.
- (56) Göppert-Mayer, M. *Annalen der Physik* **1931**, *401*, 273–294.
- (57) Allen, L.; Eberly, J., *Optical Resonance and Two-Level Atoms*, 1987, New York, Dover Publications.
- (58) Scherf, U *Journal of Materials Chemistry* **1999**, *9*, 1853–1864.
- (59) Würthner, F. *Chemical Communications* **2004**, *0*, 1564–1579.
- (60) Kersting, R.; Lemmer, U.; Mahrt, R. F.; Leo, K.; Kurz, H.; Bäessler, H.; Göbel, E. O. *Physical Review Letters* **1993**, *70*, 3820–3823.
- (61) Lanzani, G.; Cerullo, G.; Brabec, C.; Sariciftci, N. S. *Physical Review Letters* **2003**, *90*, 047402–1–4.
- (62) Spreitler, F.; Sommer, M.; Hollfelder, M.; Thelakkat, M.; Gekle, S.; Köhler, J. *Physical Chemistry Chemical Physics* **2014**, *16*, 25959–25968.
- (63) Lang, E.; Hildner, R.; Engelke, H.; Osswald, P.; Würthner, F.; Köhler, J. *ChemPhysChem* **2007**, *8*, 1487–1496.
- (64) Gadermaier, C; Cerullo, G; Manzoni, C; Scherf, U; List, E. J. W.; Lanzani, G *Chemical Physics Letters* **2003**, *384*, 251–255.
- (65) Hestand, N. J.; Spano, F. C. *Chemical Reviews* **2018**, *118*, 7069–7163.
- (66) Orrit, M.; Bernard, J; Personov, R. I. *Journal of Physical Chemistry* **1993**, *97*, 10256–10268.
- (67) Tamarat, P.; Maali, A.; Lounis, B.; Orrit, M. *The Journal of Physical Chemistry A* **2000**, *104*, 1–16.

-
- (68) Raithel, D.; Simine, L.; Pickel, S.; Schötz, K.; Panzer, F.; Baderschneider, S.; Schiefer, D.; Lohwasser, R.; Köhler, J.; Thelakkat, M.; Sommer, M.; Köhler, A.; Rossky, P. J.; Hildner, R. *Proceedings of the National Academy of Sciences* **2018**, *115*, 2699–2704.
- (69) Kunz, R.; Timpmann, K. K.; Southall, J.; Cogdell, R. J.; Freiberg, A.; Köhler, J. *Angewandte Chemie - International Edition* **2013**, *52*, 8726–8730.
- (70) Weigel, A.; Sebesta, A.; Kukura, P. *Journal of Physical Chemistry Letters* **2015**, *6*, 4032–4037.
- (71) Yoshizawa, M.; Yasuda, A.; Kobayashi, T. *Applied Physics B Photophysics and Laser Chemistry* **1991**, *53*, 296–307.
- (72) Bosma, W. B.; Mukamel, S. *Phys. Rev. Letters* **1992**, *68*, 2456–2459.
- (73) Holcman, J.; Choueiry, A. A.; Enderlin, A.; Hameau, S.; Barisien, T. *Nano Letters* **2011**, *11*, 4496–4502.
- (74) Shen, Y. R., *The Principles of Non-Linear Optics*, 1984, New York, John Wiley & Sons.
- (75) Haken, H.; Wolf, H. C., *Molekülphysik und Quantenchemie 4th Edition*, 2003, Springer Verlag Berlin Heidelberg New York.
- (76) Wittmann, B., *Untersuchung des Aggregationsverhaltens von supramolekularen Nanofasern mittels optischer Spektroskopie*, 2017, Bayreuth, Universität Bayreuth, Master Thesis.
- (77) Spano, F. C.; Mukamel, S. *Physical Review A* **1989**, *40*, 5783–5801.
- (78) Drobizhev, M.; Stepanenko, Y.; Dzenis, Y.; Karotki, A.; Rebane, A.; Taylor, P. N.; Anderson, H. L. *Journal of the American Chemical Society* **2004**, *126*, 15352–15353.
- (79) Drobizhev, M.; Makarov, N. S.; Hughes, T.; Rebane, A. *Journal of Physical Chemistry B* **2007**, *111*, 14051–14054.
- (80) Wang, H.; Li, Z.; Shao, P.; Qin, J.; Huang, Z. L. *Journal of Physical Chemistry B* **2010**, *114*, 22–27.
- (81) Lippitz, M., *Zwei-Photonen-Fluoreszenz-mikroskopie und -Spektroskopie von Sauerstofftransportproteinen: Experimente zur Sauerstoffbindung und an einzelnen Proteinen*, 2002, Mainz, Universität Mainz, Ph.D. Thesis.
- (82) Johnsen, M.; Paterson, M. J.; Arnbjerg, J.; Christiansen, O.; Nielsen, C. B.; Jørgensen, M.; Ogilby, P. R. *Physical Chemistry Chemical Physics* **2008**, *10*, 1177–1191.

- (83) McClain, W. M. *The Journal of Chemical Physics* **1971**, *55*, 2789–2796.
- (84) Maruo, S.; Nakamura, O.; Kawata, S. *Optics Letters* **1997**, *22*, 132.
- (85) Sun, H. B.; Matsuo, S.; Misawa, H. *Applied Physics Letters* **1999**, *74*, 786–788.
- (86) Denk, W.; Strickler, J. H.; Webb, W. W. *New Series* **1990**, *248*, 73–76.
- (87) Helmchen, F.; Denk, W. *Nature Methods* **2005**, *2*, 932–940.
- (88) Zondervan, R.; Kulzer, F.; Orlinskii, S. B.; Orrit, M. *The Journal of Physical Chemistry A* **2003**, *107*, 6770–6776.
- (89) Hollas, J. M., *Symmetry in Molecules*, 1972, London, Chapman & Hall.
- (90) Harris, D. C.; Bertolucci, M. D., *Symmetry and Spectroscopy*, 1978, New York, Dover Publications.
- (91) Farchioni, R.; Grosso, G., *Organic Electronic Materials*, 2001, Berlin, Heidelberg, New York, Springer.
- (92) Herzberg, G., *Molecular Spectra and Molecular Structure - Volume II Infrared and Raman Spectra of Polyatomic Molecules*, 1991, Malabar, Florida, Krieger Publishing Company.
- (93) Hildner, R.; Lemmer, U.; Scherf, U.; Köhler, J. *Chem. Phys. Letters* **2007**, *448*, 213–217.
- (94) Haedler, A. T.; Beyer, S. R.; Hammer, N.; Hildner, R.; Kivala, M.; Köhler, J.; Schmidt, H.-W. W. *Chemistry - A European Journal* **2014**, *20*, 11708–11718.
- (95) Kasha, M.; Rawls, H. R.; Ashraf El-Bayoumi, M. *Pure and Applied Chemistry* **1965**, *11*, 371–392.
- (96) Spano, F. C. *Accounts of chemical research* **2009**, *43*, 429–439.
- (97) Hestand, N. J.; Spano, F. C. *Accounts of Chemical Research* **2017**, *50*, 341–350.
- (98) Bloch, F.; Hansen, W. W.; Packard, M. *Physical Review* **1946**, *69*, 127.
- (99) Breuer, H.; Petruccione, F., *The Theory of Open Quantum Systems*, 2002, New York, Oxford University Press.
- (100) Gerhardt, I.; Wrigge, G.; Zumofen, G.; Hwang, J.; Renn, A.; Sandoghdar, V. *Physical Review A - Atomic, Molecular, and Optical Physics* **2009**, *79*, 1–4.
- (101) Wilma, K.; Shu, C.-c.; Scherf, U.; Hildner, R. *Journal of the American Chemical Society* **2018**, *140*, 15329–15335.
- (102) Lindblad, G. *Commun. Math. Phys.* **1976**, *48*, 119.

-
- (103) Tempel, D. G.; Aspuru-Guzik, A. *Chem. Phys.* **2011**, *391*, 130–142.
- (104) Scherf, U.; Müllen, K. *in: Advances in Polymer Science* **1995**, *123*, 1.
- (105) Bässler, H. *Chemical Physics Letters* **1993**, *203*, 28–32.
- (106) Somitsch, D; Wenzl, F. P.; Kreith, J; Pressl, M; Kaindl, R; Scherf, U; Leising, G; Knoll, P *Synthetic Metals* **2003**, *138*, 39–42.
- (107) Burrows, H. D.; De Melo, J. S.; Serpa, C.; Arnaut, L. G.; Monkman, A. P.; Hamblett, I.; Navaratnam, S. *Journal of Chemical Physics* **2001**, *115*, 9601–9606.
- (108) Stampfl, J; Tasch, S; Leising, G; Scherf, U. *Synthetic Metals* **1995**, *71*, 2125–2128.
- (109) Vaughan, J. C.; Hornung, T; Feurer, T; Nelson, K. A. *Optics Letters* **2005**, *30*, 323–325.
- (110) Lozovoy, V. V.; Pastirk, I.; Dantus, M. *Optics Letters* **2004**, *29*, 775–777.
- (111) Xu, B.; Gunn, J. M.; Cruz, J. M. D.; Lozovoy, V. V.; Dantus, M. *Journal of the Optical Society of America B* **2006**, *23*, 750.
- (112) Parson, W. W., *Modern Optical Spectroscopy*, 2015, Berlin Heidelberg New York, Springer Verlag.
- (113) Tannor, D. J.; Rice, S. A. *The Journal of Chemical Physics* **1985**, *83*, 5013–5018.
- (114) Shapiro, M.; Brumer, P. *The Journal of Chemical Physics* **1986**, *84*, 4103–4104.
- (115) Tannor, D. J.; Kosloff, R.; Rice, S. A. *The Journal of Chemical Physics* **1986**, *85*, 5805–5820.
- (116) Brumer, P.; Shapiro, M. *Chem. Phys. Letters* **1986**, *126*, 541–546.
- (117) Peirce, A. P.; Dahleh, M. A.; Rabitz, H. *Physical Review A* **1988**, *37*, 4950–4964.
- (118) Kosloff, R; Rice, S. A.; Gaspard, P; Tersigni, S *Chemical Physics* **1989**, *139*, 201–220.
- (119) Van der Walle, P; Milder, M. T. W.; Kuipers, L; Herek, J. L. *Proceedings of the National Academy of Sciences of the United States of America* **2009**, *106*, 7714–7717.
- (120) Shapiro, M.; Brumer, P. *Reports on Progress in Physics* **2003**, *66*, 859–942.
- (121) Kuroda, D. G.; Singh, C. P.; Peng, Z.; Kleiman, V. D. *Science* **2009**, *326*, 263–267.
- (122) Aeschlimann, M.; Bauer, M.; Bayer, D.; Brixner, T.; Garcia de Abajo, F. J.; Pfeiffer, W.; Rohmer, M.; Spindler, C.; Steeb, F. *Nature* **2007**, *446*, 301–304.

- (123) Michaelis De Vasconcellos, S.; Gordon, S.; Bichler, M.; Meier, T.; Zrenner, A. *Nature Photonics* **2010**, *4*, 545–548.
- (124) Fras, F.; Mermillod, Q.; Nogues, G.; Hoarau, C.; Schneider, C.; Kamp, M.; Höfling, S.; Langbein, W.; Kasprzak, J. *Nature Photonics* **2016**, *10*, 155–158.
- (125) Shu, C. C.; Dong, D.; Petersen, I. R.; Henriksen, N. E. *Phys. Rev. A* **2017**, *95*, 033809.
- (126) Grondelle, R. V.; Novoderezhkin, V. I. *Phys. Chem. Chem. Phys.* **2005**, *8*, 793–807.
- (127) Laquai, F.; Park, Y.-s.; Kim, J.-j.; Basche, T. *Macromolecular Rapid Communications* **2009**, *30*, 1203–1231.
- (128) Scholes, G. D.; Mirkovic, T.; Turner, D. B.; Buchleitner, A. *Energy & Environmental Science* **2012**, *5*, 9374–9393.
- (129) Wan, Y.; Stradomska, A.; Knoester, J.; Huang, L. *Journal of the American Chemical Society* **2017**, *139*, 7287–7293.
- (130) Cogdell, R. J.; Gall, A.; Köhler, J. *Quarterly Reviews of Biophysics* **2006**, *39*, 227–324.
- (131) Menke, S. M.; Holmes, R. J. *Energy & Environmental Science* **2014**, *7*, 469–832.
- (132) Siebbeles, L. D. A.; Grozema, F. C. e., *Charge and Exciton Transport through Molecular Wires*, 2011, Weinheim, Wiley–VCH Verlag GmbH & Co. KGaA.
- (133) Tamai, Y.; Matsuura, Y.; Ohkita, H.; Bente, H.; Ito, S. *The Journal of Physical Chemistry Letters* **2014**, *5*, 399–403.
- (134) Scherer, N. F.; J., C. R.; Matro, A.; Du, M.; Ruggiero, A. J.; Romero-Rochin, V.; Cina, J. A.; Fleming, G. R.; Rice, S. A. *The Journal of Chemical Physics* **2002**, *95*, 1487–1511.
- (135) Leichtle, C.; Schleich, W. P.; Averbukh, I. S.; Shapiro, M. *The Journal of Chemical Physics* **1998**, *108*, 6057.
- (136) Konar, A.; Lozovoy, V. V.; Dantus, M. *Journal of Physical Chemistry Letters* **2012**, *3*, 2458–2464.
- (137) Belfield, K. D.; Bondar, M. V.; Yanez, C. O.; Hernandez, F. E.; Przhonska, O. V. *The Journal of Physical Chemistry B* **2009**, *113*, 7101–7106.
- (138) Belfield, K. D.; Bondar, M. V.; Morales, A. R.; Padilha, L. A.; Przhonska, O. V.; Wang, X. *Chemical Physics Chemistry* **2011**, *12*, 2755–2762.
- (139) Nairat, M.; Konar, A.; Lozovoy, V. V.; Beck, W. F.; Blanchard, G. J.; Dantus, M. *The Journal of Physical Chemistry A* **2016**, *120*, 1876–1885.

- (140) Herek, J. L.; Wohlleben, W; Cogdell, R. J.; Zeidler, D; Motzkus, M *Nature* **2002**, *417*, 533–535.
- (141) Wittmann, B.; Kreger, K.; Schmidt, H.-W.; Hildner, R. Unpublished Manuscript., 2019.
- (142) Hunger, C., *Alternative Concepts for Electron Acceptor and Transparent Conducting Electrode in Organic Photovoltaics*, 2015, Bayreuth, Universität Bayreuth, Ph.D. Thesis.
- (143) Köhler, A.; Beljonne, D. *Advanced Functional Materials* **2004**, *14*, 11–18.
- (144) Celestino, A.; Eisfeld, A. *Journal of Physical Chemistry A* **2017**, *121*, 5948–5953.
- (145) Bouchene, M. A.; Nicole, C.; Girard, B. *Journal of Physics B: Atomic, Molecular and Optical Physics* **1999**, *32*, 5167–5177.

Publication List

Used for the present thesis

- *Visualising Hidden Ultrafast Processes in Individual Molecules by Single-Pulse Coherent Control*
Wilma, K., Shu, C., Scherf, U., Hilder, R., The Journal of the American Chemical Society, Volume 140, Issue 45 (2018), pp. 15329 - 22176
- *Two-Photon Induced Ultrafast Coherence Decay of Highly Excited States in Single Molecules*
Wilma, K., Shu, C., Scherf, U., Hilder, R., New Journal of Physics, Volume 21, Focus on Nanoscale Quantum Optics (2019), pp. 045001

Further publications

- *Revealing Structure Formation in PCPDTBT by Optical Spectroscopy*
Scharsich, C., Fischer, F. S. U., Wilma, K., Hildner, R., Ludwigs, S., Köhler, A., Journal of Polymer Science Part B Polymer Physics, Volume 53, Issue 20 (2015), pp. 1416-1430
- *Tracing Single Electrons in a Disordered Polymer Film at Room Temperature*
Wilma, K., Issac, A., Chen, Z., Würthner, F., Hildner, R., Köhler, J., The Journal of Physical Chemistry Letters, Volume 7, Issue 8 (2016), pp. 1478 - 1483
- *Excited State Dynamics and Conformations of a Cu(II)-Phthalocyanine-Perylenebisimide Dyad*
Wilma, K., Unger, T., Kostakoglu, S., Hollfelder, M., Hunger, C., Lang, A., Gürek, A. G., Thelakkat, M., Köhler, J., Köhler, A., Gele, S., Hildner, R., Physical Chemistry Chemical Physics, Volume 19, Issue 33 (2017), pp. 22169 - 22176

Danksagung

Letzten Endes möchte ich mich bedanken. Ohne euch wäre diese Arbeit wohl nicht zu solch einem Erfolg für mich geworden, von wissenschaftlichem aber auch persönlichem Wert. Ich möchte euch für eure Zeit und eure Unterstützung danken.

Als Erstes möchte ich dir danken, Richard. Nachdem ich im Masterstudium meine Leidenschaft für die Kurzzeitphysik und nicht-lineare Optik entdeckt hatte, war dein Angebot, einen Ultrakurzzeitaufbau zu erstellen und in Betrieb zu nehmen, geradezu die perfekte Chance für mich. Deine Tür stand immer offen und du warst immer bereit Frage und Antwort zu stehen. Ich danke dir für die fantastische Betreuung und deine menschliche Art, die meine Arbeit in deiner jungen Arbeitsgruppe unvergesslich macht. Ich wünsche dir alles Gute für deine Professur in Groningen.

Jürgen, vielen Dank, dass du mich seit meiner Bachelorarbeit 2012 unterstützt hast und mir stets wissenschaftliche Verantwortung übertrugst. Ich danke dir für die angenehme familiäre Stimmung am Lehrstuhl, die meine Arbeit um ein vielfaches erleichterte. Aufgrund unserem guten Verhältnisses konnte ich stets mit einem Lächeln in die Arbeit gehen. Des Weiteren danke ich allen Professoren des GraKos, die immer ihr Möglichstes gegeben haben die interdisziplinäre Arbeit zwischen den unterschiedlichen Arbeitsgruppen zu stärken und die Promotion für die Studenten so fair wie möglich zu gestalten. Ich bekam viele Chancen, mich durch das GraKo weiter zu entwickeln und durfte Auslandsreisen bestreiten und Konferenzen beiwohnen. Ohne das GraKo wäre dies wohl nicht möglich gewesen. Ein besonderes Danke gilt hier Prof. Dr. Jürgen Köhler und Prof. Dr. Stephan Kümmel, den beiden „Köpfen“ des GraKos. Prof. Dr. Stephan Kümmel und Prof. Dr. Peter Strohrigel danke ich ebenfalls für ihre Rollen als Mentor. Prof. Dr. Markus Lippitz danke ich für seinen Einsatz für die Promotionsstudenten und für die Übernahme der Zweitkorrektur. Auch wenn der Großteil meiner Proben schon einen Bart hat, danke ich Prof. Dr. Ullrich Scherf für das MeLPPP und Prof. Dr. Hans-Werner Schmidt für das S-CBT.

Many thanks to you, Chuancun. You hosted me during my time in Australia and I felt very welcome at your research group. I have learnt a lot about the theoretical physics and you had always time to answer any (silly) question. You showed me a lot of Canberra and I have enjoyed my time to the fullest. I am pleased to have such a

strong collaboration and also found a new friend on the other side of the globe. All the best to your new group in China and to your family!

Ohne die Techniker am Lehrstuhl würde wohl nur schwer etwas vorangehen. Werni und Stefan, vielen Dank für eure Unterstützung und eure stetige Hilfe. Ebenfalls danke ich euch für eure menschliche Art, die einem immer die Kaffeepausen, Ausflüge und Feiern versüßt haben. Evelyn, Michaela und Franzi, das Rückgrat des Lehrstuhls. Vielen Dank für eure Hilfe bei organisatorischen aber auch menschlichen Anliegen. Ich fühlte mich sehr aufgehoben durch eure Unterstützung. Auch dir Claudia, vielen lieben Dank für deine Hilfe bezüglich aller GraKo und Universitäts-relevanten Anliegen. Ihr haltet den Lehrstuhl am Laufen. Frank der Macher aka „des mach ma scho das' bassd“, egal welches wirres Konzept ich mir überlegt habe, ihr in der Werkstatt habt es verbessert und umgesetzt, vielen Dank! Auch ein dickes Danke an Peter Hagen, der in den Endzügen meiner Arbeit mir bei IT-technischen Angelegenheiten unter die Arme griff.

Meinem Lehrstuhl, EPIV, SSM oder EPIX und meiner Arbeitsgruppe danke ich herzlich. Ihr habt mein Leben (sind ja immerhin schon 10 Jahre) hier an der Universität unvergesslich gemacht. Fachliche und schwachsinnige Diskussionen werden wohl eingebrannt bleiben und ich mich gerne zurückerinnern. Ich habe hier sehr viel Zeit verbracht und habe (fast) jeden Moment genossen. Ich danke euch allen (ich versuche es chronologisch zu halten): Daniel Zalami, Johannes Maier, Inga Elvers, Sebastian Beyer, Alexander „Lexington“ Löhner, Ralle, Bernd „Fazzo“ Wittmann, Carlos mi Mamasita, Lisa Günter, Sebastian Pickel, Daniel Cornelius Zapf, Christian „Schiggi“ Schörner, Uwe Gerken und allen anderen von früheren und heutigen Zeiten des Lehrstuhls.

Den wohl wichtigsten Teil meines Lebens belegen meine Familie und Freunde. Ich wäre nicht der, der ich heute bin, hätte ich euch nicht an meiner Seite gehabt. Ich danke dir Fabian, dass du seit je her mein bester Kumpel bist und auch obwohl wir uns nicht mehr so oft sehen, sich niemals etwas daran ändern wird. Ich fühle mich heute noch wie bei unseren stundenlangen Telefonaten in der Schulzeit, wenn wir miteinander quatschen. Nicht umsonst verbinden uns unsere Oberarme für immer. Sebastian, ich habe mit dir wohl den Kumpel in Bayreuth gefunden, der mir hier gefehlt hat. Vielen Dank, dass wir uns immer zoffen, verarschen aber auch ernsthaft austauschen konnten und können. Ich hoffe, dass unsere Wege auch weiterhin davon profitieren. Bernd, danke dass du so ein guter Freund geworden bist. Ich weiß, ich habe dich oft gestresst, vor allem gegen Ende meiner Arbeit. Ich danke dir sehr, dass du immer ehrlich warst und mir sehr viel geholfen hast bezüglich meiner Probleme, vor allem deiner Probe betreffend. Unsere Gespräche haben mir extrem viel gebracht. Auch dir Daniel vielen Dank. Du verhältst

dich zwar ab und zu fragwürdig aber ich wusste immer, dass man auf dich zählen kann. Ich bin sehr froh darüber, dass wir uns noch relativ kurz vor Ende kennengelernt haben.

Meinem kompletten Freundeskreis aus Hof und aus Bayreuth danke ich für alles und jeden einzelnen Zeitpunkt. Jede Feier, jeder Ausflug oder einfach nur unsere Bierchen am Kanal werden unvergesslich bleiben. Ihr gehört zu meiner Familie.

Mama und Papa, auch wenn ich in einer, für manche ungewohnten Konstellation, aufgewachsen bin, möchte ich keinen Moment missen. Ihr habt mir beide bewiesen, dass es keine Situation im Leben gibt, die man nicht bewältigen kann, wenn man einfach nur den Willen besitzt. Ich habe die stärkste Frau zur Mutter und den aufopferungsvollsten Mann zum Vater. Ihr habt den stolzesten Mann zum Sohn. Ich danke euch für alle Werte, die ihr mir mitgegeben habt. Ihr habt mir den Weg bereitet, den ich heute gehen kann. Bastian, Henri, Madelaine, Sibylle und Saskia vielen Dank, dass ihr mir immer geholfen habt den Kopf frei zu bekommen und für mich da wart.

Letzten Endes danke ich dir ganz besonders, Carina. In dir habe ich sowohl meinen besten Freund als auch meine Familie gefunden (damit meine ich auch Heike, Hartmut und Marc). Du hast mir Rückhalt gegeben wie kein anderer Mensch und warst in guten aber vor allem schwierigen Zeiten da, um mir zuzuhören. Vielen Dank für jeden einzelnen Moment den wir haben, du bist (m)ein wundervoller Mensch. Ich liebe dich.

Eidesstattliche Versicherung

Hiermit versichere ich an Eides statt, dass ich die vorliegende Arbeit selbstständig verfasst und keine anderen als die von mir angegebenen Quellen und Hilfsmittel verwendet habe.

Zusätzlich erkläre ich hiermit, dass ich keinerlei frühere Promotionsversuche unternommen habe.

Weiterhin erkläre ich, dass ich keine Hilfe von gewerblichen Promotionsberatern bzw. -vermittlern oder ähnlichen Dienstleistern weder bisher in Anspruch genommen habe, noch künftig in Anspruch nehmen werde.

Außerdem erkläre ich mich einverstanden, dass die elektronische Fassung meiner Dissertation unter Wahrung meiner Urheberrechte und des Datenschutzes einer gesonderten Prüfung unterzogen werden kann.

Des Weiteren erkläre ich mich einverstanden, dass bei Verdacht wissenschaftlichen Fehlverhaltens Ermittlungen durch universitätsinterne Organe der wissenschaftlichen Selbstkontrolle stattfinden können.

Ort, Datum

Kevin WILMA